Electrocaloric Cooling Power and Long Term Stability of Barium Zirconate Titanate

**Zur Erlangung des akademischen Grades Doktor-Ingenieur (Dr.-Ing.)
genehmigte Dissertation von M.Sc. Florian Weyland aus Rodgau
Mai 2019 – Darmstadt – D 17**

TECHNISCHE
UNIVERSITÄT
DARMSTADT

Electrocaloric Cooling Power and Long Term Stability of Barium Zirconate Titanate

Genehmigte Dissertation von M. Sc. Florian Weyland aus Rodgau

1. Gutachten: Prof. Dr. Jürgen Rödel
2. Gutachten: Prof. Dr. Karsten Albe

Tag der Einreichung: 7. Mai 2019
Tag der Prüfung: 24. Juni 2019

Fachbereich Material- und Geowissenschaften
Mai 2019 — Darmstadt — D 17

To my wife Shantall

Table of content

Abstract

Interest on the electrocaloric effect grew rapidly over the past decade. In this time, the electrocaloric temperature change was directly and indirectly determined in a lot of ferroelectric materials. To compare those materials with respect to electrocaloric applications not solely the electrocaloric but also the thermophysical performance characteristics need to be considered. Here, a material related cooling power is derived on basis of a Newtonian cooling model of a thin plate, which includes electrocaloric as well as thermophysical properties. From the material related cooling power a caloric figure of merit is derived which is used to compare materials of the $Ba(Zr_xTi_{1-x})O_3$ system. The electrocaloric temperature change, specific heat capacity and thermal conductivity of $Ba(Zr_xTi_{1-x})O_3$ are provided. The depicted compositions have different paraelectric to ferroelectric phase transition behavior, ranging from first order to second order character, diffusive phase transition and relaxor-like behavior. The largest caloric figure of merit is found for $Ba(Zr_{0.13}Ti_{0.87})O_3$ with a second order paraelectric to ferroelectric phase transition. The caloric figure of merit is further used to compare the electrocaloric effect with the magnetocaloric and mechanocaloric effect. It is found that multilayer structures of the best lead containing electrocaloric materials can compete with representative materials of the magnetocaloric effect. Whereas, NiTi, a representative of the mechanocaloric effect, exhibits a five times larger performance than the best magnetocaloric or electrocaloric materials.

Phenomenological calculations are used to elaborate on the effect of critical end points, tricritical point and triple point on the electrocaloric behavior. The electric field – temperature phase diagram of BT is provided. The contribution of the latent heat, at the electric field induced first order phase transition, to the electrocaloric temperature change is subtracted and by this it is demonstrated that the largest electrocaloric responsivity is at the liquid – vapor type of critical end point. The phase diagram and electrocaloric temperature changes for $Ba(Zr_xTi_{1-x})O_3$ are calculated. A complete composition – temperature phase diagram with the position of a tricritical point and of a triple point are calculated. By considering the line of critical end points, an electric field – composition – temperature phase diagram is constructed. It is demonstrated that the triple point has a positive effect in the enhancement of the electrocaloric properties, whereas the tricritical point has no effect.

The long term stability of the electrocaloric temperature change and the effect of oxygen vacancy migration is demonstrated. The movement of oxygen vacancies under strong electric fields, leads to a change in the defect chemistry and hence, to increased leakage current and Joule heating. It is demonstrated that the main conduction mechanism after 10^6 electrocaloric cycles changes from ionic to electronic conductivity. By changing the polarity of the electric field after every 10^5 cycles the oxygen vacancies can be redistributed and a large cycle number of 10^6 without decreasing ECE is obtained.

Das Interesse über den elektrokalorischen Effekt hat im letzten Jahrzehnt rasch zugenommen. In dieser Zeit wurde die elektrokalorische Temperaturänderung in vielen ferroelektrischen Materialien direkt und indirekt bestimmt. Um diese Materialien im Hinblick auf elektrokalorische Anwendungen zu vergleichen, müssen nicht nur die elektrokalorischen, sondern auch die thermophysikalischen Leistungsmerkmale berücksichtigt werden. In dieser Arbeit wird eine materialbezogene Kühlleistung auf Basis des Newtonschen Abkühlgesetzes einer dünnen Platte hergeleitet, welche sowohl elektrokalorische als auch thermophysikalische Eigenschaften einschließt. Aus der materialbezogenen Kühlleistung wird eine kalorische Gütezahl abgeleitet, mit welcher Materialien des $Ba(Zr_xTi_{1-x})O_3$ Systems verglichen werden. Die elektrokalorische Temperaturänderung, die spezifische Wärmekapazität und die Wärmeleitfähigkeit von $Ba(Zr_xTi_{1-x})O_3$ werden bereitgestellt. Die gezeigten Zusammensetzungen weisen ein unterschiedliches paraelektrisch zu ferroelektrisch Phasenübergangsverhalten auf, das von Verhalten erster Ordnung, bis zweiter Ordnung, diffusem Phasenübergang und relaxorähnlichem Verhalten reicht. Die größte kalorische Gütezahl wurde für $Ba(Zr_{0.13}Ti_{0.87})O_3$ gefunden, welches einen Übergang zweiter Ordnung von paraelektrischer zu ferroelektrischer Phase hat. Die kalorische Gütezahl wird ferner verwendet, um den elektrokalorischen Effekt mit dem magnetokalorischen und mechanokalorischen Effekt zu vergleichen. Es wurde festgestellt, dass Mehrschichtstrukturen der besten bleihaltigen elektrokalorischen Materialien, mit repräsentativen magnetokalorischen Materialien konkurrieren können, wohingegen das mechanokalorische Material NiTi eine fünfmal höhere Leistung zeigt als die besten magnetokalorischen oder elektrokalorischen Materialien.

Phänomenologische Berechnungen werden verwendet, um die Auswirkung von kritischen Endpunkten, trikritischem Punkt und Tripelpunkt auf das elektrokalorische Verhalten zu untersuchen. Das elektrische Feld – Temperatur Phasendiagramm von BT wird bereitgestellt. Der Beitrag der latenten Wärme, des durch ein elektrisches Feld induzierten Phasenüberganges erster Ordnung, zur elektrokalorischen Temperaturänderung wird abgezogen, und es wird gezeigt, dass die größte elektrokalorische Empfindlichkeit am kritischen Endpunkt des Flüssigdampftyps liegt. Das Phasendiagramm und die elektrokalorischen Temperaturänderungen für $Ba(Zr_xTi_{1-x})O_3$ wurden berechnet. Es wurde ein komplettes Zusammensetzung – Temperatur Phasendiagramm mit Position des trikritischen Punktes und Tripelpunktes berechnet. Unter Berücksichtigung der Linie von kritischen Endpunkten wurde ein elektrisches Feld – Zusammensetzung – Temperatur Phasendiagramm erstellt. Es wird gezeigt, dass der Tripelpunkt einen positiven Einfluss auf die elektrokalorischen Eigenschaften hat, während der trikritische Punkt keinen Einfluss hat.

Die Langzeitstabilität der elektrokalorischen Temperaturänderung und der Einfluss von Sauerstoffleerstellenmigration wird gezeigt. Die Bewegung von Sauerstoffleerstellen unter starken elektrischen Feldern führt zu einer Änderung der Defektchemie und somit zu einem erhöhten Leckstrom

und Joulescher Erwärmung. Es wird gezeigt, dass der Hauptleitungsmechanismus nach 10^6 elektrokalorischen Zyklen von ionischer zu elektronischer Leitfähigkeit wechselt. Durch ändern der Polarität des elektrischen Feldes nach jeweils 10^5 Zyklen können die Sauerstoffleerstellen umverteilt werden und eine große Zyklenzahl von 10^6 ohne Abnahme in der elektrokalorischen Temperaturänderung wird erhalten.

El interés por el efecto electrocalórico creció rápidamente en la última década. Durante este tiempo, el cambio de la temperatura electrocalórica fue determinada de manera directa e indirecta en varios materiales ferroeléctricos. Para comparar esos materiales con respecto a las aplicaciones electrocalóricas, no solo se deben considerar las características electrocalóricas, sino también las características de rendimiento termofísico. El poder de enfriamiento relacionado con el material deriva de un modelo de enfriamiento newtoniano de una placa delgada, el cual incluye propiedades tanto electrocalóricas como termofísicas. A partir de la potencia de enfriamiento del material se deriva una figura calórica de mérito, la cual es utilizada para comparar los materiales del sistema $Ba(Zr_xTi_{1-x})O_3$. El cambio de temperatura electrocalórica, la capacidad térmica específica y la conductividad térmica de $Ba(Zr_xTi_{1-x})O_3$ son proporcionados. Las composiciones representadas tienen diferentes comportamientos de transición de fase paraelectro a ferroelectrica, que van desde el carácter de primer orden al de segundo orden, transición de fase difusiva y comportamiento similar al relaxor. La figura de mérito más alta es encontrada para $Ba(Zr_{0.13}Ti_{0.87})O_3$ con una transición de fase de segundo orden de paraelectro a ferroeléctrica. La figura calórica de mérito es utilizada para comparar el efecto electrocalórico con el efecto magnetocalórico y mecanocalórico. Se encuentra que las estructuras multicapa de los mejores materiales electrocalóricos que contienen plomo pueden competir con materiales representativos del efecto magnetocalórico. Mientras, NiTi, un representante del efecto mecanocalórico, exhibe un rendimiento cinco veces mayor que los mejores materiales magnetocalóricos o electrocalóricos.

Los cálculos fenomenológicos son utilizados para elaborar el efecto de los puntos finales críticos, el punto tricrítico y el punto triple en el comportamiento electrocalórico. Se proporciona el diagrama de fase de campo eléctrico - temperatura de BT. La contribución del calor latente, en la transición de fase de primer orden, inducida por el campo eléctrico, se sustrae del cambio de temperatura electrocalórica y con esto se demuestra que la mayor capacidad de respuesta electrocalórica se encuentra en el tipo de líquido - vapor del punto final crítico. Se calcula el diagrama de fase y el cambio de temperatura electrocalórica para $Ba(Zr_xTi_{1-x})O_3$. Asimismo, se calcula un diagrama de fase completo de composición-temperatura con la posición de un punto tricrítico y de un punto triple. Al considerar la línea de puntos finales críticos, se construye un diagrama de fase de campo eléctrico – composición - temperatura. Se demuestra que el punto triple tiene un efecto positivo en la mejora de las propiedades electrocalóricas, mientras que el punto tricrítico no tiene ningún efecto.

Se demuestra la estabilidad a largo plazo del cambio de temperatura electrocalórica y el efecto de la migración de vacantes de oxígeno. El movimiento de vacantes de oxígeno bajo fuertes campos eléctricos, conduce a un cambio en la química del defecto y, por lo tanto, a un aumento de la corriente de fuga y el calentamiento de Joule. Se demuestra que el mecanismo de conducción principal después de 10^6 ciclos electrocalóricos cambia de conductividad iónica a electrónica. Al cambiar la polaridad del campo eléctrico después de cada 10^5 ciclos, las vacantes de oxígeno se pueden redistribuir y se obtiene un gran número de ciclos de 10^6 sin disminuir el ECE.

Table of Figures

Abbreviations

BT	Barium titanate
BZ	Barium zirconate
BZT	Barium zirconate titanate
C	Cubic phase
DSC	Differential scanning calorimeter
EC	Electrocaloric
ECE	Electrocaloric effect
FE	Ferroelectric
HCFC	Hydrochlorofluorocarbon
HFC	Hydrofluorocarbon
O	Orthorhombic phase
PE	Paraelectric
PMN	Lead magnesium niobate
(1-*x*)PMN-*x*PT	Lead magnesium niobate – lead titanate
PNR	Polar nanoregion
PST	Lead scandium tantalate
R	Rhombohedral phase
RE	Relaxor ferroelectric
T	Tetragonal phase
TCP	Tricritical point
XRD	X-ray diffraction

1. Introduction

1.1. Preface

Refrigeration became an important part of modern lifestyle. The development of cooling techniques influenced our society from its beginning and a great advance for human benefit was achieved by air conditioner and refrigerator for foodstuffs. The vapor compression technique is still the dominant design for these systems. As a refrigerant Hydrochlorofluorocarbons (HCFC's) were used, which harm the ozone layer and contribute to atmospheric global warming. They were replaced by Hydrofluorocarbons (HFC's), which don't harm the ozone layer but still promote global warming. Nowadays, the most common refrigerant is R-600a, i.e. isobutane. This gas possesses a relatively low impact on global warming but cannot be used in large quantities due to its explosive risk. So efforts were made to develop new refrigeration techniques that upgrade artificial cooling, but at the same time limit or eliminate the environmental harm. Therefore, solids are a good prospect coolants, because of their higher mass density that allows for a higher energy density and in order to avoid the release of harmful gases.[1]

Electrocaloric (EC) materials give a promising alternative for new cooling systems. Refrigerators based on EC materials are assumed to have an efficiency of 60 % to 80 % and hence have the potential to replace conventional fridges (efficiency of 40-50 %) in the future.[1-3] Solid state cooler prototypes using an electrocaloric element have been already under investigation by few research groups[4-16], but the low electrocaloric effect (ECE) in these materials prevented practical use. For high performance solid-state coolers materials with a larger ECE need to be found.[17] Therefore, the aim of replacing vapor compression refrigerators by electrocaloric coolers is still a long path.

A more short-term objective for EC based solid-state coolers that might be reached is the inclusion into modern communication devices and computing equipment. Due to the rapid miniaturization an efficient heat rejection is a big challenge. The concentration of multiple active and passive components (e.g. transistors, capacitors,…) in a confined space makes it difficult to keep the single parts operate at intended temperatures, as heat is produced faster than it is dissipated. The temperature rise can lead to physical damage. Thus, miniaturized cooling systems are required to meet these challenges. Due to the large amount of energy consumption at continuous operation and difficult on-board installation, conventional vapor compression technology doesn't meet the required criteria. The utilization of solid refrigerants holds the potential benefits of larger heat extraction due to their larger mass and energy densities. Additionally, static operation and low maintenance may be other benefits.[1]

However, development of a practical electrocaloric refrigeration system is hindered by some main drawbacks that can be deduced from literature:

- Low adiabatic temperature change near room temperature
- Low isothermal entropy change
- Requirement of large electric fields

To eliminate those drawbacks it is necessary to explore the basics of the ECE, to be able to develop new materials with enhanced properties. Those work from material side might then enable engineers to build environmentally friendly and miniaturized cooling devices. Before giving some literature review about ferroelectrics (which are investigated throughout this work) and the electrocaloric effect, a short historical overview will be given.

Over the last years some review articles appeared giving a general overview of the ECE from the beginnings to nowadays development. [17-30] Despite, most of them starting with a short historical note or even giving some more detailed historical overview like Scott[21], only Moya[19] refers that the first mentioning of the ECE as an inverse of the pyroelectric effect was given by William Thomson M.A.[31], better known as Lord Kelvin, in 1877. A publication never mentioned in those review articles is the early experimental proof of the occurrence of a temperature change in a changing electric field by Straubel in 1902.[32] In this publication he proved qualitatively the heating and cooling effect in a brazilian tourmaline and gave an estimated temperature change in this pyroelectric crystal of 0.74 mK. The study was extended by Lange[33], a student of Straubel, in his doctoral dissertation in 1905. Here, a comprehensive overview about the thermodynamics are given in accordance to the theories by Lord Kelvin[34], Voigt[35, 36] and Riecke[37]. The equation for indirect estimation of the ECE (given later in the literature review), derived from Maxwell relations, is already set in early textbooks from Voigt[38] and Pockels[39]. Studies until then where done on pyroelectric materials, as ferroelectricity was not observed until 1920 (published 1921) by Valasek[40]. In 1930 then, a more deep investigation was done by Kobeko and Kurtschatov on ferroelectric Rochelle salt.[41] In their work they already made the connection between the temperature dependent dielectric constant and the ECE. Furthermore, they already observed the normal and inverse ECE and interpreted the heating of the sample under an ac electric field to be connected to dielectric losses. In addition they show the proportionality between the temperature change and the square of the polarization. By this they could determine the spontaneous polarization of Rochelle salt and find the Curie temperature. Even though the terms used here will be explained later on, it should be recognized that this was an important contribution to the research field of the ECE. Publications in the subsequent years were poor due to worldwide political conflicts. In the ‘60s and ‘70s several materials were investigated at low temperatures to evaluate suitability for cryogenic cooling.[42-49] Important to mention is the theoretical consideration of an energy conversion device by Childress, who described that the thermal conduction inside a ferroelectric material should be considered as a factor in the design of a device.[50] For the ECE at elevated temperatures, i.e. around room temperature and

higher, efforts were made by Thacher[51] and Tuttle & Payne[52, 53], who investigated lead-based compounds between 300 K and 450 K. They found EC temperature changes of 1 K and 2.2 K, respectively, at phase transitions between antiferroelectric or paraelectric and ferroelectric phases. In the '80s and '90s researcher from the Soviet Union worked on lead-based materials[54-57] which resulted in a functioning demonstrator of an EC device, built by Sinyavsky et al.[4, 5, 58, 59]. Until this time only few or even no publications appeared per year which can be seen from Figure 1.1.1 a). Before coming to the recently increased interest in the ECE for solid state cooling two important contributions should be mentioned which appeared around the turn of the millennium. In 1998, Xiao et al. found an substantial ECE in the nowadays often investigated (1-*x*)Pb($Mg_{1/3}Nb_{2/3}$)O_3-*x*$PbTiO_3$ [(1-*x*)PMN-*x*PT] solid solution.[60, 61] In 2002, Shebanov et al. investigated a multilayer structure in order to increase the applied electric field, which is nowadays a current research trend.[62] The progress in thin film technology enabled the ECE to become a "hot topic". Due to the fact that large electric fields can be applied to thin film structures, a large EC temperature change is observed for those. This was first published in Science by Mischenko et al., who calculated with an indirect approach a temperature change of 12 K for a $PbZr_{0.95}Ti_{0.05}O_3$ thin film.[63] Another publication in Science by Neese et al. two years later found similar temperature changes in ferroelectric polymer films.[64] Those two publications can be seen as the trigger for intensive investigations of the ECE from several research groups around the globe in the following years. Investigations focused not only on lead-based materials and polymers but also on lead-free materials. From Figure 1.1.1 a) can be seen that especially lead-free perovskite materials show a fast increase in publication numbers. Those materials are often studied for their piezoelectric properties at the same time. The publication numbers for lead-based materials show a more modest increase and interest in ferroelectric polymers might already decrease again. Taking a closer look to the type of samples investigated, see Figure 1.1.1 b), one can see that the research interest increased not solely on thin films, but also on bulk materials and multilayer structures. The latter ones are of particular interest as they feature substantial thermal capacitance and low operation voltages. A recent review by Moya et al. focuses on the EC performance of multilayers.[65] The increasing interest on EC solid state cooling can be as well seen from Figure 1.1.1 c) and d). After the report of giant ECE by Mischenko et al.[63] and Neese et al.[64], the increasing research interest lead to a better understanding of the ECE and material development. Several publications in high impact journals were published between 2013 and 2016, whereas in 2017 only one article appeared. The number of overview articles was large in 2012 and 2014 but in 2017 none appeared. It should be noted that numbers for 2018 are not included in Figure 1.1.1 (one review article appeared in MRS Bulletin[65]) but the statistics in Figure 1.1.1 c) and d) might be an indication that the amount of important findings is decreasing and a material scanning sets in. As indicated earlier there are two ways of determining the ECE: i) indirect method using Maxwell relations to calculate the EC temperature change and ii) direct method by measuring the EC temperature change.

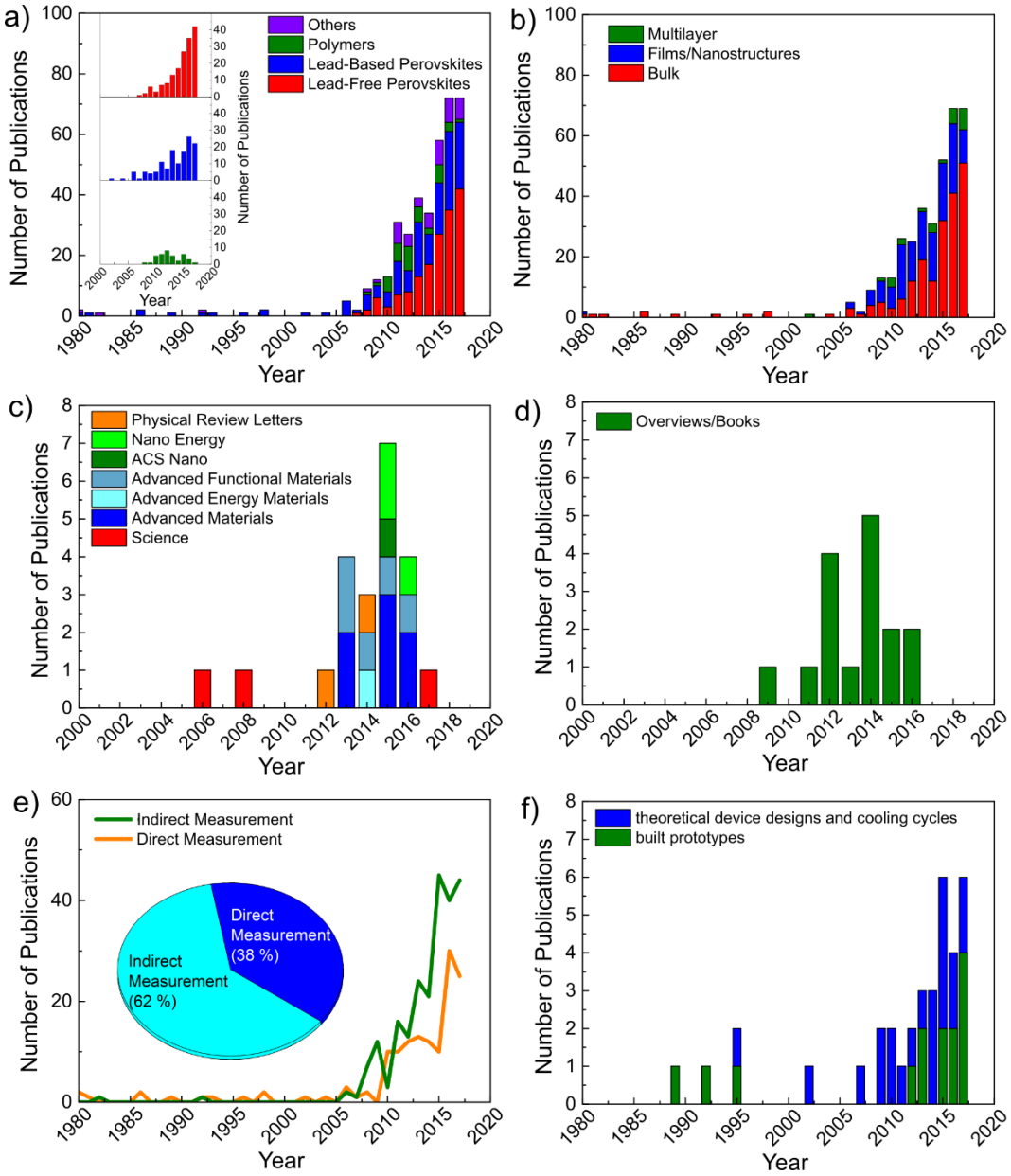

Fig. 1.1.1: Data is compiled from a search at Web of Science including „electrocaloric" in the title. a) Number of publications split between type of material. b) Number of publications split between type of sample dimension. c) Publications appeared in high impact factor journals, i.e. impact factor larger than 8. d) Number of overview articles and a book appeared in 2014. e) Number of publications using the indirect determination of the ECE or direct measurements. Inset: Indirect measurements against direct measurements overall. f) Number of publications dealing with built prototypes or theoretical considerations and thermodynamic cycles.

Direct measurements conducted accurately should be always preferred to indirect methods. While measurement set-ups exist that can determine the ECE in bulk and multilayer structures with a good accuracy, the direct measurement of thin films is difficult. The number of publications utilizing the indirect approach increased faster than the ones measuring directly, displayed in Figure 1.1.1 e). This onset of indirect measurements goes in accordance to the onset of investigated bulk and lead-free perovskite materials. It might be deduced that the research on the ECE benefit from the research on lead-

free piezoelectrics, where plenty of material compositions were available to measure indirectly the ECE. The overall share of direct and indirect investigations is depicted in the inset of Figure 1.1.1 e).

The importance of direct measurements is the subject of a whole review article by Liu et al..[28] The aim of almost all investigations is the future implementation of the ECE in a solid state cooling device. The status on theoretical considerations and built prototype devices is provided in Figure 1.1.1 f). As the early development of a prototype cooler was done by the group around Sinyavsky, it took long until more prototypes were built. In a natural manner the development of prototypes is shifted in time relating to the start of increased interest. However, the amount of built EC devices seems to increase and it will be of interest how much more prototypes will appear and if the ECE can be brought into commercialization.

Despite the large temperature changes observed in thin film structures, for mid-size and large scale cooling applications bulk or multilayer structures are needed, because of their bigger cooling capacity.[66-72] Therefore, research throughout this work was conducted on bulk ferroelectric materials. A common approach in the search for suitable EC materials is to obtain maximum EC properties at the temperature range of interest, i.e. mostly around room temperature and slightly elevated temperatures till 350 K. For cooling devices a certain operation temperature range is needed which makes it necessary that EC performance is stable across the desired temperature range. The temperature span of maximized EC performance in a material depends on its phase change characteristics, i.e. first order-, second order-, diffusive-, or relaxor-like phase transition. From application point of view, the achievable EC temperature change which drives the heat flow and determines the exchangeable energy is important. In addition, the cooling power is a key performance parameter which defines together with the electrical input energy the coefficient of performance. As an EC cooler will operate in a cyclic manner, the thermophysical properties of the EC material play a crucial role in extracting and absorbing heat. Those thermophysical properties are not well studied in electrocaloric materials. To clarify on which type of ferroelectric, i.e. first order-, second order-, relaxor-, or relaxor-like ferroelectric, future material development should focus on, considerations on the basis of material related cooling power must be included. In this work an equation for the material related cooling power is derived which can be used as a figure of merit for EC materials. Until now no such figure of merit is used for EC materials in comparison to thermoelectric materials. Furthermore, the electrocaloric as well as thermophysical properties of ferroelectrics with different phase change characteristics are elucidated, schematically shown in Figure 1.1.2. A barium titanate (BT)-based material system is chosen, i.e. $Ba(Zr_xTi_{1-x})O_3$, which shows a transition from first order-, to second order-, to diffusive, to relaxor-like characteristics with increasing amount of barium zirconate (BZ).[73] The obtained properties will be used to derive the materials measure of cooling power.

A comparison on basis of materials cooling power and not solely on EC temperature change will provide guidance in the development of new EC materials with improved EC performance.

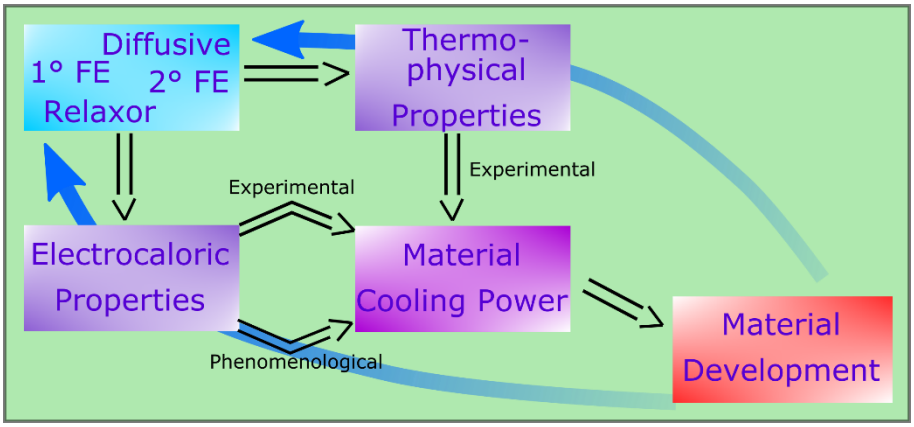

Fig. 1.1.2: Schematic of the main objective of this work. Ferroelectric (FE) materials with different phase change characteristics will be studied and thermophysical and electrocaloric properties will be measured and derived in the framework of the phenomenological theory. The obtained properties will be used for a comparison based on the material cooling power. This will help in the ongoing material development and can pave a way for the optimization of ferroelectric materials as electrocaloric refrigerants.

1.2. General View of Ferroelectricity

Ferroelectric materials are commercially used in several applications like piezoelectric devices[74-76], high-permittivity dielectrics[77-79], pyroelectric sensors[80-82], ferroelectric random access memories[83, 84] and positive temperature coefficient of resistivity components[85]. Furthermore, development of new devices using ferroelectric materials are under consideration, i.e. refrigerators[18, 20] or piezoelectric energy harvester[86, 87]. Due to the large capability of applications, ferroelectrics are called "smart" materials.[88] They show several possibilities of energy conversion (often with a direct and converse effect) giving the opportunity of actuating and sensing in the same material. To understand the general phenomena occurring in ferroelectrics this chapter describes some important concepts. Main focus is kept on essential concepts to understand the electrocaloric effect. After a brief description of dielectric (section 1.2.1.), electrostrictive (section 1.2.2.), piezoelectric (section 1.2.3.) and pyroelectric properties (section 1.2.4.), the principals of ferroelectricity (section 1.2.5., 1.2.6. and 1.2.7.) will be explained. Here, a focus is set on structural phase transitions (section 1.2.8.) and phenomenological description (section 1.2.9.) of those. Section 1.2. is completed with a description of relaxor ferroelectrics (RE) and their difference to ferroelectrics (section 1.2.10.). The information of the following sections (1.2.1 – 1.2.10) is taken from several textbooks by Uchino[88], Lines & Glass[89], Jona & Shirane[90], Jaffe & Cook & Jaffe[91], Samara[92], Newnham[93], Strukov & Levanyuk[94], and a review from Ahn et al.[95] and one from Damjanovic[96] if not otherwise indicated.

1.2.1. Dielectricity

In ionic crystals the application of an electric field will lead to a displacement of the ions either towards the cathode (cations) or to the anode (anions) due to electrostatic forces. The electron clouds will deform as well. This is known as electric polarization. The contribution to this electric polarization are electronic and ionic displacement as well as dipole reorientation.[93] The contribution to dielectric polarizability depends on the electric field frequency. Electrons, ions and dipoles can follow the alternating electric fields only until certain frequencies. This is typically 10^{12}-10^{15} Hz for electrons, 10^{9}-10^{12} Hz for ions and 10^{6}-10^{9} Hz for dipoles.[88] Considering a dielectric plate capacitor, the stored electric charge per unit area is called electric displacement (D_i) which is related to the electric field (E_i) as

$$D_i = \varepsilon_0 E_i + P_i, \tag{1.2.1}$$

where ε_0 is the vacuum permittivity (ε_0 = 8.854187817 x 10^{-12} F/m) and P_i is the induced polarization.[93] This shows the difference between an air-filled capacitor and a dielectric capacitor which is the dielectric polarization. The dielectric displacement in ferroelectric materials is determined by the dipolar polarization due to high dielectric susceptibility, i.e. the contribution from the vacuum

susceptibility can be neglected.[89] Therefore, throughout this work the dielectric displacement is set equal to the polarization, $D \cong P$. The induced polarization is proportional to the applied electric field and can be expressed as

$$P_i = \chi_{ij}\, \varepsilon_o\, E_j + P_s, \tag{1.2.2}$$

where χ_{ij} is the dielectric susceptibility and P_s the spontaneous polarization. The susceptibility can be expressed by the dielectric permittivity ($\chi_{ij} = \varepsilon_{ij} - 1$) which is more commonly used to describe the ability of a dielectric to store charge.

1.2.2. Electrostriction

An external applied electric field induces polarization in a dielectric material which is due to the displacement of the ions. With the displacement of the ions, the lattice gets distorted which results in an induced strain.[91] The induced strain is a result of the coupling between the electrical and mechanical properties. The quadratic relationship between the electric field and the mechanical properties is known as electrostriction.[94] To explain the phenomena of electrostriction a one-dimensional spring model of the crystal lattice can be considered.[88] The springs represent the cohesive forces from the electrostatic Coulomb energy and the quantum mechanical repulsive energy. In a centrosymmetric dielectric the springs are all the same due to equivalent ionic distances. If an applied electric field acts on the crystal the ionic distance between two cations (or anions) remain the same as the extension and contraction of the springs are nearly the same. The result will be no strain but the picture of idealized (harmonic) springs is not correct. In a harmonic spring the force F is the spring constant k times the displacement Δl ($F = k\, \Delta l$). In reality the springs possess anharmonicity ($F = k_1\, \Delta l - k_2\, \Delta l^2$). This means they are more easily to be extended than contracted. This results then in a strain (x_{ij}) which is independent on the direction of the applied electric field. The electrostrictive effect can be described by

$$x_{ij} = M_{ijkl}\, E_k\, E_l, \tag{1.2.3}$$

$$x_{ij} = Q_{ijkl}\, P_k\, P_l, \tag{1.2.4}$$

where M_{ijkl} and Q_{ijkl} are the electrostrictive tensors.[88] The electrostrictive coefficients are considered to be mainly temperature independent.[97]

Moreover, a converse electrostrictive effect exists relating an applied mechanical stress (X_{ij}) with dielectric permittivity as[88]

$$\Delta\left(\frac{1}{\varepsilon_0\, \varepsilon_{ij}}\right) = 2\, Q_{ijkl}\, X_k\, X_l. \tag{1.2.5}$$

1.2.3. Piezoelectricity

Not all dielectrics possess a centrosymmetric crystal structure throughout the whole temperature range. Some of them can exhibit a non-centrosymmetric crystal structure at lower temperatures. All non-centrosymmetric crystal structures are listed in Table 1.2.1.

Tab. 1.2.1: Crystallographic classification according to symmetry and polarity considerations. Notation is given with Hermann-Mauguin notation. Adapted from Uchino.[88] All point groups are piezoelectric and the 10 polar ones are also pyroelectric.

	Nonpolar	**Polar (pyroelectric)**
	Non-centrosymmetric	
Cubic	$\bar{4}3m, 23$	
Hexagonal	$622, \bar{6}m2, \bar{6}$	$6mm, 6$
Tetragonal	$422, \bar{4}2m, 4$	$4mm, 4$
Rhombohedral	32	$3m, 3$
Orthorhombic	222	$mm2$
Monoclinic		$2, m$
Triclinic		1

As in centrosymmetric crystals the bonds between the ions in non-centrosymmetric crystals are treated as springs.[88] However, the non-centrosymmetric structure causes different ionic distances (in other words anions and cations are connected alternating by hard and soft springs) as compared to a centrosymmetric structure. If an electric field is applied the soft and hard springs will contract and expand differently strong and change the distance between cations (or anions). Hence, in non-centrosymmetric crystal structures already the linear coupling term between the electric field and mechanical properties contribute to the strain.[94] Due to a linear relationship the strain changes the sign when the direction of the electric field changes, i.e. the material experiences contraction and elongation with changing the direction of the electric field.[91] The linear relationship between the electric field and strain is known as the converse piezoelectric field. The converse piezoelectric effect is expressed as[93]

$$x_{ij} = d_{ijk} E_k, \tag{1.2.6}$$

where d_{ijk} is the piezoelectric tensor. The direct piezoelectric effect describes the relation between the polarization induced by an external stress. This is expressed as[93]

$$P_i = d_{ijk} X_{jk}. \tag{1.2.7}$$

1.2.4. Pyroelectricity

Some of the piezoelectric crystal systems exhibit a charge generation during the change of temperature (heating and cooling). Only some of the crystal systems showing piezoelectric properties show pyroelectric properties as well, see Table 1.2.1. A necessary condition for pyroelectricity is a unique polar axis, i.e. a polar axis that is not compensated by other polar axes.[94] The uncompensated polar axis results in a permanent dipolar moment. This leads to a spontaneous polarization (P_s) and due to electrostriction a spontaneous strain (see Eq. 1.2.4). The pyroelectric effect can be expressed as[94]

$$\Delta P_i = p_i \, \Delta T, \tag{1.2.8}$$

where p_i is the pyroelectric coefficient. The converse effect is the electrocaloric effect and will be described in detail in section 1.3.. Like the piezoelectric effect, the pyroelectric effect is only possible in certain crystal systems due to symmetry considerations. This crystal systems are summarized in Table 1.2.1.

1.2.5. Ferroelectricity

Materials exhibiting ferroelectricity belong to the crystal systems showing pyroelectricity (see Table 1.2.1). In ferroelectric materials the direction of the spontaneous polarization can be reversed by the application of an electric field.[90] The occurrence of spontaneous polarization is related to the lattice vibrations at finite temperatures.[88] At high temperatures acoustic modes and optical modes are active resulting in ion shifts at a vibration frequency. Here, acoustic modes are not generating a dipolar moment and optical modes generate a dipolar moment. Particular modes can become stabilized if they reduce the crystal energy. Starting at a high temperature where all modes are active and decreasing the temperature the modes minimizing the crystal energy will be stabilized. This is accompanied by a decrease in vibration mode frequency and finally at a specific temperature this frequency becomes zero. The condensation of this mode is an essential concept of ferroelectricity and called soft phonon mode condensation.[89]

The occurrence of spontaneous polarization can be explained as well by energy minimization considerations. Due to the shift of ions from their original position a local field is generated that acts on neighboring ions. This dipolar coupling can be expressed as an energy term:[88]

$$W_{dip} = -\left(\frac{N\alpha\gamma^2}{9\varepsilon_0^2}\right) P^2. \tag{1.2.9}$$

Here N is the number of atoms per unit volume, α is the ionic polarizability, γ is the Lorentz factor. The shift of ions from the nonpolar position changes the elastic energy at the same time. The change in elastic energy can be expressed as[88]

$$W_{elas} = \left(\frac{k}{2Nq^2}\right) P^2 + \left(\frac{k\prime}{4N^3q^4}\right) P^4, \tag{1.2.10}$$

where k and k' are the force constants and q is the electric charge. Combining Equation 1.2.9 and 1.2.10 leads to the total energy:

$$W_{tot} = \left[\left(\frac{k}{2Nq^2}\right) - \left(\frac{N\alpha\gamma^2}{9\varepsilon_0^2}\right)\right] P^2 + \left[\frac{k'}{4N^3q^4}\right] P^4. \tag{1.2.11}$$

The functions of energy versus the polarization are schematically shown in Figure 1.2.1. It can be seen that the polarization is zero if the coefficient of the harmonic term of elastic energy is equal or greater than the coefficient of dipolar coupling. In this case the ions will not shift from their nonpolar position and no spontaneous polarization occurs. If the coefficient from dipolar coupling is greater, then the ions will shift to a polar position inducing a spontaneous polarization. The polarizability might be temperature dependent leading to a transition from a nonpolar phase to a polar phase during temperature decrease.[88] The high temperature nonpolar phase is termed paraelectric (PE) and the lower temperature polar phase is termed ferroelectric. From the one-dimensional picture in Figure 1.2.1 can be seen that two stable configurations in the total energy exist. This refers to the polarization in antiparallel directions. An external electric field can switch the ions between those minima which is a necessary condition for ferroelectrics.

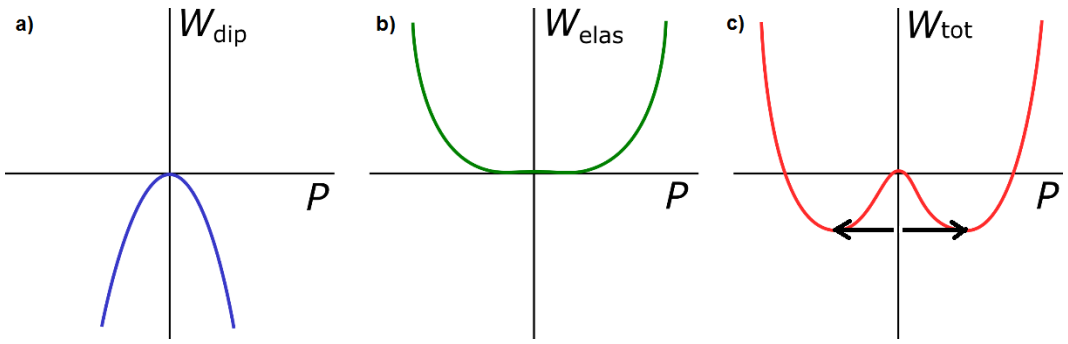

Fig. 1.2.1: Schematic of a) the dipolar energy, W_{dip},b) the elastic energy, W_{elas}, and c) the combined total energy, W_{tot}.

1.2.6. Ferroelectric Domains

If a ferroelectric crystal is cooled from the high temperature paraelectric phase down to the ferroelectric phase the spontaneous polarization appears. The dipolar displacement can only occur in certain directions depending on the crystallographic structure.[93] In case the spontaneous polarization vector of all dipoles in the volume would show into the same direction, a large depolarizing field will occur due

to the uncompensated dipole moments at the surfaces of the crystal. The depolarization field (E_{dep}) can be very large and in the order of 10^5 V mm^{-1}.[89] A compensation can be obtained by free charges inside the crystal or from the surrounding. Those compensating charge carriers can lead to an extinction of the field inside the bulk and outside the crystal but not necessarily right below the crystal surface.[89] Due to the fact that a ferroelectric must have at least two stable displacement directions, the spontaneous polarization will occur along different directions during the cooling from paraelectric to ferroelectric phase. The direction of the spontaneous polarization will be equal in a certain volume which is called a domain.[96] Two neighboring domains with different spontaneous polarization directions are separated by a domain wall. These walls differ from the perfect crystal and therefore need a certain amount of energy to build up.[89] The final domain configuration in the crystal is then determined by minimizing the energy related to the electrostatic energy (from depolarization field) and the domain wall energy. It should be noted that the angles of the polar vectors between two neighboring domains are restricted by the crystal structure.[96] It is possible for all crystal structures that the neighboring domains have antiparallel polarization vectors, i.e. 180° domain walls. Furthermore, in tetragonal (4mm) crystal systems 90° domain walls are possible, in orthorhombic (mm) systems 60°, 90° and 120° domain walls are possible and in rhombohedral (3m) systems 71° and 109° domain walls are possible.

1.2.7. Polarization Reversal

A distinct feature of ferroelectric materials is the occurrence of a polarization hysteresis loop under the reversal of an electric field. The hysteresis loop results from the ability of the domains to orientate in the direction of the applied electric field.[96] A schematic hysteresis loop is shown in Figure 1.2.2. After cooling the ferroelectric crystal from the paraelectric phase to the ferroelectric phase a multidomain state is established due to the large depolarization field (see section 1.2.6.) and the macroscopic polarization is zero. If an applied electric field is increased the domains, with polarization not pointing in the direction of the applied electric field, will switch towards the direction of the electric field. This gives rise to a large measureable polarization change. Once the domains are aligned to the electric field linear behavior can be observed. The extrapolation of linear polarization response towards zero electric field gives the value of the spontaneous polarization for single crystals.[96] If the applied electric field is decreased towards zero field some domains will back-switch. The remaining polarization at zero field is called remanent polarization (P_r). If the electric field is applied in the opposite direction the majority of domains will reverse at the coercive field (E_c) to align along the new electric field direction. The area within the hysteresis loop gives a measure of the energy losses related to the switching of domains.[96]

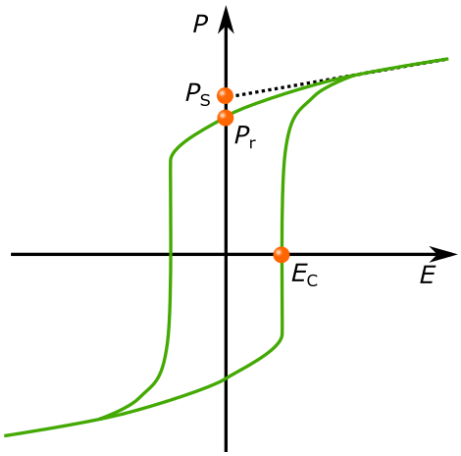

Fig. 1.2.2: Schematic of the polarization electric field behavior of a ferroelectric material.

1.2.8. Phase Transitions

At high temperature ferroelectrics exhibit a non-polar paraelectric phase which is transformed into a polar ferroelectric phase at a reduced temperature. The transition from paraelectric to ferroelectric phase takes place at a specific temperature, called Curie temperature (T_C), which is accompanied with the onset of a polarization and strain, called spontaneous polarization (P_S) and spontaneous strain (x_S). With decreasing temperature, interferroelectric transitions can occur at which the crystal structure and the direction of the polar axis change. Considering the soft phonon explanation (see section 1.2.5.) the soft mode frequency varies with temperature approaching zero at the phase transition.[89] This temperature dependency can be expressed as

$$\omega_T^2 = K\,(T - T_C), \tag{1.2.12}$$

where ω_T is the phonon mode frequency, K a constant and T_C the Curie temperature. The phonon frequency can be related to the static dielectric constant by the Lyddane-Sachs-Teller relationship.[89] It follows a temperature dependency of the static dielectric permittivity as

$$\varepsilon'(0) = \frac{C}{(T-T_C)}. \tag{1.2.13}$$

This is the Curie-Weiss temperature dependence of the static dielectric permittivity observed in ferroelectrics above the phase transition.[89] Accordingly the coefficient C is the Curie constant. A more general view about phase transitions can be obtained from thermodynamic considerations. A thermodynamic potential gives a full description of a thermodynamic system in equilibrium. If a system is in the equilibrium state, at constant pressure, and temperature the Gibbs free energy (G) is at a minimum. The Gibbs free energy can be expressed as[94]

$$G = U - TS - X_i x_i - E_i P_i, \tag{1.2.14}$$

where U is the internal energy and S the entropy. At T_C the Gibbs free energy of phase A and phase B are equal. If the temperature is slightly varied, G of one phase is lower than the other and this phase becomes more stable. From the Gibbs free energy the behavior of entropy and specific heat can be derived by differentiation of G over the temperature.[94]

$$S = -\left(\frac{\partial G}{\partial T}\right)_E, \tag{1.2.15}$$

$$c_p = T\left(\frac{\partial S}{\partial T}\right)_E. \tag{1.2.16}$$

The phase transition can be of first or second order and is classified by the derivative of G, see Figure 1.2.3. If the first derivative shows discontinuity the phase transition is termed first order. If the discontinuity occurs in the second derivative of G it is termed second order phase transition.[94] For a first order phase transition follows that the entropy is discontinuous. For a second order phase transition follows that the entropy change is continuous and the heat capacity is discontinuous.

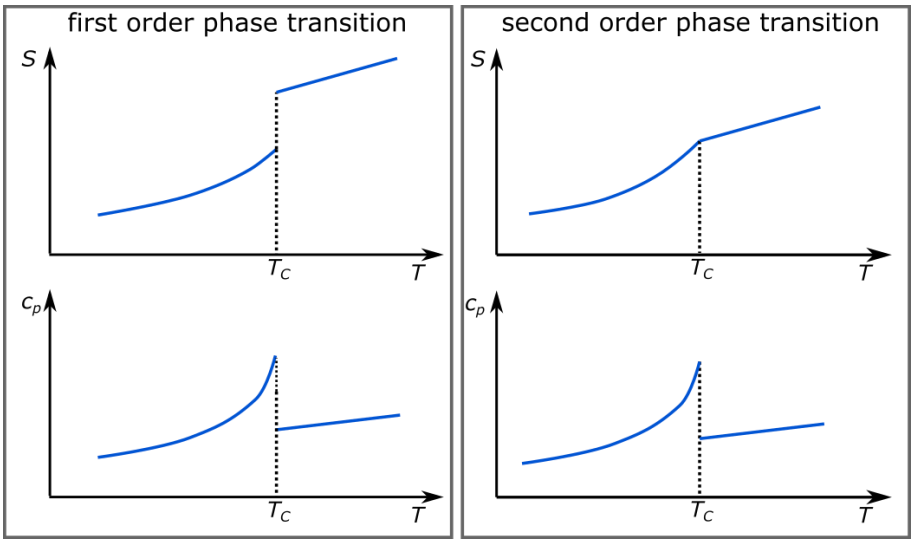

Fig. 1.2.3: Schematic of the entropy and heat capacity change at a first and second order phase transition.

1.2.9. Phenomenological Theory of Ferroelectric Phase Transitions

Ferroelectric properties in the region of the phase transition can be described by phenomenological theory. This theory is purely macroscopic and gives no information about the physical mechanisms. As a starting point a polynomial expansion of the Gibbs free energy (Equation 1.2.14) expressed as a deviation from a prototype state without spontaneous polarization and spontaneous strain, i.e. $P_s = x_s = 0$, is used.[94] For simplification reasons the assumption is made that the polarization in the ferroelectric

phase is directed only along one of the crystallographic axes, all stresses are zero and the non-polar phase is centrosymmetric. It follows for the Landau polynomial in the Devonshire form:[98] [99]

$$G_1 = \left(\frac{A}{2}\right) P^2 + \left(\frac{B}{4}\right) P^4. \tag{1.2.17}$$

The polynomial is truncated to the fourth order for simplicity. The coefficient A is temperature dependent and the coefficient B is assumed to be temperature independent. This assumption is working fine to describe a simple second order phase transition. The minimization of G_1 with respect to the polarization gives the equation of state

$$E = AP + BP^3, \tag{1.2.18}$$

where E is the Maxwell field. The stable state can be deduced from the minimum in G_1, $\partial G_1/\partial P = 0$. For the second order phase transition B is positive and if A is positive as well the only stable state is corresponding to $P = 0$, i.e. the non-polar state. At the point where the temperature dependent variable A changes from positive to negative G_1 will develop a maximum at $P = 0$ and two minima at $P \neq 0$. Near the Curie temperature A behaves linear:

$$A = A_0(T - T_C) = \left(\frac{1}{\varepsilon}\right)_{T>T_C}. \tag{1.2.19}$$

The spontaneous polarization and the dielectric permittivity in the polar phase (below T_c) can be expressed as[89]

$$P_S^2 = \frac{A_0(T-T_C)}{B}, \tag{1.2.20}$$

and

$$\frac{1}{\varepsilon} = 2A_0(T_c - T). \tag{1.2.21}$$

The temperature dependencies are qualitatively shown in Figure 1.2.4. Equations 1.2.19 and 1.2.21 show that the reciprocal permittivity changes the slope from positive to negative and is twice as large in the polar phase as in the non-polar phase. The phenomenological theory gives also a description of zero-field entropy and zero-field specific heat as a deviation from the high temperature symmetric phase with S^0 and c_p^0 being the entropy and specific heat capacity of the symmetric phase:[89]

$$S = S^0 - \frac{1}{2}A_0 P_S^2, \tag{1.2.22}$$

and

$$c_p = c_p^0 + \frac{A_0^2 T}{2B\rho}. \tag{1.2.23}$$

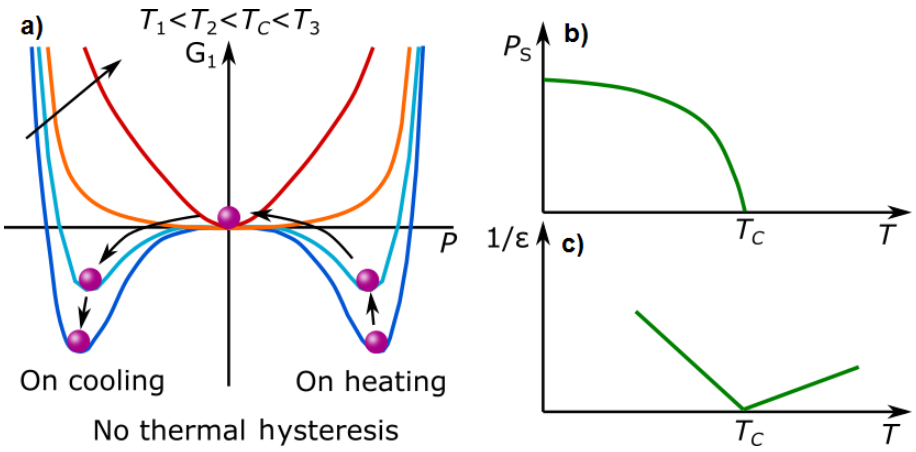

Fig. 1.2.4: a) Landau energy, b) polarization and c) reciprocal permittivity as a function of temperature for a ferroelectric second order phase transition.

Considering now a first order phase transition the coefficient B is negative. To ensure stability in the ferroelectric phase, it is necessary to take into account a sixth order expansion term in Equation 1.2.17.

$$G_1 = \left(\frac{A}{2}\right)P^2 + \left(\frac{B}{4}\right)P^4 + \left(\frac{C}{6}\right)P^6. \tag{1.2.25}$$

The coefficient C must be positive for stability reasons and it follows:

$$E = AP + BP^3 + CP^5. \tag{1.2.26}$$

Now it is possible to obtain a minimum in G_1 at $P = 0$ and two minima for $P \neq 0$ for $A > 0$. The coefficient A can still be written in the Curie-Weiss form as[89]

$$A = A_0(T - T_0), \tag{1.2.27}$$

but now T_0 is called Curie-Weiss temperature and is not equal to the transition temperature T_c. At T_c the three minima become equal and the stable state will discontinuously jump from $P = 0$ to $P = \pm P_s$, see Figure 1.2.5. For ferroelectrics with a first order phase transition a temperature range exists from T_0 to T_C^* where the ferroelectric and paraelectric phase can coexist as stable or metastable phases. The temperature T_0 denotes the lowest temperature where the paraelectric phase can exist and the temperature T_C^* denotes the highest temperature where the ferroelectric phase can exist.[94] The spontaneous polarization in the ferroelectric phase can be expressed as:[89]

$$P_s^2 = \frac{-B \pm \sqrt{B^2 - 4A_0(T - T_0)C}}{2C}. \tag{1.2.28}$$

The reciprocal permittivity is discontinuous at T_c and exhibits different slopes depending if T_c is approached from lower temperatures (spontaneous polarization contributes) or from higher temperatures.[89]

$$\left(\frac{1}{\varepsilon}\right)_{T\to T_c^-} = \frac{3B^2}{4C} + 8A_0(T_c - T), \tag{1.2.29}$$

or

$$\left(\frac{1}{\varepsilon}\right)_{T\to T_c^+} = \frac{3B^2}{16C} + A_0(T - T_c). \tag{1.2.30}$$

This shows that the slope of the reciprocal permittivity is eight times higher below T_c than above.[89] The discontinuity in spontaneous polarization is reflected in the discontinuity of entropy at the phase transition and hence a latent heat occurs. The entropy discontinuity can be expressed as[89]

$$\Delta S(T_C) = \frac{1}{2}A_0P_s^2. \tag{1.2.31}$$

The resulting discontinuous enthalpy is then:[89]

$$\Delta H_L(T_C) = \frac{1}{2}T_cA_0P_s^2. \tag{1.2.32}$$

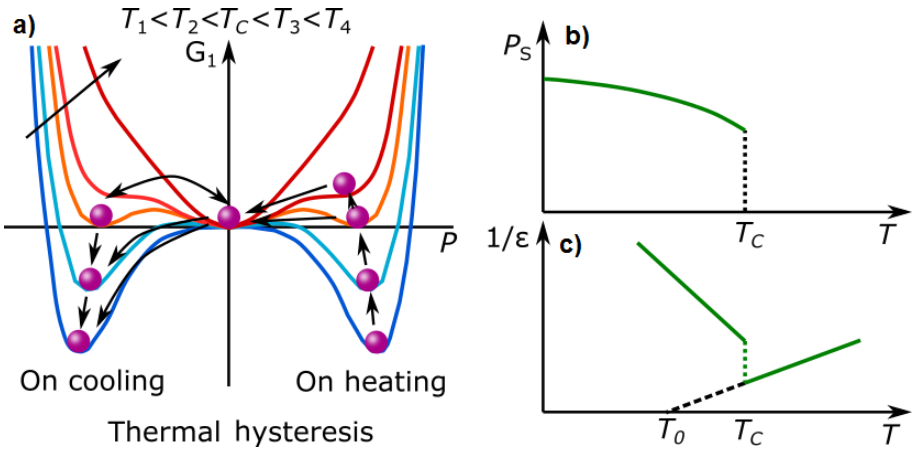

Fig. 1.2.5: a) Landau energy, b) polarization and c) reciprocal permittivity as a function of temperature for a ferroelectric first order phase transition.

1.2.10. Relaxor Ferroelectrics

Relaxor ferroelectrics or often just relaxors (REs) are a subclass of ferroelectrics. Some macroscopic features can be observed that distinguish them from classical ferroelectric materials. Several theories were developed over the years to explain the origin of the occurrence of relaxor properties. In this

section, first the macroscopic differences between ferroelectrics and REs will be described, as they are more accessible and of importance for applications. Later on some important theories will be introduced.

Beforehand, classical ferroelectrics with two kinds of phase transitions were discussed. In terms of the dielectric permittivity, they exhibit one big difference. First order phase transition results in a finite dielectric permittivity during the transition and second order phase transition in an infinitive value. But both share a common feature, that the Curie point is a singular point with respect to the dielectric permittivity. However, in comparison with classical ferroelectrics, REs exhibit a macroscopically different temperature evolution of dielectric permittivity and polarization. Cross[100], who introduced the name relaxor ferroelectrics, defined three peculiar characteristics for REs: (i) A broad and smeared maximum dielectric permittivity. (ii) A frequency dependence of the maximum dielectric permittivity temperature (T_m). (iii) No macroscopic symmetry breaking at T_m. These RE characteristics are commonly used to define a material as a RE. Other peculiar characteristics can be found with respect to the polarization behavior. Instead of a vanishing spontaneous polarization at T_C, REs exhibit a spontaneous polarization at temperatures far above T_m.[92] The polarization loops of RE's display different shape with changing temperature, i.e. square shaped at low temperatures, pinched loops at intermediate temperatures and then slim loops at higher temperatures.[92, 95] The comparison of dielectric permittivity, spontaneous polarization and hysteresis loops between classical ferroelectrics and RE's are displayed in Figure 1.2.6. Regarding the physical explanations for the observed phenomena several attempts were made but none of them seem to satisfactorily explain all the observed behaviors in the different lead-based and lead-free REs.

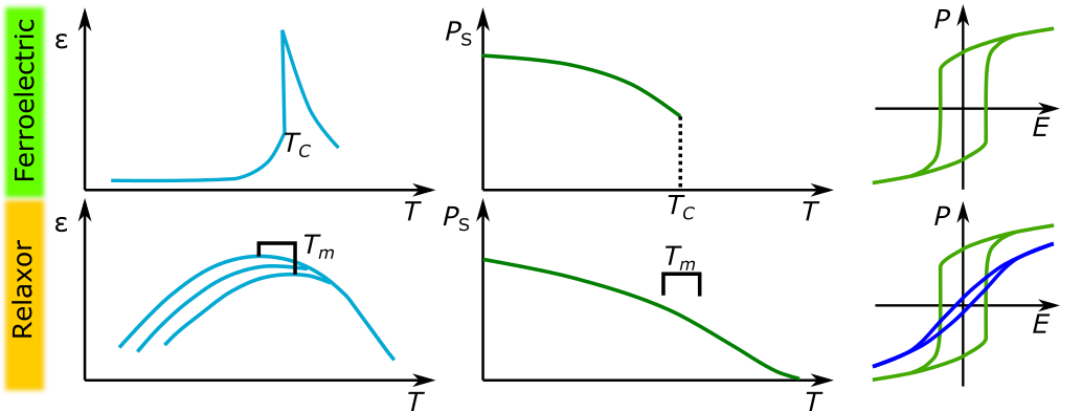

Fig. 1.2.6: Schematic relative permittivity, spontaneous polarization and polarization – electric field loops for a ferroelectric and relaxor material. Note that the transition temperature T_m is not connected to a structural transition.

Starting at the early discovery of a RE system, i.e. $Pb(Mg_{1/3}Nb_{2/3})O_3$ (PMN), by Smolenskii et al.[101, 102] in 1954, theories were derived to explain the different behavior of REs in comparison to ferroelectrics. Smolenskii proposed that the dielectric behavior originates from a diffuse phase transition which is caused by compositional heterogeneity. In the case of PMN it would mean that Mg^{2+} and Nb^{5+} are

irregularly distributed. The resulting ordered and disordered regions with varying sizes lead to different Curie temperatures for every of those regions and therefore, the diffuse phase transition behavior. This was supported by results from Setter and Cross[103, 104] on $Pb(Sc_{1/2}Ta_{1/2})O_3$ (PST). They demonstrated how the diffuse phase transition gradually disappears, dependent on the degree of ordering of the B-site cation. Treating the findings mathematically it was empirically found that a quadratic dependence exists between the reciprocal dielectric permittivity and temperature above T_m.[105] This relation is still widely in use to describe REs due to its similarity to the Curie-Weiss law and therefore is given here:

$$\frac{1}{\varepsilon'} - \frac{1}{\varepsilon'_m} = \frac{(T-T_\theta)^2}{2\varepsilon'_m\delta^2}. \tag{1.2.33}$$

Here, ε'_m, T_θ and δ describe the dielectric permittivity at T_m, a mean Curie temperature and a standard deviation, respectively. The idea of superimposed phase transitions with different Curie temperatures was questioned by Cross[100] in 1987. He agreed with the idea of chemical heterogeneity at a nanoscale level resulting in the polar nanoregions (PNRs). In his explanation, he considered that ferroelectricity is a cooperative phenomenon and scales with the volume of PNRs. For a certain volume the ferroelectricity will break down at a certain temperature due to thermal motion. This means that the thermal energy exceeds the energy barrier for polarization switching along equivalent directions. He called the state at which this happens the superparaelectric state. This means that at temperatures above T_m PNRs are highly dynamic with a rapid switching of polarization among the equivalent states. One significant result from this model is that the local symmetry of PNRs is lower than the global symmetry. As this model by Cross gave further inside into the physics of REs, it only focuses on the temperatures above T_m and gives no explanation about the frequency dispersion at lower temperatures. Continuing from Cross's superparaelectric model, it was assumed that during cooling of an RE at one point dielectric relaxation will slow down and become frozen.[92] Analyzing the characteristic relaxation times it followed that the Arrhenius-type analysis gave unreasonable values. Whereas, using a modified Arrhenius-equation, i.e. Vogel-Fulcher relation, gave reasonable values. The Vogel-Fulcher equation was introduced by Vogel[106], Fulcher[107] and Tammann[108] to explain glass transition phenomena. Applied to the frequency behavior of dielectric permittivity maximum it is written as,

$$\omega = \omega_0 \exp\left(-\frac{E_A}{k_B(T-T_{VF})}\right). \tag{1.2.34}$$

Here, ω, ω_0, E_A, k_B, T_{VF} are the measurement frequency, the Debye frequency, the activation energy barrier, the Boltzmann constant and the Vogel-Fulcher temperature. The Vogel-Fulcher equation can be seen as an equation for thermally activated processes, whereas the Arrhenius equation is a special case, where T_{VF} is 0 K. Often T_{VF} is related to be the freezing temperature (T_f) below which the RE is in a glass-like state.[92] This means that the thermal motion of the majority of PNRs reduces and long-range

order can be established by the application of an external electric field. The behavior in this case will be the same as that of a ferroelectric material. An electric field induced phase transition from a relaxor into a ferroelectric phase is a distinct feature of REs. Below T_f the electric field induced phase transition is metastable over time and the relaxor is called nonergodic. Above T_f the thermal activation is strong enough to lead to a reversible phase transition between the electric field induced ferroelectric phase and the RE phase and the relaxor is called ergodic.[92]

1.3. The Electrocaloric Effect

The electrocaloric effect is the reverse of the pyroelectric effect. Hence, all crystal structures that exhibit pyroelectricity also exhibit the ECE. Ferroelectrics are a subgroup of pyroelectric materials with typically large pyroelectric coefficients. Therefore, FEs are expected to be good EC materials. The ECE couples a change in the applied electric field to a temperature change in the material. If the change in the applied electric field takes place under adiabatic conditions, i.e. no heat exchange with the environment, the EC material heats up or cools down for electric field application or withdrawal, respectively. With a suitable heat transfer management the cooling part can be used for cooling of hot spots in electronics.[30]

On the macroscopic scale the electrocaloric effect can be explained by entropy exchanges. Similar as for the magnetocaloric effect the total entropy of a pyroelectric material can be expressed as the sum of two subsystems, i.e. dipolar entropy and lattice entropy.[109-112] The dipolar entropy is related to the dipolar ordering and the lattice entropy is related to the thermal vibration of the lattice. The dipolar entropy subsystem can be influenced by the change of the applied electric field. Under adiabatic conditions the change in the dipolar entropy will be compensated by a change in the lattice entropy and hence a change in the material temperature. For most materials the temperature will increase when the electric field is applied, see Figure 1.3.1. If the electric field is then held constant, the material can exchange heat with the environment until the driving force of temperature difference between material and environment vanishes. A removal of the applied electric field leads then to a decrease in the material temperature.

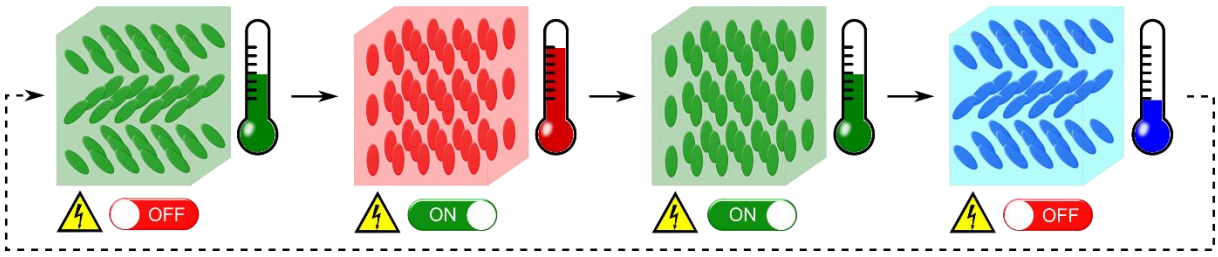

Fig. 1.3.1: Schematic of the electrocaloric effect under application and removal of an electric field in a pyroelectric material.

In the following chapters the background of the ECE is explained. First the theoretical description is developed (section 1.3.1.) and then some general considerations of the ECE in perovskites are given (section 1.3.2.). This is continued by the consideration of an EC cooling cycle and the resultant material measures of performance (section 1.3.3.). Further, attention will be given to the degradation behavior of EC materials as an important factor for long term usage of EC elements (section 1.3.4.). In the end the $Ba(Zr_xTi_{1-x})O_3$ system is introduced as an interesting material to study (section 1.3.5.).

1.3.1. Theoretical Description of the Electrocaloric Effect

The electrocaloric effect in ferroelectric materials is related to the entropy change of the subsystems. Therefore, the ECE can be described by using the first and second law of thermodynamics and change in the internal energy. First, a description is derived from Maxwell relations as this is commonly used to indirectly evaluate the EC temperature change from electric field dependent polarization measurements. A deeper understanding of the ECE can be gained from a phenomenological approach described in the second part of this section. This section is based on a review paper by Kutnjak et al.[18] and books from Grindlay[113] and Correia & Zhang[1].

A description of the ECE can be derived starting from the Gibbs free energy *G* for a pyroelectric material. The vectors x_i, X_i, P_i and E_i are written as scalars for simplification.

$$dG = -SdT - xdX - PdE. \tag{1.3.1}$$

The relations for the thermal, elastic and dielectric responses of the system are:

$$S = -\left(\frac{\partial G}{\partial T}\right)_{X,E}; x = -\left(\frac{\partial G}{\partial X}\right)_{T,E}; P = -\left(\frac{\partial G}{\partial E}\right)_{T,X}. \tag{1.3.2}$$

The Maxwell relation can be derived for the variable pairs (*S,T*) and (*P, E*)

$$\left(\frac{\partial S}{\partial E}\right)_{T,X} = \left(\frac{\partial P}{\partial T}\right)_{E,X}. \tag{1.3.3}$$

From equations 1.3.1 to 1.3.3 the entropy change during an adiabatic process can be derived for constant stress *X*.

$$dS = \left(\frac{\partial S}{\partial E}\right)_T dE + \left(\frac{\partial S}{\partial T}\right)_E dT = 0. \tag{1.3.4}$$

From this follows that:

$$\left(\frac{dT}{dE}\right)_S = -\frac{T}{\rho \cdot c_E}\left(\frac{\partial P}{\partial T}\right)_E = -\frac{T}{\rho \cdot c_E} p_E \quad . \tag{1.3.5}$$

In equation 1.3.5 the specific heat capacity at constant electric field is described as c_E and $p_E = (\partial P/\partial T)_E$ is the pyroelectric coefficient at constant electric field. The adiabatic temperature change can now be obtained by formal integration of Equation 1.3.5.

$$\Delta T = -\int_{E_1}^{E_2} \frac{T}{\rho \cdot c_E\,(E,T)} \left(\frac{\partial P}{\partial T}\right)_E dE. \tag{1.3.6}$$

From equation 1.3.5 and 1.3.6 can be deduced that large electrocaloric temperature changes can be achieved if the pyroelectric material possesses a high pyroelectric coefficient. Some values of pyroelectric coefficients are given in table 1.3.1. It can be seen that poled ceramics of the perovskite structure exhibit good pyroelectric properties.

Tab. 1.3.1: Materials selection with their crystal structure, symmetry and pyroelectric coefficient.[93]

Material	**Crystal Structure**	**Crystal Symmetry**	**p_E at 298 K (μC m^{-2} K^{-1})**
Poled Ceramics			
$BaTiO_3$	perovskite	Tetragonal, 4*mm*	-260
$Pb(Zr_{0.95}Ti_{0.05})O_3$	perovskite	Trigonal, 3*m*	-306
Crystals			
$LiNbO_3$	Corundum derivative	Trigonal, 3*m*	-96
$LiTaO_3$	Corundum derivative	Trigonal, 3*m*	-175
$(Ba_{0.5}Sr_{0.5})Nb_2O_6$	Tungsten Bronze	Tetragonal, 4*mm*	-502
$SrBi_2Ta_2O_9$	Aurivillius	Orthorhombic, *mm*2	-240
ZnO	Wurtzite	Hexagonal, 6*mm*	-6.9
polyvinylidene difluoride	Molecular Solid	Orthorhombic, *mm*2	-40

Using equation 1.3.6 it is possible to estimate the electrocaloric temperature change by measuring the polarization as a function of temperature and electric field. Problems may arise if the system undergoes a phase transition which leads to singularities in P(E, T) and c_E(E, T). The magnitude of the electrocaloric temperature change obtained by this indirect method should be tested by direct measurements.

A second path to derive the EC temperature change ΔT is by using the phenomenological theory. Again the stress is set constant. The isothermal equation of state, i.e. $E = E(T, P)$, is inserted into the Maxwell relation,

$$\left(\frac{\partial S}{\partial P}\right)_T = \left(\frac{\partial E}{\partial T}\right)_E, \tag{1.3.7}$$

and by integrating with respect to P it follows:

$$S(T, P) = -\int \frac{\partial E(T,P)}{\partial T}\, dP + S^0(T). \tag{1.3.8}$$

From equation 1.3.8 can be seen that the entropy has two contributions. One is related to the isothermal dielectric equation of state and the other part $S^0(T)$ not. The total entropy of the system can be written as the sum of the two components.

$$S\,(T,P) = S_{dip}\,(T,P) + S_{latt}\,(T)\,. \tag{1.3.9}$$

In ferroelectric materials the dipolar part is associated with ionic displacements, whereas in relaxor ferroelectric materials the dipolar part is related to the polar nanoregions. If the isothermal equation of state is formulated as,

$$E = A_0(T - T_0)P + BP^3 + CP^5, \tag{1.3.10}$$

and substituted in equation 1.3.8, it follows for B and C temperature independent,

$$S(T,P) = -\frac{A_0 P^2}{2} + S^0(T). \tag{1.3.11}$$

If an electric field is applied adiabatically the EC material transforms from a state $E = 0, T = T_i$ and $P = P_i$ to a state $E \neq 0, T = T_f$ and $P = P_f$. The total entropy change must be zero,

$$\Delta S\,(T,P) = \Delta S_{dip}\,(T,P) + \Delta S_{latt}\,(T) = 0. \tag{1.3.12}$$

Inserting equation 1.3.11 leads to,

$$-\frac{A_0}{2}{P_i}^2 + S^0(T_i) = -\frac{A_0}{2}{P_f}^2 + S^0(T_f), \tag{1.3.13}$$

or,

$$S^0(T_f) - S^0(T_i) = \frac{A_0}{2}[{P_f}^2 - {P_i}^2]. \tag{1.3.14}$$

Equation 1.3.14 determines the isentropic curve in the $P - T$ plane, demonstrated in Figure 1.3.2 a). Assuming that S^0(T) is a smooth function of T, $S^0(T_f)$ may be expanded in terms of $(T_f - T_i)$ leading to,

$$\left[\left(\frac{\partial S^0}{\partial T}\right)\Big|_{T=T_i}\right](T_f - T_i) = \frac{A_0}{2}[{P_f}^2 - {P_i}^2], \tag{1.3.15}$$

or,

$$(T_f - T_i) = \frac{A_0 T_i}{2\rho c_P(T_i)}[{P_f}^2 - {P_i}^2] = \Delta T. \tag{1.3.16}$$

Here, c_P is the specific heat capacity at constant polarization. Thus, for a fixed T_i the plot of ΔT versus ${P_f}^2$ is a straight line, depicted in Figure 1.3.2 b), with a slope of $A_0 T_i / 2\rho c_P(T_i)$ and an intercept at ${P_i}^2$.

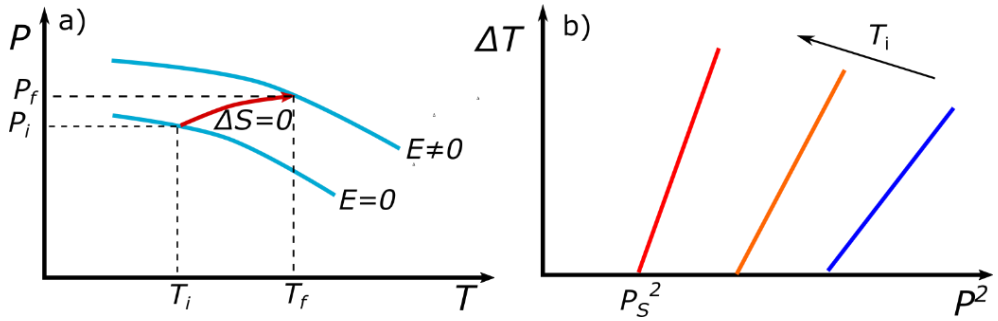

Fig. 1.3.2: a) *P-T* plane displaying schematically the isentropic change in polarization and temperature under the application of an electric field. b) Relationship between the electrocaloric temperature change and the quadratic polarization. The crossing with the x-axis is the quadratic spontaneous polarization.

1.3.2. The Electrocaloric Effect in Ferroelectrics

Many research was done on ceramic and polymer pyroelectric systems with respect to the ECE. The research spans from bulk materials to thick and thin films, as well as multilayer structures (see Figure 1.1.1). For bulk materials different structures were investigated, like perovskites, pyrochlores, aurivillius phases, tungsten bronzes or salts.[1] The focus is set to the perovskite structure, which is of main interest in ferroelectric investigations and applications. Some characteristics important for the EC performance are described.

As stated in Section 1.2.8. the paraelectric to ferroelectric phase transition can be of first or second order nature. In the case of first order nature the entropy will change discontinuously and in the case of a second order nature the change will be gradually.[113] Therefore, a latent heat will contribute to the temperature change in FEs with first order phase transition.[53, 62, 114] A drawback is that the operational temperature range of the first order phase transition is rather narrow.[30, 115, 116] In addition the initial nature of the phase transition can be altered by the application of strong electric fields (towards second order nature).[117] A second order phase transition provides wider operational ranges, but there is no contribution to the temperature change from a latent heat.[118] For relaxor ferroelectrics the electric field induced phase transition plays a crucial role.[110] In the thermally annealed state, the transition from relaxor phase to ferroelectric phase is typically of first order, accompanied by released latent heat.[119, 120] This holds for temperatures below the liquid vapor type of critical end point of the relaxor system.[121] The released latent heat can account for a major part of the adiabatic temperature change.[122] It should be noted, that in the nonergodic relaxor phase temperature range the electric field induced phase transition is irreversible upon electric field removal[123] and therefore cannot add to the cooling of the material. Above the temperature induced ferroelectric to relaxor transition, i.e. in the ergodic relaxor phase, the electric field induced phase transition is reversible[123] and therefore additional cooling is reached due to the absorbed latent heat. The influence of the latent heat gets weaker as the temperature

is increased towards the critical end point, which is of second order nature.[121] The effect of the electric field induced phase transition is crucial in the enhancement of relaxor EC performance over broad temperature ranges. Nevertheless, the largest ECE responsivity, i.e. temperature change over electric field change, can be found at the critical end point.[111] Here, the energy required for electric field induced polarization rotations is largely reduced, giving rise for large ECE.[121] The concept of energy minimization between different phases can be observed as well at morphotropic phase boundaries.[124-126] These phase boundaries in the temperature composition diagram can be found in numerous solid solutions and often feature enhanced electromechanical properties.[127-132]

To achieve substantial EC temperature changes, very large electric fields are required. Intrinsic and extrinsic properties will limit the electric field strength. In single crystals micro-cracks will occur due to the large electromechanical strain.[133] Some materials cannot withstand large electric fields, because of their limited dielectric strength or grain boundary conductance.[134-136] A high ionic or electronic conductivity will result in a large leakage current, leading to Joule heating. The Joule heating will decrease the cooling and will increase the heating effect in the material.[137, 138] Therefore, materials with large electric breakdown fields are desired.

1.3.3. Measures of Electrocaloric Materials

Using the EC material as a coolant awareness has to be given that the temperature change effect only occurs during an electric field change and therefore, after a cooling step a heating step follows. To utilize now the ECE in a cooling device a thermodynamic cycle must be installed with a heat sink and a heat load between which the heat is transferred by the EC element. A possible Carnot-like cycle[18, 46, 49] for electrocaloric refrigeration is shown in Figure 1.3.3. Starting at state A, the material undergoes a temperature change. This is due to the compensation of the decrease in entropy of the dipolar subsystem by the lattice subsystem. The total entropy of the state A and the state B are the same under adiabatic conditions. The step A to B can be also described by an isothermal process, at which the dipolar entropy decreases due to the ordering of the dipolar entities in an electric field and an isofield process, at which the temperature increases due to the increase in the lattice vibration entropy. At state B the material is brought into contact with a heat sink and thus allowed to release heat until it reaches state C. From state B to C the electric field is held constant. Step C to D and back to state A is the reversal of the previous processes. At the adiabatic depolarization the increase of dipolar entropy is compensated by the decrease of lattice entropy, hence the temperature of the material decreases. From state D to A the material absorbs heat from the load.

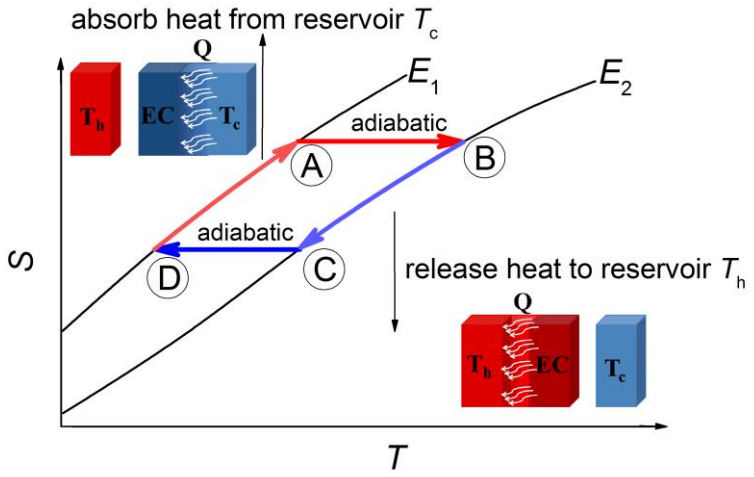

Fig. 1.3.3: Schematic presentation of the entropy and temperature change during an electrocaloric cycle: The path from A to B and C to D represent adiabatic processes and the path from B to C and D to A represent isoelectric heat exchange. E_1 and E_2 denote constant electric fields.

From the above considerations three quantities, i.e. temperature change, entropy change and absorbed heat, can be deduced that are important measures of potential candidates for EC cooling. Those properties can be transferred into each other if the specific heat capacity is known:

$$\Delta T = \frac{Q}{c_p}, \tag{1.3.17}$$

and

$$\Delta T = \Delta S \frac{T}{c_p}. \tag{1.3.18}$$

Comparison between EC materials are often done by those three quantities but they are not sufficient to find suitable EC materials. Moreover, other performance parameters must be included like the work (W_E) done to drive the ECE. This can be connected to the heat (Q_C) absorbed by the EC material towards the materials efficiency[139]:

$$\eta = \frac{Q_C}{W_E}. \tag{1.3.19}$$

Further performance characteristics, i.e. thermophysical behavior, on the material level should be included to find the most suitable EC coolant. Presently, information on thermophysical behavior of ferroelectric materials is lacking. The thermal conductivity of only some materials are reported.[140-152] Measurements of the specific heat capacity are sometimes largely deviating from the theoretical Dulong-Petit limit which was confirmed for example in barium titanate.[153, 154] For barium titanate a specific heat capacity of 750 J kg^{-1} K^{-1} was reported[155] which is 210 J kg^{-1} K^{-1} higher as expected from the Dulong-

Petit limit. If equations 1.3.17 and 1.3.18 are used to interconvert the EC properties, those large differences in the specific heat capacity will lead to large differences in those properties. Therefore, knowledge about the thermophysical behavior in ferroelectrics should be expanded and the influence of phase transition characteristics should be understood.

1.3.4. Electrical Degradation in Electrocaloric Materials

Electrical degradation in ferroelectrics is a well-known phenomenon and can be designated to fatigue and aging. The term fatigue in ferroelectrics is used for the reduction in material performance under the cyclic application of an electric field. Whereas, aging occurs under constant external parameters. Fatigue in ferroelectrics is investigated in dependence of the way the electric field is applied, i.e. unipolar, sesquipolar or bipolar.[156] With regard to EC applications, fatigue under unipolar electric fields is of interest. A differentiation must be taken in the applied electric field function between unipolar electric fields used in most literature and the one used for EC cycles. For applications, such as actuators, a sinusoidal or triangular electric field function is used. For EC cycles a step-like electric field function must be considered, with sharp increase/decrease of the electric field and holding times with constant maximum and zero electric field in between. In the following, some factors influencing the electrical degradation of ferroelectrics are highlighted.

The influence of unipolar electric field cycles on the macroscopic properties was investigated by Pan et al.[157], Verdier et al.[158, 159] and Wang et al.[160]. It was observed that an offset polarization is built. This is depicted by the shift of the polarization curve along the polarization axis. Verdier et al.[159] assigned the offset polarization to an accumulation of charge carriers at the grain boundaries. They found that a thermal annealing at 373 K leads to a reduction in the offset polarization and a complete loss was observed above 523 K. The effect of unipolar electric field cycling was found small compared to bipolar electric field cycling. Nevertheless, for EC cycling it has to be considered that the maximum electric field is held for a certain time during one cycle. Therefore, electrical degradation due to electric field triggered transport mechanisms must be considered. Charged species, i.e. electronic or ionic, might be moved towards one of the electrodes depending if they are positively or negatively charged. Defect species occur always to a certain amount. In perovskite-type titanates typical defect species are oxygen vacancies, see Figure 1.3.4. It was shown that an electric field can lead to the migration of those species in connection with enhanced conductivity.[161-164] A separation of charged species and concentration gradients of oxygen vacancies are often assumed to model the degradation behavior. Compared to the initial state the anode region is considered to be oxygen vacancy depleted and the cathode region to be enriched.[161, 165-169] The migration of oxygen vacancies is considered the origin of degradation, whereas the enhanced conductivity is a result of electronic charge carrier injection. The enhanced electrical conductivity

impedes the EC performance, hence, the long term stability of the EC effect should be investigated experimentally to verify the influence of the electric field wave form on the cyclic stability.

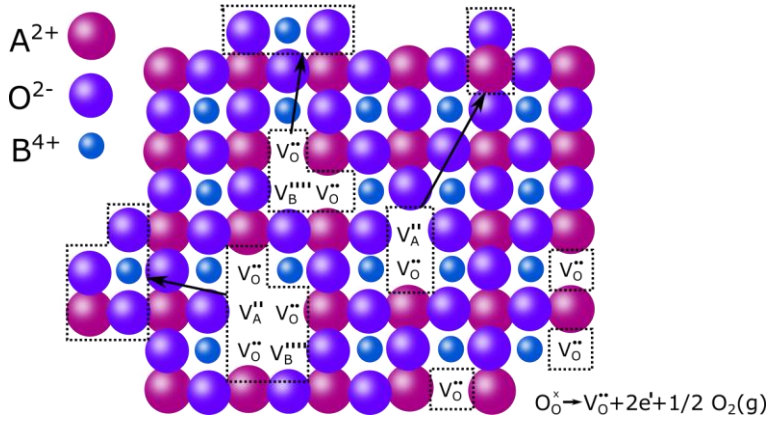

Fig. 1.3.4: Common defects occurring in barium titanate, schematically redrawn from Lee et al.[170]. Shown are partial and full Schottky defects and outgassing of oxygen.

1.3.5. The $Ba(Zr_xTi_{1-x})O_3$ System as an Interesting Electrocaloric Material

The first polycrystalline ceramic discovered exhibiting ferroelectricity was barium titanate, BT.[171, 172] It was from then on that BT was considered for piezoelectric applications like transducers.[173] Furthermore, the main phenomenological theory for ferroelectrics was developed by Devonshire on basis of considerations about BT.[98, 99] Due to the discovery of lead zirconate titanate (PZT) shortly after, BT was not of main focus for applications.[127, 174] Nevertheless, scientific interest was always strong on BT and it is seen as a prototype ferroelectric used for comparison. BT has a cubic perovskite structure at high temperatures with Ba^{2+}-ions on the A-site, Ti^{4+}-ions on the B-site and O^{2-}-ions building an oxygen octahedra.[90] From the high temperature phase three consecutive phase transitions take place: cubic ($m\bar{3}m$) $\xrightarrow{\sim 393\ K}$ tetragonal (4mm) $\xrightarrow{\sim 278\ K}$ orthorhombic (mm) $\xrightarrow{\sim 183\ K}$ rhombohedral (3m).[89] At those phase transitions the axis of the dipolar moment goes from <001> to <011> and then to <111>. The dipolar moment itself originates from the shift of Ti^{4+}-ions and O^{2-}-ions relative against the Ba^{2+}-ions.[175] With the phase transition changes in the lattice parameter, spontaneous polarization and dielectric permittivity can be observed, shown in Figure 1.3.5. At the PE to FE transition a jump in the spontaneous polarization occurs connected with the first order character of the transition. Similar jumps occur at the interferroelectric transitions. Those transitions must be of first order, as the ferroelectric phases do not share group-subgroup relationships. The dielectric softening in the vicinity of the phase transitions can be seen from the distinct maxima in the dielectric permittivity.

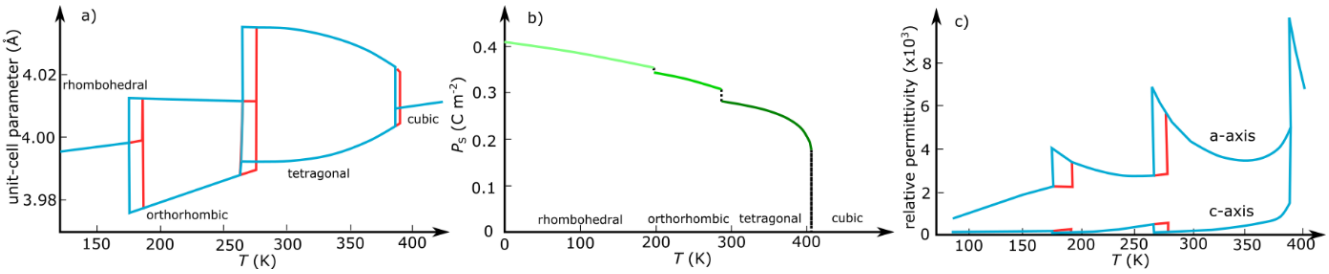

Fig. 1.3.5: Properties of barium titanate single crystals after Jona & Shirane[90]. a) Unit-cell parameter as a function of temperature. b) Spontaneous polarization as function of temperature. c) Relative permittivity as function of temperature.

For EC applications BT is of interest due to non-toxic constituents, high polarizability and the large dielectric strength. The dielectric strength of BT is 180 kV cm^{-1}[176] which is twice the one of PZT[177]. Shortly after the report on the giant ECE[178] the well-developed phenomenological description of BT was used to explain the occurrence of the giant ECE and that at the large applied electric fields on the thin film such a giant temperature change is expectable and far from giant.[179] Furthermore, the mechanical boundary conditions and the influence on the phase transition temperature were investigated by means of the phenomenological theory.[180] The influence of grain size on the ECE in BT was investigated shortly after but only three nano-grain sizes were investigated theoretically.[181] Another theoretical treatment of BT thin films including mechanical constraints was conducted in terms of a transverse Ising model resulting in a temperature change of ~11 K at an electric field change of 400 kV cm^{-1}.[182] The first direct measurements of the EC temperature change on BT were conducted on a single crystal with [001] orientation. A modified DSC (differential scanning calorimeter) was used to measure the specific heat capacity under various electric fields around the PE to FE transition[155] and the interferroelectric transition from tetragonal to orthorhombic structure[183]. The reported maximum entropy change around the PE to FE phase transition was 1.9 J kg^{-1} K^{-1} (ΔT_{EC} = 1.6 K). In a later study an entropy change of 2 J kg^{-1} K^{-1} was reported.[184] Larger entropy changes for the PE to FE transition were found for BT single crystals in other studies, where the electrocaloric effect was not investigated.[185-188] Using the entropy changes observed there, i.e. 2.15 J kg^{-1} K^{-1} - 2.36 J kg^{-1} K^{-1}, field induced temperature changes over 2 K can be expected. These differing values demonstrate that the electrocaloric temperature change in BT single crystals is dependent on the quality of the crystal and moreover the underlying defect structure. A more deep study was conducted by Novak et al.[115, 116], where the connection between the electric field induced PE to FE transition, the resultant latent heat, and the impact of the critical end point were studied experimentally and in the framework of the phenomenological Ginzburg-Landau theory. After the advantages of thin films, i.e. large electric field can be applied, and bulk structures, i.e. large cooling capacity, were determined, the research direction went towards multilayer structures in order to combine both advantages.[65] BT-based multilayer structures were investigated and substantial temperature changes of 1.8 K were found.[67, 189, 190]

From the EC point of view BT is not solely interesting due to its large temperature changes around the PE to FE phase transition but also as a base material for isovalent substitution at the A- and B-site. By substituting different ions into the BT lattice the PE to FE and interferroelectric phase transitions can be strongly influenced but the perovskite structure can be preserved.[89] Exchanging the Ti^{4+}-ion by a Zr^{4+}-ion shifts T_C to lower temperatures and the interferroelectric transitions towards higher temperatures, see Figure 1.3.6. The Zr^{4+}-ions (0.084 nm ionic radius) are larger than the Ti^{4+}-ions (0.061 nm ionic radius) and are considered to be nearly unpolarizable.[191-193] With low concentrations of Zr^{4+}-ions, $x<0.13$, the three consecutive phase transitions, cubic to tetragonal to orthorhombic to rhombohedral (decreasing temperature), are maintained. Around $x\sim0.13$ - 0.15 the lines of the transition temperatures in the phase diagram merge together and only one transition from cubic to rhombohedral occurs. For higher concentrations of Zr^{4+}-ions the macroscopic properties like dielectric response or polarization show diffusive character or relaxor-like behavior. Due to the interest in those properties for example as a capacitor or actuator material, barium zirconate titanate, $Ba(Zr_xTi_{1-x})O_3$, has been investigated for decades.[73, 77, 194-202] An early work from Hennings et al.[194] investigated the range from $x=0.00 – 0.25$ with focus on the phase transition range. From latent heat measurements they deduced that the first order character of the paraelectric to ferroelectric transition gradually decreases with increasing Zr^{4+}-ion content. This is reflected in the observed behavior of the spontaneous polarization (in the reference it is remanent polarization). The jump in polarization at T_C gradually decreases with increasing Zr^{4+}-ion content. For the compositions with diffusive phase transition the polarization slowly decreases over a broad temperature range coinciding with the broad maximum in the dielectric permittivity. In 1990 Lin and Wu[203] gave an explanation for the shape of the $Ba(Zr_xTi_{1-x})O_3$ phase diagram based on lattice distortions introduced by the Zr^{4+}-ion substitution. They assumed that the lattice strain broadening measured by XRD reflects the dynamic strain of the soft phonon mode above T_C. By comparing BT to compositions with A-site or B-site substituents of different amounts, it can be seen that a B-site substitution of a sufficient amount (in their work $Ba(Zr_{0.2}Ti_{0.8})O_3$ was measured) leads to a suppression of lattice strain induced from soft phonon modes. They concluded that the larger Zr^{4+}-ions push the neighboring oxygen ions outwardly along the <001> axis towards the center of the next octahedral, thereby hindering the displacement of Ti^{4+}-ions and retarding the soft mode vibration. Further, the push-in of an oxygen ion will displace the other oxygen of an octahedral outwardly and therefore open space for the Ti^{4+}-ion to displace along the <011> and <111> axis. This is reflected in the temperature increase of the interferroelectric transitions with increasing zirconium content. As the above mentioned works focus more on the transition from BT towards compositions with diffusive phase transitions the interest of most following studies were directed towards the onset and origin of relaxor-like behavior in $Ba(Zr_xTi_{1-x})O_3$.

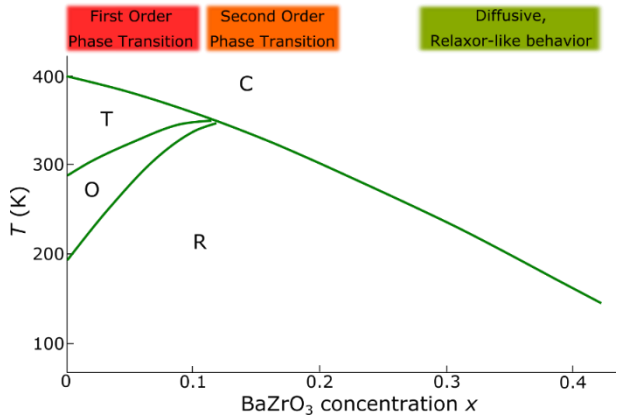

Fig. 1.3.6: Temperature – composition phase diagram of $Ba(Zr_xTi_{1-x})O_3$ after Dong et al.[204]. Composition ranges are included where first order, second order phase transitions and diffusive, relaxor-like behavior was found.

Around the millennium Ravez and different co-authors addressed the relaxor onset in a series of publications.[205-209] They observed by XRD that, like PMN, no macroscopic structural transition takes place around T_m. But unlike PMN, no long-range ferroelectric order could be induced by an external electric field.[206] A phase diagram was constructed with the onset of relaxor-like behavior at $x \sim 0.27$ and a defect cluster model was suggested to explain the relaxor properties.[209] At the same time Sciau, one of the co-authors of Ravez, published synchrotron radiation powder diffraction data of $Ba(Zr_{0.35}Ti_{0.65})O_3$ suggesting that the low temperature ground state is different from the one of PMN.[210] It was suggested that no chemically ordered regions exist in $Ba(Zr_{0.35}Ti_{0.65})O_3$ like in PMN and that the behavior is close to the ideal dipolar glass model. The difference from PMN was further corroborated by Raman investigations under high pressure.[211] It was shown that the Raman fingerprint of $Ba(Zr_{0.35}Ti_{0.65})O_3$ behaves like a relaxor with temperature but like a ferroelectric with pressure. More insight on the structural features of $Ba(Zr_{0.35}Ti_{0.65})O_3$ was given by an EXAFS study and pair distribution function analysis from neutron powder diffraction data from Laulhe et al..[193, 212] It was found that the Zr-O distance in $Ba(Zr_xTi_{1-x})O_3$ relaxor compositions is the same like in $BaZrO_3$ suggesting that the ZrO_6 octahedra is stiff against chemical pressure. To accommodate the chemical pressure from surrounding $BaTiO_3$, the ZrO_6 octahedra tilt (assumed angle of 11°). At the same time a tensile stress for the $BaTiO_3$ next to $BaZrO_3$ was assumed to accommodate the large differences in the cell volume. From the pair distribution analysis it was deduced that the Ti displacement is the same like in BT. So both end members BT and BZ maintain their off-centering, or in the case of BZ no off-centering, in $Ba(Zr_xTi_{1-x})O_3$. From their findings the authors concluded that the difference in the dielectric properties between the $Ba(Zr_xTi_{1-x})O_3$ compositions is not a result of the B-site off-centering but a different correlation between the cation displacements.

Besides those structural investigations, attempts were made to explain the relaxor origin and the difference to the archetypical PMN in terms of the low temperature nonergodic state. Bokov et al.[213] performed a dielectric analysis of $Ba(Zr_{0.325}Ti_{0.675})O_3$ and found deviation from the Vogel-Fulcher freezing. They assumed two sets of PNRs existing in the low temperature range, i.e. static (large) PNRs and dynamic (small) PNRs. The nonergodicity is associated with the static PNRs which cannot be reoriented by thermal activation due to the large size. Similar, deviation from the Vogel-Fulcher freezing was reported by Ke et al.[214] and a coexistence between static (large) and dynamic (small) PNRs was also suggested by Shvartsman et al.[215]. The origin of the PNRs is still under debate driven by different models for relaxor behavior. Kleemann follows the idea of random fields.[216, 217] As this might be understandable for PMN where the B-site ions have different charge states, it might be questionable for $Ba(Zr_xTi_{1-x})O_3$ where Zr^{4+}-ions and Ti^{4+}-ions have the same charge. Kleemann argues that the internal strains due to the unit cell mismatch between BT and BZ unit cells, give rise to small random fields that play the important role in the relaxor-like behavior of $Ba(Zr_xTi_{1-x})O_3$.[216] In contrast Akbarzadeh et al. found by first-principle calculations that random electric fields and random strains do not significantly contribute to the formation of PNRs.[218, 219] Sherrington offered another view on $Ba(Zr_xTi_{1-x})O_3$ as a soft pseudospin glass.[220] From broadband dielectric measurements it was revealed that PNRs are related to Ti^{4+}-ions hopping between equivalent states and that the phase transition is rather of the order-disorder type than of the displacive type.[221, 222] Seeing $Ba(Zr_xTi_{1-x})O_3$ as a dipolar glass rather than a relaxor was supported by Pirc et al.[223] and Filipic et al.[224] by their observation that no macroscopic domains can be formed by the application of an electric field.

Beside the question about the crossover from ferroelectric to diffusive and relaxor-like behavior in $Ba(Zr_xTi_{1-x})O_3$ interest arose about the electrocaloric properties, as $Ba(Zr_xTi_{1-x})O_3$ is a lead-free system.

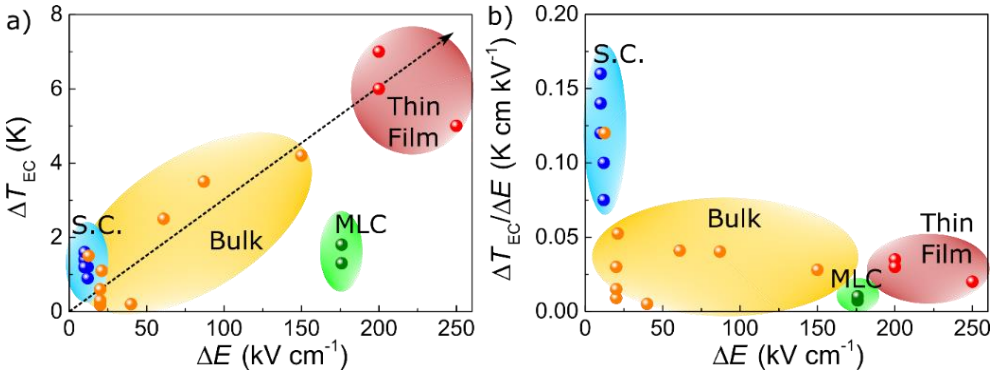

Fig. 1.3.7: a) Electrocaloric temperature change, and b) electrocaloric responsivity as function of electric field change of barium zirconate titanate. Data is shown for direct measurements on single crystals (S.C.), bulk materials, thin films and multilayer capacitors (MLC). For references of the taken data points see text.

The main focus of EC investigations was set on BT as a typical ferroelectric material that has been investigated for decades and on $Ba(Zr_{0.20}Ti_{0.80})O_3$ which exhibits the diffusive phase transition around room temperature. The tuning of ferroelectric to paraelectric phase transition towards lower temperatures, than the one observed in BT, made $Ba(Zr_xTi_{1-x})O_3$ an interesting system. In Figure 1.3.7 a) the electrocaloric temperature change and b) electrocaloric responsivity of BT and $Ba(Zr_{0.20}Ti_{0.80})O_3$ are shown. Data is taken from references with direct measurements of the ECE.[116, 155, 184, 190, 192, 225-232] Note that the measurement points shown are at different temperatures. Nevertheless, some common trends can be observed. From Figure 1.3.7. a) can be seen that the electrocaloric temperature change increases with increasing electric field change. Single crystals, bulk samples and thin films lie around a straight line, demonstrating the importance of large electric fields. The multilayer capacitors fall off this line and show lower values than expected for large electric field changes. Those might be due to non-optimum temperatures where the measurement was conducted and difficulties in the exact determination of the ECE itself. Multilayer capacitors consist of multiple layers of EC active material, but also layers of electrodes, inactive EC material (material at the edges where the electric field strength is lower or vanished) and two outer electrodes. Those extra thermal masses that do not contribute to the temperature change make it difficult to determine exactly the temperature change of the active ECE material itself. In Figure 1.3.7. b) the EC responsivity is shown. It can be seen that bulk samples, multilayer capacitors and thin films exhibit similar EC responsivity and that the influence of the electric field change on the EC responsivity is low. In comparison to the other sample structures, single crystals exhibit rather large EC responsivities. This results from the large contribution of the electric field induced phase transition from paraelectric to ferroelectric phase above T_C. In a narrow temperature range the contribution from the phase transition is large and the low electric fields needed to drive BT single crystals into the ferroelectric phase leads to the large EC responsivity.

2. Experimental Part

2.1. Processing

Ceramics with the nominal composition $Ba(Zr_xTi_{1-x})O_3$ were produced via a solid state route in the molar fraction range x=0-0.35. Raw materials of $BaCO_3$ (>99 %), TiO_2 (>99 %, anatase) and ZrO_2 (>99 %) (all Alfa Aesar GmbH, Germany) were weighed with respect to their stoichiometric formula and placed in a nylon container. The total batch consisted of 40 g weighed powder. For the mixing step zirconia balls and ethanol was added. The mixing of the start powders was performed in a planetary ball mill (Fritsch Pulverisette 5, Germany) for 5 h and a rotation frequency of 250 rounds per minute. The suspension was filled into a glass beaker and dried in an oven at 363 K for 24 h. The powder was then compacted with a hand press into cylindrical pellets and calcined in a zirconia crucible at 1473 K for 2 h with a heating/cooling rate of 3 K/min. The calcined pellets were pulverized and filled in the nylon container with zirconia balls and ethanol. The powder was then milled in the planetary ball mill for 15 h at a rotation frequency of 250 rounds per minute. The suspension was then filled in a glass beaker and dried in an oven at 363 K for 24 h. The dried powder was pestled and compacted with a hand press into disc-shaped green bodies. The green bodies were then compacted further in a cold isostatic press (KIP 100E, Paul-Otto Weber GmbH, Germany) at 300 MPa for 90 s. The pressed green bodies were sintered inside a zirconia crucible at 1623 K for 2 h and a heating/cooling rate of 3 K/min. The sintered samples were ground from both sides by a semiautomatic grinding machine to an end thickness between 200 μm and 500 μm. After the grinding step, samples were heated to 673 K for 2 h and a heating rate of 2 K/min.

For microstructural investigations with the optical microscope, the samples were polished in several steps down to a ¼ μm diamond paste finish. The polished samples were then thermally etched in a muffle furnace at 1473 K for 30 min and a heating/cooling rate of 10 K/min.

For electrical testing a thin layer of silver was sputtered on both surfaces by a sputter coater (Emitech K950x Turbo Evaporator, Quorum Technologies, UK). A mask was partly used (electrocaloric measurements) to cover the edge in order to prevent electrical sparks at the electrical testing with high voltage. The sample was inserted free or with the mask into the chamber of the sputter coater and the chamber was evacuated. Argon gas was inserted into the chamber in a flow mode at an argon pressure of 2 $x10^{-2}$ mbar. A current of 40 mA was applied to the silver target for 8 min per surface. To mount a sample into the home-built measurement chamber copper wires were connected to the electrodes. Thin copper wires with a weight of ~0.0010 g were glued with a small amount ~0.0015 g of conducting silver varnish on both electrodes.

2.2. Microstructure and Crystallinity

The density of the samples was measured by the Archimedes method. For the measurement a hydrostatic scale (BA110S Basic, Sartorius AG, Germany) was used. First the sample was measured in air (m_{air}). The sample was then given into a flask with distilled water and put into a vacuum bell jar for 30 min. Afterwards the sample was measured in water (m_{water}). During the weighing the temperature of the water in the scale was read from a thermometer. The density can be calculated by the following formula:

$$\rho = \frac{m_{air} \cdot (\rho_{water}(T) - \rho_{air})}{K \cdot (m_{air} - m_{water})} + \rho_{air}. \quad (2.2.1)$$

Here ρ, $\rho_{water}(T)$, ρ_{air} and K are the density, the density of water, the density of air and a correction factor. The density is in general temperature dependent but here only the exact density of water was considered depending on the temperature determined from the thermometer. For the density of air 0.0012 g cm^{-3} were assumed (1 bar, 293 K). The correction factor accounts for the fact that the wires of the scale are submerged deeper into the water when the sample is weighed inside the water and is given by the manufacturer as 0.99983.

Microstructural images were taken at room temperature with an optical microscope (LEITZ DMRME, Leica Microsystems GmbH, Germany). For the determination of mean grain size images of 5 samples of the same composition were taken and analyzed with the linear intercept method. For the grain size calculation with the linear intercept method a numerical factor of 1.56 for isometric grain shape was used.

The XRD experiments were carried out at room temperature on sintered samples which were crushed prior to the measurement. The samples were analyzed in a Bragg-Brentano geometry (AXS D8, Bruker Corporation, Germany) with copper K_α radiation (λ=1.5406 Å). The angular range of the measurement was 20° to 80°. The experiments were performed by Mr. Jaud (FG Strukturforschung, TU Darmstadt). The lattice parameter can be determined by the Bragg equation,

$$n \cdot \lambda = 2 \cdot d \cdot \sin(\theta), \quad (2.2.2)$$

where n, d, θ are an integer number, the lattice plane distance and the angle between the incident beam and the sample. The lattice plane distance is connected with the lattice parameter by the Miller indices.

Cubic: $$\frac{1}{d^2} = \frac{h^2+k^2+l^2}{a^2}. \quad (2.2.3)$$

Tetragonal: $$\frac{1}{d^2} = \frac{h^2+k^2}{a^2} + \frac{l^2}{c^2}. \quad (2.2.4)$$

Orthorhombic: $$\frac{1}{d^2} = \frac{h^2}{a^2} + \frac{k^2}{b^2} + \frac{l^2}{c^2}. \quad (2.2.5)$$

Rhombohedral: $$\frac{1}{d^2} = \frac{4}{3}\left(\frac{h^2+hk+k^2}{a^2}\right) + \frac{l^2}{c^2}. \quad (2.2.6)$$

2.3. Dielectric Permittivity Analysis

The dielectric permittivity (ε) or dielectric susceptibility (χ) are parameters describing the response of a dielectric material to an external applied electric field and give a measure of the charge that can be stored on the electrodes of the capacitor arrangement. Contributions to the dielectric permittivity origin from intrinsic factors, i.e. electronic and ionic polarization, and extrinsic factors, i.e. orientation polarization, space charge polarization or domain wall polarization. The dielectric permittivity of a material can be determined by comparison with a capacitor of the same dimensions but with vacuum between the two electrodes. By applying an electric field to such a capacitor, the electrodes will get charged and exhibit the capacitance C_0. In case of the gap between the electrodes filled by a dielectric material, the capacitance will increase to C, because the external electric field leads to induced polarization that partly cancels the charge on the electrodes. The dielectric permittivity is in general a complex quantity and can be divided in a real part and an imaginary part.

$$\varepsilon = \varepsilon' + i\varepsilon''. \quad (2.3.1)$$

The real part of the complex dielectric permittivity is determined by the ratio between the capacitor filled with the dielectric material and a capacitor with vacuum.

$$\varepsilon' = \frac{C}{C_0}. \quad (2.3.2)$$

Here ε' is the real part of the dielectric permittivity. In case of a parallel plate capacitor the capacitance C_0 can be expressed as:

$$C_0 = \varepsilon_0 \frac{A}{d}. \quad (2.3.3)$$

Here ε_0, A, d are the permittivity of vacuum (8.85 x10^{-12} A s V^{-1} m^{-1}), the area of the electrode and the distance between the electrodes.

The imaginary part of the complex dielectric permittivity describes the losses that occur if an electric field (mostly an ac electric field) is applied to the dielectric material. Those losses originate from the leakage current in the material due to the fact that real materials exhibit a finitely large resistivity. Another origin can be the consumption of energy by the material if an ac electric field is applied that

expresses itself in heat generation. Those losses result in a phase shift that is different from an ideal capacitor (90°) and are generally given as a loss tangent ($\tan\delta$).

$$\tan\delta = \frac{\varepsilon''}{\varepsilon'}. \tag{2.3.4}$$

The dielectric behavior of the samples was measured in a parallel plate capacitor arrangement with two electrodes on the surfaces of the samples by an LCR meter (Precision LCR Meter HP4192A, Hewlett Packard, USA). The frequency range of the LCR meter was 20 Hz to 1 MHz. Several frequencies were measured and are indicated in the corresponding figure. For all measurements a heating/cooling rate of 1 K min^{-1} was used and an ac voltage of 1 V if not otherwise indicated. The given measurement accuracy of the equipment is ±0.05 % (manufacturer manual).

2.4. Impedance Spectroscopy

The impedance (Z) is a complex quantity that gives a measure on the opposition an electronic device (here a parallel plate capacitor) can give to an ac current at a specific frequency. The impedance is given by the real part, i.e. resistance (R), and the imaginary part, i.e. reactance (X):

$$Z = R + jX. \tag{2.4.1}$$

A similar representation can be chosen for the admittance (Y) which is the inverse of the impedance. Then the real part is defined by the conductance (G) and the imaginary part is the susceptance (B):

$$Y = G + jB. \tag{2.4.2}$$

Impedance and admittance make it possible to characterize the reaction of a capacitor to an ac field. As a real capacitor has a finite resistivity, it can be described by an equivalent circus with a susceptance and a conductance in parallel and therefore is equal to the admittance.

The impedance was measured by an impedance analyzer (Alpha-A impedance analyzer, Novocontrol Technologies, Germany) connected by 4-point probe to the sample. The measured frequency range was 10^{-2} Hz to 10^{7} Hz. An excitation ac voltage of 1 V was used. The obtained impedance data was analyzed with the software RelaxIS (rhd instruments, Germany).

2.5. Polarization Analysis

In a ferroelectric material an applied external field can induce electric dipole moments and orientate permanent electric dipole moments. By applying external electric field amplitudes with opposite direction a so-called hysteresis loop is observed for ferroelectric materials, like described in section 1.2.7.

The hysteresis loop can be measured by a Sawyer-Tower bridge.[233] A schematic of the home-built setup can be seen in Figure 2.5.1. A dc voltage signal is generated by a function generator (33220A, Agilent, USA). The signal is then amplified by a high voltage generator (Trek 20/20C, TRek Inc., USA). The high voltage is applied to the sample which is in series with a reference capacitor (16.77 μF). The displacement current at both capacitors is the same (they are in series) and therefore the same charge Q is accumulated at the capacitors. The following relations can be used to determine the polarization of the sample by measuring the voltage at the reference capacitor:

$$Q = C_{\text{sample}} \cdot U_{\text{sample}} = C_{\text{reference}} \cdot U_{\text{reference}} , \tag{2.5.1}$$

$$P = \frac{C_{\text{reference}} \cdot U_{\text{reference}}}{A_{\text{sample}}}. \tag{2.5.2}$$

The voltage at the reference capacitor was measured by a measuring board from National Instruments which was connected to a computer and readout by a LabView program. The LabView program was written by Florian Schader (FG Nichtmetallisch Anorganische Werkstoffe, TU Darmstadt).

During the polarization measurement a dc electric field was ramped with 8 x10^6 V m^{-1} s^{-1} to the maximum electric field (positive electric field axis in the figures) and then with the same rate to the negative electric field maximum (negative electric field axis in the figures) and with the same rate back to zero electric field. Prior to the measurement, the measurement temperature was stabilized for at least 10 minutes.

The sample is connected in series with the reference capacitor and therefore a part of the applied voltage will drop at the reference capacitor. The reference capacitor is chosen to have a much larger capacitance than the sample to keep the voltage drop small. For the sample a capacitance in the nF-range can be assumed which will not be larger than 50 nF even close to phase transitions or with applied electric field. This leads to a maximum error in the applied electric field below <0.3 %.

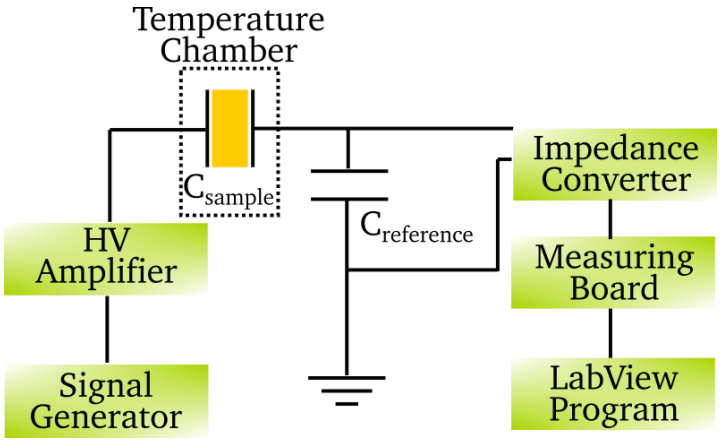

Fig. 2.5.1: Setup for polarization measurements: Schematic representation of the measurement setup for polarization measurements at ramping dc electric field for various temperatures above and below room temperature.

2.6. Calorimetry: AC Calorimetry and Differential Scanning Calorimetry (DSC)

Calorimetric techniques can be used to determine the thermal behavior of ferroelectrics and measure the temperature dependence of the specific heat capacity. Especially the nature of the phase transition, i.e. first order or second order, and the occurrence of critical fluctuations can be determined. For the characterization of first order phase transitions the amount of latent heat $L \equiv \Delta H$ and the presence of possible pretransitional heat capacity effects are of interest. For a second order phase transition there are no discontinuities in the enthalpy H but the heat capacity will exhibit either a discontinuous jump or a divergence. Several calorimetric techniques were developed over the years each one with its strength and weaknesses. Here, two techniques will be introduced, i.e. differential scanning calorimetry (DSC) and ac calorimetry. Information in this section is taken from a book chapter from Garland.[234]

DSC is the most common calorimetric technique used nowadays due to the availability of commercial instruments. The method has advantages in detecting very small enthalpy changes (~0.01 J g^{-1}), small sample sizes (~10 mg) and rapid operating procedures. However, difficulties occur to make detailed quantitative measurements near phase transitions. This can be understood considering the measurement principle. A constant heating rate $dH_{reference}/dt$ is applied to a reference sample (sapphire) resulting in a linear temperature increase of the reference sample. The instrument forces the sample to follow the temperature ramp of the reference sample. To do so the power input dH_{sample}/dt has to be varied. The differential power is the measured quantity. Problems to distinguish between first order and second order phase transitions in the DSC signal arise due to the fact that the latent heat cannot be delivered to the sample instantaneously. This will broaden the signal for a first order phase transition and make it similar to a second order phase transition with the same integrated enthalpy change δH. Even more difficult it will get to distinguish those transitions from a weak first order phase transition with pretransitional heat capacity changes. Ferroelectrics, also the archetypical BT with its first order paraelectric to ferroelectric phase transition, exhibit such weak first order phase transitions.

Another source of problem may be the fast scan rate DSC instruments use. Typical scan rates for DSC instruments are 5-10 K min^{-1} which can be orders of magnitude larger than the rate required to stay in thermal equilibrium.

The absolute accuracy of latent heat is around ±20 % and the accuracy of integrated enthalpy change might be ±50 %.

The measurements were conducted by Claudia Fasel (FG Disperse Feststoffe, TU Darmstadt) in a DSC from Netzsch (DSC 200 F3 Maia, Netzsch-Gerätebau GmbH, Germany). Samples with a weight between

20 – 40 mg were measured in an aluminum pan. As a reference material sapphire was used. The heating rate was 10 K min^{-1} and a nitrogen flow with 250 ml min^{-1} was defined.

Another calorimetric technique is ac calorimetry. It was invented in the 1960s by Kraftmakher[235] and Sullivan and Seidel[236]. For this technique an oscillating input power is applied on one side of the sample and the oscillating temperature response at the opposite surface is measured. From this the heat capacity can be determined directly and not the enthalpy like in the DSC. The advantage of this technique is that slow scanning rates can be used and a good resolution in C_p(T). For thermal analysis some assumptions must be made. Here, a zero-dimensional model of thermal analysis is used, which can be assumed if the internal time constant of the sample (τ_{int}) is small and temperature gradients can be neglected. This depends on the thermal conductivity of the sample and can be adjusted by suitable choice of the sample geometry. If internal temperature gradients cannot be neglected, a suitable model for thermal analysis must be chosen (like one-dimensional model). A second assumption is made by considering that the thermal link to the bath can be represented by a single thermal resistance R. The thermal link is the gas and wires that connect the sample to the bath. If heat is put into the sample from the input power, it follows from the conservation of energy:

$$P = C_p \frac{dT}{dt} + \frac{dL}{dt} + \frac{T - T_{bath}}{R}. \tag{2.6.1}$$

Here $dL = \bar{L} dm$ with $\bar{L}$ the latent heat per gram and dm the mass that is converted from one coexisting phase to another. The bath temperature is T_{bath} and the sample temperature T. The input power is described by:

$$P = P_0 + P_0 \cos(\omega t). \tag{2.6.2}$$

The frequency must be chosen to avoid temperature gradients in the sample. A suitable frequency fulfills the condition $\omega \tau_{int} \ll 1$.* Equation 2.6.1 can be integrated to get the time variation of the sample temperature after a steady state is reached. It is assumed that the thermal resistance and heat capacity are constant over a small temperature interval. Furthermore, the latent heat term in equation 2.6.1 is ignored. This can be done in the absence of two phase coexistence.

$$T(t) = T_{bath} + RP_0 + \Delta T_{ac} \sin(\omega t + \varphi). \tag{2.6.3}$$

From this can be seen that the sample temperature has a dc and an ac component.

* The internal time constant can be calculated by $\tau_{int} = C_p / K$. The thermal conductance is K=t/A·κ. From the usually used geometries an internal time constant in the range 0.5 x10^{-3} - 1.4 x10^{-3} s follows.

$$T(t) = T_{dc} + T_{ac}(t). \tag{2.6.4}$$

The ac component can be re-expressed as:

$$T_{ac}(t) = \Delta T_{ac} \cos(\omega t + \varphi - \frac{\pi}{2}), \tag{2.6.5}$$

where φ represents a phase shift between the input power oscillation and the temperature oscillation. The observable quantities ΔT_{ac} and φ are given by:

$$\Delta T_{ac} = \frac{P_0}{\omega C_p}\left(1 + \frac{1}{\omega^2 R^2 C_p^2}\right)^{-1/2}, \text{ and} \tag{2.6.6}$$

$$\tan\varphi = \frac{1}{\omega\tau_{ext}} = \frac{1}{\omega R C_p}, \tag{2.6.7}$$

where $\tau_{ext} = RC_p$ is the external time constant for heat flow from the system to the bath. Equation 2.6.7 can be inserted in equation 2.6.6 and it follows:

$$\Delta T_{ac} = \frac{P_0}{\omega C_p}(1 + \tan^2\varphi)^{-1/2}, \tag{2.6.8}$$

$$\Delta T_{ac} = \frac{P_0}{\omega C_p} \cdot \sqrt{\frac{1}{1+\tan^2\varphi}}, \tag{2.6.9}$$

$$\Delta T_{ac} = \frac{P_0}{\omega C_p} \cdot cos\varphi. \tag{2.6.10}$$

The heat capacity is then given by:

$$C_p = \frac{P_0}{\omega \Delta T_{ac}} \cdot \cos\varphi. \tag{2.6.11}$$

The design for ac calorimetry measurements used is shown in Figure 2.6.1 a) and a schematic diagram is shown in 2.6.1 b). The sample was cut in dimensions of 6 mm length, 3 mm broadness and 0.5 mm thickness. On one side of the sample a strain gauge (KFH-6-120-C1-11L1M2R, Omega Engineering GmbH, Germany) with a resistance of 120 Ohm was attached, used as the heater element. On the opposite surface a small bead thermistor (GAGR150KM3976J15, TE connectivity, Switzerland) was glued to measure the temperature oscillations. The whole arrangement was soldered to contact points inside the calorimeter. A platinum thermistor (PRT) is constantly inserted in the measurement chamber to track the temperature of the bath. The measurement chamber consisted of a big copper block in order to have a large thermal mass that prevents temperature fluctuations inside the chamber. The copper block was surrounded by a flexible heater which was controlled by a temperature controller. Another stainless steel cap was used to shield the measurement chamber. The whole calorimeter can be inserted

into liquid nitrogen in order to cool below room temperature and to stabilize the temperature. The calorimeter was designed by Nikola Novak (Nichtmetallisch Anorganische Werkstoffe, TU Darmstadt).

The whole measurement procedure was controlled by a LabView program written by Patrick Breckner (FG Nichtmetallisch Anorganische Werkstoffe, TU Darmstadt). The measurement was conducted under a linear heating rate of 2 K h^{-1} controlled by a temperature controller (Eurotherm 3216, Schneider Electric, Germany). Therefore, the bath temperature was measured before and after each measurement cycle. First the PRT was read out by a digital multimeter (2001 Multimeter, Keithley, USA). Afterwards two cycles of a sinusoidal output voltage were given out by the measuring board. The angular frequency of that voltage was 0.0767 Hz and the amplitude was 5 V. The total time for the two cycles was around ~163.84 s. A resistance of 2114 Ω was connected in series with the heater. This allowed for a stable voltage supply to the heater. The power amplitude produced by the heater was 0.3 mW. During the power oscillations the temperature oscillations were recorded by measuring the resistance of the small bead thermistor with a digital multimeter (34401A Multimeter, Hewlett Packard, USA). After the two cycles the bath temperature was determined again. This procedure was followed continuously and resulted in measurement points every ~0.092 K.

By a fit of the measured T_{ac}(t) the values of φ and ΔT_{ac} can be obtained and the heat capacity can be determined. This was done in an automated procedure with a Matlab code written by Nikola Novak and Patrick Breckner (FG Nichtmetallisch Anorganische Werkstoffe, TU Darmstadt).

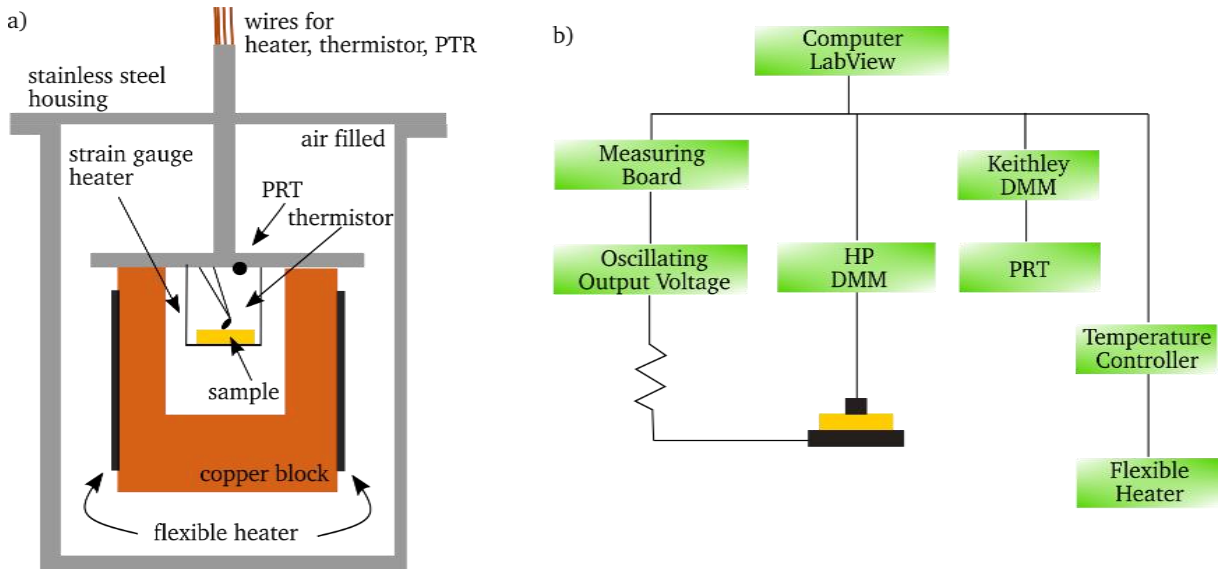

Fig. 2.6.1: Setup for ac calorimetry measurements. a) Diagram showing the components of the home built calorimeter. b) Schematic showing the measurement components and instruments used.

2.7. Thermal Diffusivity/ Conductivity Analysis

The thermal diffusion or thermal conduction of an electrocaloric material is of interest as it is important for the heat transfer from the electrocaloric material to the cold and hot reservoirs in the electrocaloric cycle. The thermal conductivity (κ) describes the property of a material to conduct thermal energy, i.e. heat, along a temperature gradient. This can be described by Fourier's law of heat conduction:

$$q = -\kappa \cdot \nabla T, \tag{2.7.1}$$

where q and ∇T are the local heat flux density and temperature gradient. In the one-dimensional form this becomes:

$$q_x = -\kappa \cdot \frac{dT}{dx}. \tag{2.7.2}$$

In general the thermal conductivity has a phonon contribution and an electronic contribution. The electronic contribution can be neglected in ferroelectric materials due to the large electric resistivity.[†] The thermal diffusivity (α) describes the heat transfer rate of a material from a point of higher temperature to a point of lower temperature. It is given by the ratio of thermal conductivity to volumetric heat capacity:

$$\alpha = \frac{\kappa}{\rho \cdot c_p}. \tag{2.7.3}$$

The thermal diffusivity plays a role in the heat equation, which can be derived from Fourier's law and the conservation of energy:

$$\frac{\partial T}{\partial t} = \alpha \cdot \nabla^2 T. \tag{2.7.4}$$

It can be seen that the thermal diffusivity is a measure of the thermal inertia of a material. In a material with low thermal diffusivity, like ferroelectrics, heat moves slowly through the material, because the heat is conducted slowly relative to the volumetric heat capacity (stored heat).

Here, two analysis techniques will be described, a transient method and a quasi-steady–state method. Transient methods, like the LASER flash analysis (LFA) described here, have the advantage of fast measurement times and reduced heat losses due to radiation. Therefore, this technique is favorable at

[†] The electronic contribution to the thermal conductivity can be estimated by the Wiedemann-Franz law: $\kappa_{electronic} = L \cdot T \cdot \sigma$, where L is the Lorenz number, i.e. ~2.5 x10^{-8} W Ω K^{-2}. The electric conductivity in ferroelectrics is low (insulators start ~10^{-6} S m^{-1}) and hence the electronic contribution to the thermal conductivity $\kappa_{electronic}$~7.5 x10^{-12} is low. For metals with large electric conductivity, i.e. >12 orders of magnitude larger, the electronic contribution to the thermal conductivity becomes substantial.

high temperatures. The LFA technique was introduced by Parker et al. in 1961.[237] The given instrumental setup used a Xenon flash lamp instead of a LASER. Such a flash lamp can be still found in commercial instruments, but due to the accepted term LFA this abbreviation will be used throughout the manuscript even if a flash lamp was used. The schematic arrangement of an LFA can be seen in Figure 2.7.1 a). A light source, i.e. a LASER or a Xenon lamp, gives a short pulse (in the ms range) to the surface of a flat sample, see Figure 2.7.1 b). It is assumed that the energy of the light pulse is absorbed by the sample solely on the surface layer. For the measurement graphite spray can be used in order to blacken the surface and reach a better absorption of the energy. For a suitable sample geometry a one-dimensional heat flow towards the rear surface can be assumed. The temperature is measured at the rear surface, see Figure 2.7.1 c).

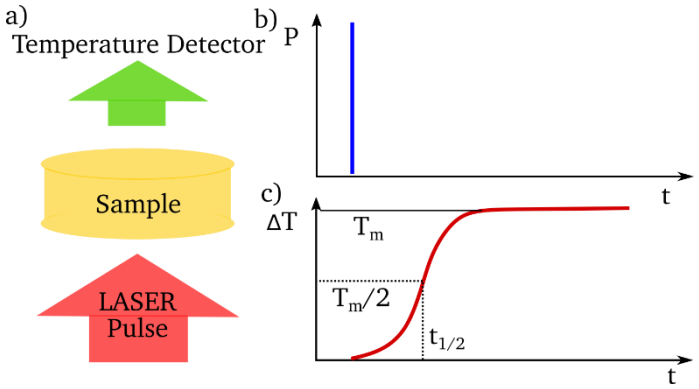

Fig. 2.7.1: Schematic of the LASER flash analysis technique to measure thermal diffusivity by a transient heat conduction. a) Measurement principle: A short LASER pulse heats up the surface of the sample and the rear surface temperture change is tracked. b) Profile of the power input with time. c) Profile of the temperature change at the rear surface.

To derive the thermal diffusivity of the material from the measured temperature profile, the one-dimensional heat transfer problem with its boundary conditions must be considered. The temperature in the sample at $t=0$ is $T(x,0)$ over the whole thickness d. At a later time the temperature distribution is given according to Carslaw and Jaeger[238]:

$$T(x,t) = \frac{1}{d}\int_0^d T(x,0)dx + \frac{2}{d}\sum_{n=1}^{\infty} \exp\left(\frac{-n^2\pi^2\alpha t}{d^2}\right) \cdot cos\frac{n\pi x}{d}\int_0^d T(x,0)cos\frac{n\pi x}{d}dx. \qquad (2.7.5)$$

The boundary conditions can be stated if assumed that the heat input Q is absorbed in a small depth L. The temperature distribution is therefore:

$$T(x,0) = \frac{Q}{\rho c_p L} \qquad 0<x<L \qquad (2.7.6)$$

$$T(x,0) = 0 \qquad L<x<d \qquad (2.7.7)$$

Using these initial conditions and equation 2.7.5 the temperature at the rear surface can be expressed:

$$T(d,t) = \frac{Q}{\rho c_p d}\left[1 + 2\sum_{n=1}^{\infty}(-1)^n \exp\left(\frac{-n^2\pi^2}{d^2}\alpha t\right)\right]. \quad (2.7.8)$$

By dimensionless analysis the thermal diffusivity can be deduced from the profile of the rear surface temperature change. Therefore, two dimensionless parameters must be introduced:

$$V(d,t) = \frac{T(d,t)}{T_m}, \quad (2.7.9)$$

$$\omega = \frac{\pi^2 \alpha t}{d^2}, \quad (2.7.10)$$

where T_m is the maximum temperature at the rear surface. Combining Equation 2.7.9 and 2.7.10 with Equation 2.7.8 yields:

$$V = 1 + 2\sum_{n=1}^{\infty}(-1)^n \exp(-n^2\omega). \quad (2.7.11)$$

If V=0.5, this means half the maximum temperature rise, $\omega = 1.38$ and the thermal diffusivity is given by:

$$\alpha = \frac{1.38 \cdot d^2}{\pi^2 t_{1/2}}, \quad (2.7.12)$$

where $t_{1/2}$ is the time to reach half the maximum temperature change. This analysis gives the advantage that it is not necessary to know the absolute temperature during the experiment, only the qualitative temperature rise, and the heat input in the beginning of the experiment does not need to be known either. The thermal conductivity can be calculated from equation 2.7.3. It has to be considered that the temperature rise in the absorbing layer of the sample can be quite large and that around phase transitions this can lead to a partial phase transformation of the sample.[‡]

The measurements of thermal diffusivity were conducted on two LFA instruments. One located at the chemistry department of TU Darmstadt (LFA 1000, Linseis, Germany) and the other one located at the material science complex of University of Connecticut (LFA 447, Netzsch, Germany). The measurements at TU Darmstadt were conducted together with Andreas Reitz (FG Anorganische Festkörperchemie, TU Darmstadt). The given accuracy for the evaluated thermal diffusivity is given as ±2 %. The sample

[‡] The temperature rise of the front surface can be calculated by $T(x<L,0)=Q/\rho c_p L$. The energy input per area can be estimated from the pulse energy of the flash lamp, i.e. ~5 J per pulse, and the area of the total measurement chamber, i.e. ~0.01 m². These values are for the LFA 447 from Netzsch, one of the LFA instruments used for thermal diffusivity measurements. The density and specific heat capacity of BT can be taken here for an estimation. The thickness L of the absorbing layer should be much smaller than the thickness of the sample and is taken here 100 times smaller than a typical sample thickness of 1.5 mm. This leads to an estimated temperature rise of the front surface of 12 K. This should be considered at measurements in the vicinity of phase transitions. Nevertheless, the temperature rise might be smaller (<3.5 K) if the thickness of the heat absorbing layer is 25 times smaller than the sample thickness.

geometry for the LFA 1000 was round pellets with a diameter of 10 mm and a thickness ~1.1 mm. For the LFA 447 squared samples with a length and broadness of 6 mm and a thickness ~1.1 mm were used. The sample surfaces were coated with a graphite spray. At every temperature 3 measurements were conducted. The measured raw data were analyzed by the respective company software to determine $t_{1/2}$.

The other technique used here is a quasi-steady-state method. In a steady-state measurement of thermal conductivity the sample is stabilized at a certain temperature and in contact with a heat source and a heat sink, see Figure 2.7.2 a). At the heat source a known constant amount of heat is supplied to the one end of the sample. The heat will travel through the sample and leave at the heat sink. After an indefinite long time a steady temperature gradient will develop in the sample. The temperature difference between the heat source and heat sink (or any two points along this axis) can be measured and the thermal conductance can be calculated according to:

$$\dot{Q} = K \cdot \Delta T. \tag{2.7.13}$$

The power input (amount of heat supplied per time) needs to be known to determine the thermal conductance. The thermal conductivity can be calculated then from the measured thermal conductance by knowing the sample geometry:

$$K = \frac{\kappa \cdot A}{\Delta x}. \tag{2.7.14}$$

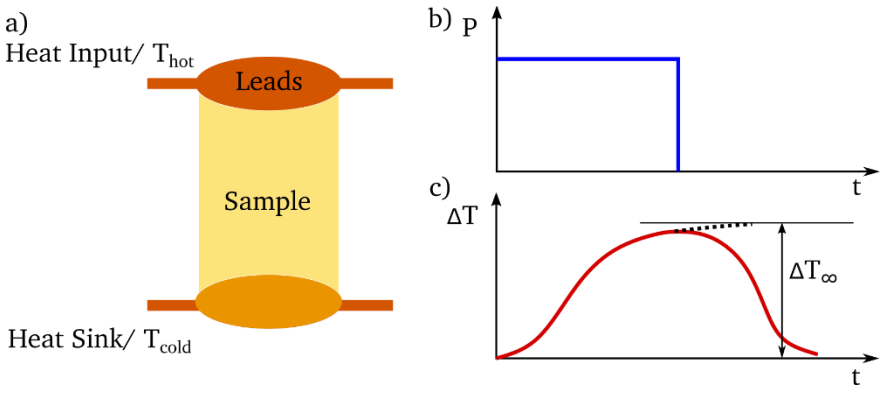

Fig. 2.7.2: Schematic of the quasi-steady-state measurement method to measure thermal conductivity. a) Measurement principle: A long pulse heats up the sample at one end and the temperature difference between both ends of the sample is recorded. b) Profile of the power input with time. c) Profile of the change of temperature difference between the two ends of the sample. The ΔT_∞ indicates the extrapolated temperature difference in the steady-state case.

The disadvantage of such a measurement is that good thermal stability is required and the long measurement times till a steady-state is reached. Nevertheless, the same principle can be used with much shorter measurement times and in a scanning mode with linear temperature increase of the bath. An appropriate fitting is necessary to subtract the linear increase of the bath and to extrapolate the steady-

state temperature difference from the measurement. For these measurements a heat pulse of several minutes, see Figure 2.7.2 b), is supplied from the heat source. A typical curve for the development of a temperature difference during the applied heat pulse is given in Figure 2.7.2 c). The temperature profile after the heat pulse is turned off must be extrapolated to gain the temperature difference ΔT_∞ at indefinite long times. The software from Quantum Design, Inc. uses the following fitting function to obtain ΔT_∞:

$$\Delta T_{model} = \Delta T_\infty \cdot \left\{ \frac{1 - \left[\tau_1 \cdot \exp\left(\frac{-t}{\tau_1}\right) - \tau_2 \exp\left(\frac{-t}{\tau_2}\right) \right]}{\tau_1 - \tau_2} \right\}. \tag{2.7.15}$$

The time constants τ_1 and τ_2 are long and short empirical time constants. The Software by Quantum Design, Inc. calculates the heat flow through the sample by considering the power of the resistive heater minus the losses due to radiation. The radiation losses increase with increasing temperature and make measurements at room temperature or above very challenging.[§]

The measurements were conducted in a Physical Property Measurement System (Physical Property Measurement System Thermal Transport Option, Quantum Design, Inc., USA) by Iliya Radulov (FG Funktionale Materialien, TU Darmstadt). The heater power was adjusted to 0.04 W.[**] The sample geometry was a cylinder with an area of the surfaces at the hot and cold end of 26.3 mm^2 and a length of 6 mm. Copper leads were glued on both sides of the sample. The size of the leads fitted to the surface of the sample. Silver glue was used to obtain good thermal connection between the sample and the leads. To account for the thermal radiation losses the infrared emissivity was set to 0.9.[239, 240]

2.8. Electrocaloric Analysis (Direct Method)

The electrocaloric effect can be determined by either measuring the temperature change or the heat that is absorbed/released due to the entropy change of the dipolar entities. Measurement techniques for both were developed. Heat changes are generally measured with modified DSC instruments that are commercially available. Temperature changes can be measured by a suitable thermometer, i.e. thermocouple or thermistor. In every case it is necessary to conduct the measurement in a chamber with good temperature stability. A typical measurement curve is shown in Figure 2.8.1. The measurement principle is to apply an electric field in a short time span, fast rising time, and track the temperature of the sample. After a long enough holding time the system relaxes back to the initial bath temperature and

[§] From the manual of Quantum Design, Inc. an error in the range ±1 mW K^{-1} can be expected around 300 K. For the geometry used in the experiments this results in an error of ±10 %.

[**] With the used sample geometry and assumed thermal conductivity between 1-3 W m^{-1} K^{-1} this results in a temperature difference between the hot and the cold end of 3-9 K.

the electric field is removed in a short time span. The temperature of the sample will exhibit a jump at the point where the electric field is applied and a second jump at the time where the electric field is removed. By analyzing the temperature jumps, the electrocaloric temperature change can be deduced.

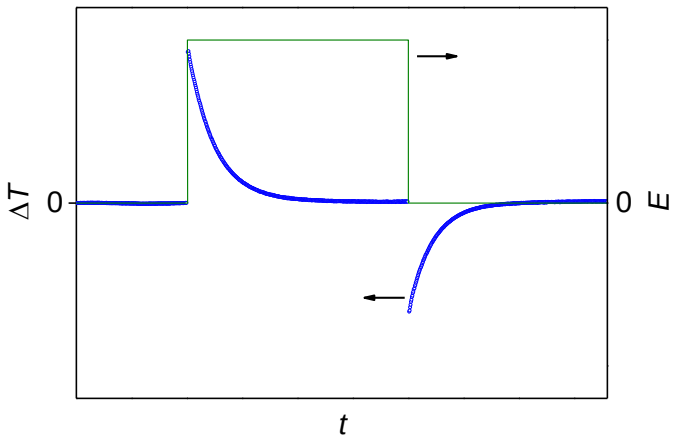

Fig. 2.8.1: Measured electrocaloric effect data: Blue circles show the change in sample temperature during electrocaloric measurement cycle. Green line shows the applied electric field function.

The measurements were conducted in the measurement chamber used for ac calorimetry. A schematic of the setup and the instruments used is given in Figure 2.8.2. a) and b). Electrodes were sputtered on both surfaces of the sample. To prevent electric sparks over the edge of the thin sample (~0.2 mm) not the whole surface was sputtered. A small area on the outer edge was kept free of electrode. This area did not contribute to the ECE. For application of an electric field copper wires were glued on the sample with a small amount of silver conducting varnish. The temperature was measured with a small bead thermistor (GAGR150KM3976J15, TE connectivity, Switzerland). The measurement procedure was controlled by a LabView program written by Patrick Breckner (FG Nichtmetallisch Anorganische Werkstoffe, TU Darmstadt). The step-like voltage signal was given out by a measuring board to a high voltage amplifier (High Voltage Amplifier 610E, TRek Inc., USA). The rising/falling time was 0.1 ms. The resistivity of the small bead thermistor was measured by a digital multimeter (34401A Multimeter, Hewlett Packard, USA). During the measurement the chamber temperature was kept constant within 0.2 mK. The temperature of the chamber is controlled by a temperature controller with connection to a flexible heater. The platinum resistor (PRT), which measured the chamber temperature, was read out by a digital multimeter (2001 Multimeter, Keithley, USA). The measurement chamber can be heated up till 460 K and cooled down till ~80 K. The cooling is achieved by putting the whole measurement chamber in a Dewar flask filled with liquid nitrogen.

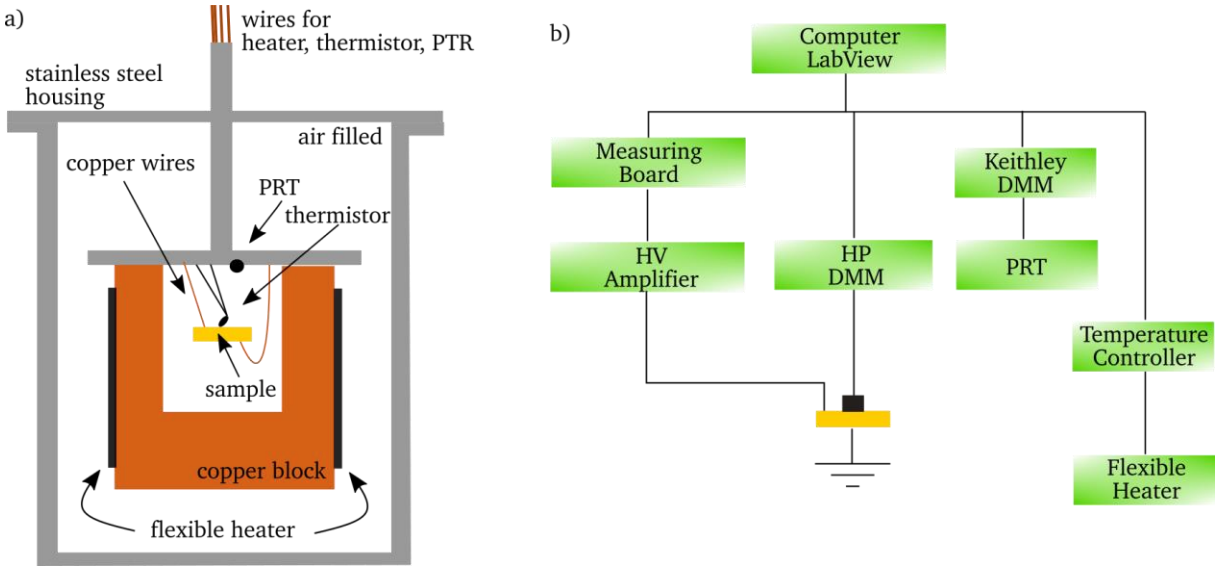

Fig. 2.8.2: Setup for electrocaloric measurements. a) Diagram showing the components of the home built measurement chamber. b) Schematic showing the measurement components and instruments used.

It has to be considered that the measurement points in Figure 2.8.1 reflect the temperature of the thermistor. To assume that this temperature is at the same time the temperature of the sample certain conditions have to be fulfilled. The time constant for heat transfer between the sample and the thermistor has to be much smaller than the time constant of heat conduction to the chamber. Furthermore, the heat capacity of the thermistor should be much lower than the heat capacity of the sample. To analyze the system a thermal equivalent circuit can be constructed (one-dimensional heat flow is considered which is sufficient for this purpose).

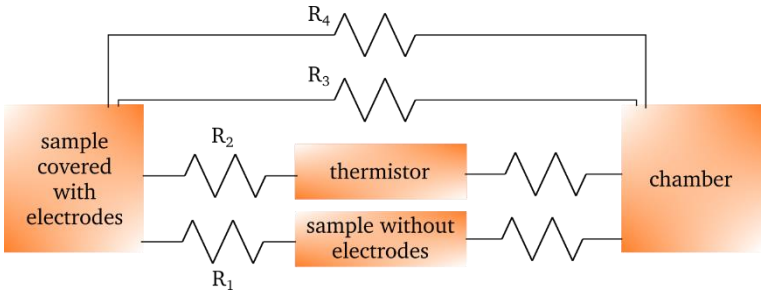

Fig. 2.8.3.: Schematic representation of the thermal subsystems and their coupling. Each subsystem has its own heat capacity and the coupling is represented by the thermal resistance R_i, i=1,2,3,4.

The whole system consisted of different subsystems, i.e. the sample covered by the electrodes, the part of the sample not covered by the electrodes and the thermistor. The subsystems are thermally coupled with each other and linked to the bath (chamber), represented by the thermal resistances R_i(i=1,2,3,4). Every subsystem has its own heat capacity. It is assumed that no thermal gradients exist at any time inside the subsystems (internal heat diffusion is fast). By analyzing the single time constants between the subsystems it can be shown that in fact the measured data points reflect the electrocaloric

temperature change (a correction factor accounting for the heat capacities of the subsystems has to be introduced).

First the thermal time constant for heat transfer from the sample covered with electrodes to the sample not covered by the electrodes is considered. The thermal resistance for the disk shape can be calculated by:

$$R_1 = \frac{\ln(\frac{r_{out}}{r_{in}})}{2\pi d\kappa}, \tag{2.8.1}$$

where r_{out}, r_{in}, d, κ are the radius of the sample, the radius of the electrode, the thickness and the thermal conductivity. For a typical sample geometry ($r_{out} = 3.75$ mm, $r_{in} = 3.4$ mm and $d = 0.2$ mm) and an assumed thermal conductivity of 2 W m^{-1} K^{-1}, this leads to a thermal resistance of ~39 K W^{-1}. The heat capacity is assumed by the mass of the sample without electrode (m~0.009 g) and the specific heat capacity ~0.4 J g^{-1} K^{-1}. This leads to a thermal time constant of:

$$\tau_1 = R_1 \cdot C_1 = 0.14 \text{ s}. \tag{2.8.2}$$

After $5 \cdot \tau_1 = 0.7$ s the temperature equilibration reached 99.2 %. The second time constant considered is for the heat transfer between the sample covered with electrodes and the thermistor. The time constant is estimated in the same manner with a contact conductance for the contact between sample and thermistor of $h_c = 3000$ W m^{-2} K^{-1} and the thermistor geometry.[241] This leads to a time constant of $\tau_2 = 0.7$ s. This is still a fast process compared to the time constants connecting the sample to the bath. R_3 and R_4 are considered to be the thermal connections between sample and bath by convection and the wires, respectively. Convection takes place over the surface of the sample via heat transfer to the surrounding air. A heat transfer coefficient of $h = 10$ W m^{-2} K^{-1} can be assumed.[242] [243] The thermal time constant is then $\tau_3 = 25$ s, which is considerably longer than τ_1 and τ_2. The heat transfer over the wires is considered by the contact conductance of $h_c = 8500$ W m^{-2} K^{-1} between the sample and the wires and the geometry of a wire (diameter of 0.06 mm).[241] The thermal time constant is then $\tau_4 =$ 420 s.

The assumptions made show that the heat transfer between the sample and the part of the sample without electrodes and the thermistor are fast processes compared to the thermal transfer to the bath. The fast thermal time constants τ_1 and τ_2 make it possible to consider the sample with electrodes, without electrodes and thermistor as one thermal system that slowly exchanges heat to the bath. By this assumption the measured temperature change data can be analyzed by a single external time constant (τ_{ext}):

$$\Delta T(t) = T_{bath} + \Delta T e^{-\frac{t}{\tau_{ext}}}. \quad (2.8.3)$$

To account for the heat transfer to the part of the sample without electrodes and the thermistor the temperature change ΔT from equation 2.8.3 can be corrected by a factor considering the heat capacities of the involved subsystems:[244]

$$\Delta T_{EC} = \Delta T \frac{\sum_i C_p^i}{C_p^{EC}}, \quad (2.8.4)$$

where C_p^i stands for the heat capacities of all subsystems involved in the fast internal equilibration and C_p^{EC} is the heat capacity of the sample covered with electrodes.

The measurement system used in this work (described before) was compared with other measurement setups from the groups of the University of Oulu (Oulu, Finland)[245], University of Duisburg-Essen (Duisburg, Germany)[231] and Imperial College London (London, United Kingdom)[246]. As test samples multilayer ceramics of 0.92 $Pb(Mg_{1/3}Nb_{2/3})O_3$-0.08 $PbTiO_3$ from the same batch were used.[247] Comparison between the different setups, i.e. modified DSC, adiabatic calorimeter, thermocouple temperature reading and thermistor temperature reading (this work), is given in Table 2.8.1. All four measurement setups revealed similar values for the electrocaloric temperature change. Especially, the thermistor temperature reading (this work) and the adiabatic calorimeter showed good agreement with differences in the temperature change <3 %. The thermocouple temperature reading exhibited the same temperature evolution under the same applied electric field, but with values slightly higher (~14 %) than thermistor temperature reading and adiabatic calorimeter. This might be due to the measurement procedure of short pulse time (~5 s), i.e. holding time with applied electric field. The sample temperature has no time to relax back to the bath temperature and determination of the electrocaloric temperature change is more difficult. The temperature changes deduced from the modified DSC are in between the thermocouple temperature reading and thermistor temperature reading. The DSC method measures the enthalpy changes, i.e. heat flow out/into the sample, and the electrocaloric temperature change can be calculated by $\Delta T = Q/c_p$. This makes it necessary to precisely determine the specific heat capacity of the sample. Other problems may arise when integration over the heat flow curve is done. Due to those difficulties in translating the heat flow curve into a temperature change, the slight discrepancy (9-14 %) between the modified DSC and the other techniques might be explained.

Table 2.8.1: Comparison of different direct measurement methods of the electrocaloric effect (modified from Molin et al.[247]).

	Advantages & Shortcomings
Thermistor temperature reading Temperature range: 77 K-460 K Temperature stabilization: ±2 mK	Direct temperature measurement Long measurement time (can be reduced) Corrections necessary by equation 2.8.4
Thermocouple temperature reading Temperature range: 77 K-573 K Temperature stabilization: ±1 mK	Direct temperature measurement Short measurement time Corrections necessary by equation 2.8.4 Sample breakdown can lead to setup damage
Adiabatic calorimeter Temperature range: 260 K-435 K Temperature stabilization: ±10 mK	Direct temperature measurement Good insulation of the calorimeter Poor thermal contact between thermocouple and sample
Modified DSC Temperature range: 77 K-443 K Temperature stabilization: <100 mK	Good insulation of the calorimeter Quasi-direct method Additional information about specific heat capacity needed Limited sample dimensions

2.9. Current Density Analysis

The current flowing through a sample under the application of a large electric field was measured. The sample was a disk in parallel plate geometry. Therefore, the current density can be evaluated by dividing the measured current with the surface area of the electrode ($J=I/A$). From the measured current density, the conductivity can be deduced from the relation $J=\sigma \cdot E$.

The current was measured with an electrometer with internal power source (6517 electrometer/high resistance system, Keithley, USA). The sample was connected in series with the power source of the electrometer. Measurements were controlled by a LabView program written by Patrick Breckner (FG Nichtmetallisch Anorganische Werkstoffe, TU Darmstadt). The measurement was conducted with stepwise increasing/decreasing of the electric field. Every electric field step was hold for 2 s in order to discern between dipolar current and the leakage current.

3. Results & Discussion

3.1. The Materials Measure of Cooling Power

An increasing number of ferroelectric materials were identified that potentially can serve as an electrocaloric material in a solid state cooling device. As an addition to the comparison on basis of the electrocaloric temperature change, a material related cooling power can be useful. The cooling power accounts for the thermodynamic cycle a possible device will operate at, by including the frequency of the cycle. Some studies compared the electrocaloric cooling power for prototypes.[5, 7, 15] Those results are sensitive to the specific device design and therefore make it impossible to compare the electrocaloric materials itself. A material cooling power is needed that excludes device-level parameter and makes a comparison of materials possible.

In this section a material related cooling power will be derived that includes the thermophysical properties, i.e. specific heat capacity and thermal conductivity. Two single crystals with [001] cut, one of barium titanate and one of lead magnesium niobate – lead titanate, were chosen to derive the material cooling power. Those materials are representatives of a classical ferroelectric with first order phase transition, i.e. BT, and a relaxor-like behavior, i.e. PMN-28PT. The representative quality of the measured single crystals is demonstrated by dielectric permittivity and polarization measurements. Furthermore, specific heat capacity and thermal diffusivity was acquired from the samples. All measurements were conducted by Richard Perez Moyet (Materials Science, University of Connecticut). An equation for the material cooling power was derived based on a Newtonian cooling model of a thin plate. The section is based on published results.[248]

The properties of ferroelectrics change most pronounced around their ferroelectric to paraelectric and interferroelectric phase transitions. To obtain the temperatures of those phase transitions and to assess the nature of the phase transition, dielectric permittivity measurements over a broad temperature range are useful. Comparing the dielectric permittivity and polarization measurements with literature enables to qualitatively determine the quality of crystals. The dielectric permittivity and loss tangent for a [001] cut BT crystal is shown in Figure 3.1.1 a) and for a [001] cut PMN-PT crystal in Figure 3.1.1 b).

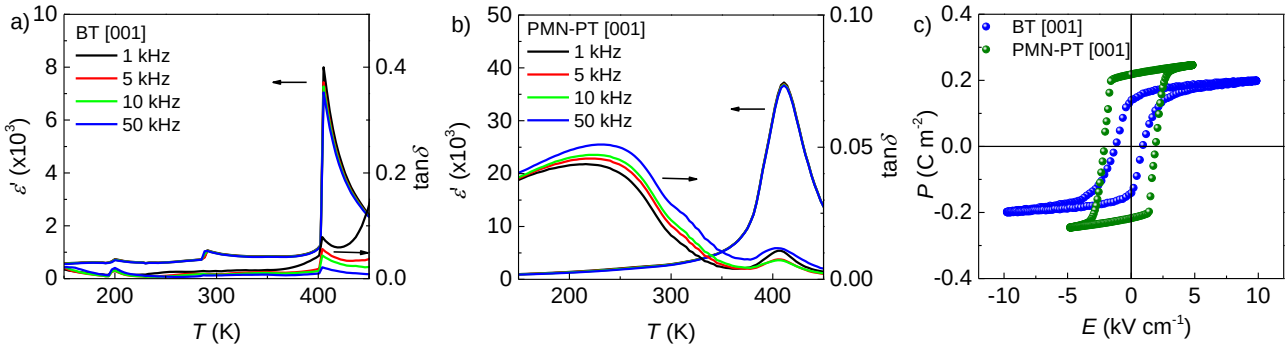

Fig. 3.1.1: a) Dielectric permittivity and loss tangent as a function of temperature for a BT single crystal with crystal orientation [001]. b) Dielectric permittivity and loss tangent as a function of temperature for a PMN-PT single crystal with crystal orientation [001]. c) Polarization versus applied electric field at room temperature for a BT single crystal with crystal orientation [001] and a PMN-PT single crystal with crystal orientation [001].

The zero-field structural phase transitions of BT can be observed from the peaks in the dielectric permittivity and loss tangent. Under heating from low temperatures the BT crystal undergoes several phase transitions, i.e. rhombohedral $\xrightarrow{\sim 200\ K}$ orthorhombic $\xrightarrow{\sim 291\ K}$ tetragonal $\xrightarrow{\sim 404\ K}$ cubic. The observed phase transition temperatures and values of the dielectric permittivity agree well with literature data.[90] In comparison to the BT crystal, the PMN-PT crystal features only one phase transition in the observed temperature range. The peak in the dielectric permittivity and the loss tangent at ~405 K is associated with a tetragonal to cubic phase transition under heating.[121, 245, 249] The broadness of the peak in dielectric permittivity shows that PMN-PT features a relaxor character and is described as relaxor-like in this section.

The $P-E$ loops shown in Figure 3.1.1 c) were acquired in the tetragonal ferroelectric phase for the [001] cut BT and PMN-PT crystal. The hysteresis loops display symmetric polarization and coercive electric fields. The obtained saturation and remanent polarization values coincide with literature values.[90, 245, 249] The obtained results from the dielectric permittivity measurements and $P-E$ loops confirm that the used crystals are representative for BT and PMN-PT, and that the subsequent thermophysical measurements display the features of BT and PMN-PT.

The thermophysical properties determine the heat flux in the EC material and how fast heat can be transferred in or out of the EC material. Therefore, they are important for the material cooling power and shown together with the EC response in Figure 3.1.2.

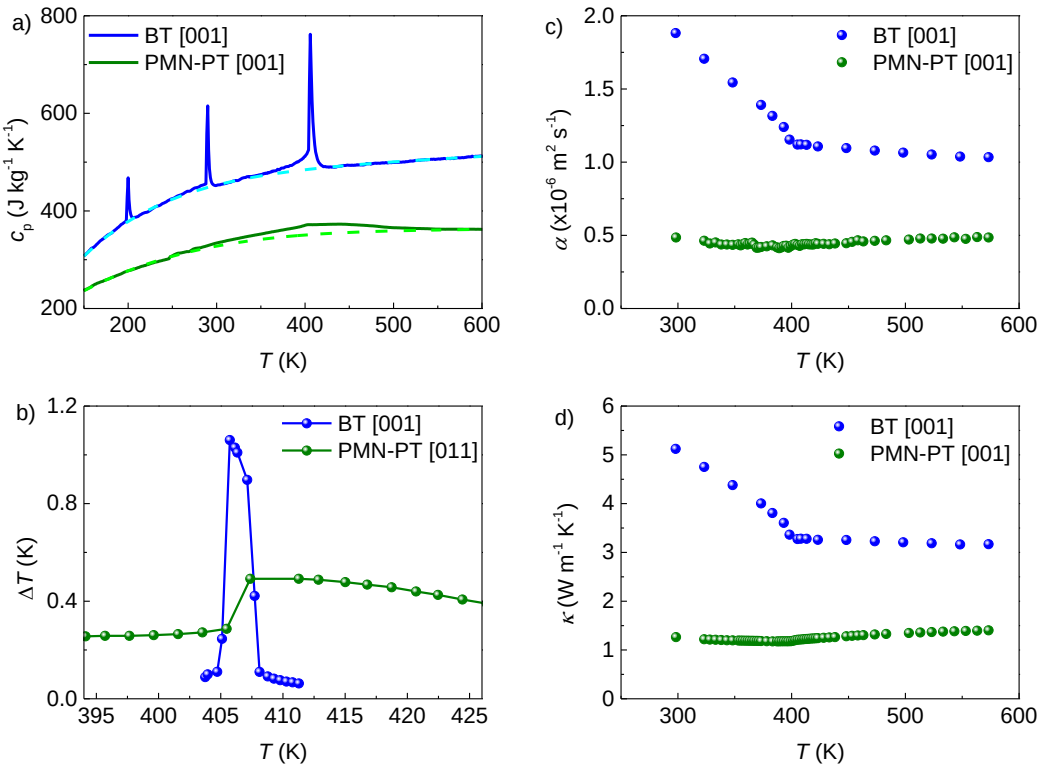

Fig. 3.1.2: a) Specific heat capacity as a function of temperature for a BT single crystal with crystal orientation [001] and a PMN-PT single crystal with crystal orientation [001]. The dashed lines denote the lattice hard mode to the specific heat capacity, obtained by fitting the measured specific heat capacity at temperature ranges away from the phase transitions. b) Electrocaloric temperature change as a function of temperature for a BT single crystal with crystal orientation [001] and a PMN-PT single crystal with crystal orientation [011]. Data points are taken from literature at an electric field removal from 8 kV cm^{-1} to 0 kV cm^{-1}.[116, 245] The electrocaloric behavior for a [001] cut crystal and a [011] cut crystal can be assumed to be similar.[246] c) Thermal diffusivity as a function of temperature for a BT single crystal with crystal orientation [001] and a PMN-PT single crystal with crystal orientation [001]. d) Thermal conductivity as a function of temperature for a BT single crystal with crystal orientation [001] and a PMN-PT single crystal with crystal orientation [001]. Data points are deduced from the measured thermal diffusivity and specific heat capacity.

The specific heat capacities of the BT and PMN-PT crystal are shown in Figure 3.1.2 a). From the measurement of specific heat capacity the phase transition temperatures can be deduced. Due to the enthalpy changes around interferroelectric and ferroelectric to paraelectric phase transitions and the possibility of latent heat at first order phase transitions, peaks in the specific heat capacity occur. The obtained phase transition temperatures for BT coincide with the temperatures obtained from the dielectric permittivity measurements. The mass specific heat capacity of PMN-PT is lower than for BT as PMN-PT has a larger molar mass than BT. In Figure 3.1.2 a) the lattice hard mode specific heat capacity is depicted by the dashed lines. If this lattice specific heat capacity is subtracted from the total specific heat capacity the excess specific heat capacity is obtained that features the enthalpy change and latent heat due to the phase transition. The sharp anomalies in BT highlight the first order character of the phase transitions. It should be noted that such sharp anomalies are not a proof for first order phase transitions, as such behavior can be also seen for second order phase transitions with extensive

pretransitional wings of enthalpy change.[234] Nevertheless, for BT it is known that the ferroelectric to paraelectric phase transition is of first order nature. The excess specific heat capacity of PMN-PT shows different behavior with a small anomaly over a broad temperature range. This observation reflects the relaxor-like behavior of this material.

Naturally, the EC performance of the materials is important for the material cooling power. The EC temperature change in the temperature range around the ferroelectric to paraelectric phase transition is depicted in Figure 3.1.2 b). The values of the EC temperature change are taken from literature.[116, 245] Values for the same composition of PMN-PT are only found for a [011] crystal, but data for a PMN-PT composition with x=0.30 suggest that the EC performance of an [011] cut crystal is similar to a [001] cut crystal.[246] For BT and PMN-PT the largest EC temperature changes can be observed at the phase transition temperature. Here, an applied electric field can induce the ferroelectric phase and thereby large enthalpy changes can be achieved with accompanied latent heat. For BT the temperature range where the applied electric field of 8 kV cm^{-1} can induce the ferroelectric field is limited to 405 K to 408 K. Substantial EC temperature changes of over 1 K can be achieved for BT. For PMN-PT the EC temperature change is nearly stable over a broader temperature range from 407 K until 425 K, but the maximum EC temperature change is ~0.5 K.

Another important thermophysical property is the thermal diffusivity. It gives a measure of heat transport in a material and is connected to the lattice specific heat capacity and thermal conductivity of a material. In Figure 3.1.2 c) the thermal diffusivity of BT and PMN-PT is shown and in Figure 3.1.2 d) the thermal conductivity is demonstrated, which was deduced from the measured thermal diffusivity and lattice specific heat capacity. It is found that the thermal diffusivity of BT decreases with temperature and exhibits an anomaly around the ferroelectric to paraelectric phase transition. At temperatures above the phase transition the thermal diffusivity is still decreasing. In contrast, the thermal diffusivity of PMN-PT is slightly increasing with temperature. A slight and broad anomaly is observed around the phase transition. At temperatures larger than the phase transition the thermal diffusivity is slightly increasing. The deduced thermal conductivity shows the same behavior as the thermal diffusivity since the lattice specific heat capacity is only slightly increasing in the measured temperature range. At elevated temperatures, such as the measured temperature range, the thermal conductivity for nonmetallic crystals should follow a 1/T – behavior.[250] This dependence might be expected for BT if a broader temperature range would be measured, but is hidden by the anomalous behavior around the phase transition. The anomalies in the thermal conductivity of ferroelectrics were related to the phonon-phonon interactions occurring at the phase transition where the soft phonon mode condensates.[144, 148, 251] The PMN-PT crystal exhibits an increasing thermal conductivity with temperature highlighting the glassy behavior. Such a glassy behavior in terms of thermal conductivity was found in relaxor ferroelectrics.[146-148]

From the thermophysical properties and EC response of BT and PMN-PT the different phase transition characteristics can be seen. Sharp anomalies are found for the BT around the ferroelectric to paraelectric phase transition. For PMN-PT small anomalies over a broad temperature range are observed reflecting the relaxor-like behavior. For the subsequent analysis of the material cooling power it is important to note that PMN-PT exhibits a smaller mass specific heat capacity, a smaller thermal conductivity and a smaller peak EC response.

To consider the material cooling power of an EC plate, the EC cycle has to be considered. Heat must be absorbed by the EC plate from one reservoir and released to another reservoir in a cyclic manner. A holding time (t_{hold}) must be introduced at which the EC plate has contact with the reservoir. The repetition of the EC cycle is then twice the holding time, as heat is exchanged at the hot and cold reservoir. The cycling frequency is then determined by the thermophysical properties that effect the heat transport through the thickness (L) of the EC plate. For the material cooling power only the heat exchanged at the cold reservoir, i.e. the reservoir that need to be cooled, is of interest. Therefore, the upper limit of the material cooling (Π) power can be expressed by considering the heat flux across the plane surface of the EC plate:

$$\Pi \leq \nu_{cycle} \cdot L \cdot Q_c, \tag{3.1.1}$$

where ν_{cycle} is the repetition rate of the cycle and Q_c is the heat absorbed at the cold reservoir. This can be expressed as well in terms of the holding time and a temperature change:

$$\Pi \leq \frac{1}{2t_{hold}} \cdot L \cdot (\rho c_p \Delta T_{cold}), \tag{3.1.2}$$

where ρ, c_p and ΔT_{cold} are the density, the mass specific heat capacity and the temperature difference between the EC plate and the reservoir. This temperature difference is not necessarily equal to the EC temperature change, but the EC temperature change describes an upper limit. The variables in Equation 3.1.2, i.e. t_{hold}, L and ΔT_{cold}, are interdependent, and it should be noted that they depend on the internal heat diffusion and on the external boundary conditions. In a device design it will be preferential that the heat flux is not dependent on the internal diffusion in the EC plate, meaning the EC material is not the limiting factor. So conditions are considered under which the heat flux inside the EC plate is fast enough. This condition is fulfilled if low Biot numbers, i.e. $Bi \leq 0.1$, are considered.[241] This will lead to Newtonian cooling/heating with negligible temperature gradients inside the material and fast heat transport towards the heat exchanging surface of the EC plate. Buffer layers of low heat flux near the interface can therefore be excluded. The Biot number is defined as:

$$Bi = \frac{hL_c}{\kappa}. \tag{3.1.3}$$

The heat transfer coefficient and the characteristic length are denoted as h and L_c, respectively. The characteristic length in the case considered is the thickness of the EC plate. A thermal lumped-capacity model can be used for the case of $Bi = 0.1$, where the EC plate is one lumped component.[241] To describe the temperature difference between the EC plate and the reservoir over time it is convenient to use the dimensionless temperature (Θ):

$$\Theta = \frac{T(t) - T_\infty}{T_i - T_\infty}. \tag{3.1.4}$$

The temperature at time t is $T(t)$, the temperature far away from the EC plate, i.e. the reservoir temperature which is considered for simplicity as constant (the thermal mass of the reservoir is large compared to the EC plate and heat flux does not considerably change the temperature of the reservoir), is T_∞, and the initial temperature of the EC plate is T_i. The dimensionless temperature is a measure of how advanced the temperature adjustment between the EC plate and reservoir is, or in other words how close the EC plate equilibrated the temperature to the reservoir. The dimensionless temperature can take values between 1 and 0, where 1 denotes that the EC plate has the initial temperature and 0 denotes that the temperature of the EC plate is equal to the reservoir temperature. Note that a dimensionless temperature of 0 requires infinite waiting time. With the assumptions described above the heat transfer problem can be described as a one-dimensional heat flow model and the solution to such a transient heat conduction problem is given by the simple lumped-capacity model with one lump,

$$\Theta = \exp\left[-\frac{ht}{\rho c_p L_c}\right] = \exp[-\frac{t}{\tau}]. \tag{3.1.5}$$

Here τ is the thermal time constant. Equation 3.1.5 can be further expressed with the Biot number and the Fourier number and it follows:

$$\Theta = \exp[-Fo \cdot Bi]. \tag{3.1.6}$$

The Fourier number is defined as:[241]

$$Fo = \frac{\alpha t}{L_c^2} = \frac{\kappa t}{\rho c_p L_c^2}. \tag{3.1.7}$$

Using Equation 3.1.6 and setting Bi=0.1, the relationship between the Fourier number and the dimensionless temperature follows as:

$$Fo = -\ln(\Theta) \cdot 10. \tag{3.1.8}$$

Using Equation 3.1.7 and Equation 3.1.8 the relation between the thickness, the dimensionless temperature and the holding time can be expressed as:

$$L = \frac{\sqrt{\kappa}\sqrt{t_{hold}}}{\sqrt{\rho c_p}\sqrt{-\ln(\Theta)\cdot 10}}. \tag{3.1.9}$$

Note that in Equation 3.1.9 the characteristic length L_c was substituted by the thickness L of the EC plate and the time t was substituted by the holding time t_{hold}. This relation between the interdependent variables L, t_{hold} and Θ is used to calculate the material cooling power by Equation 3.1.2. The maximum temperature difference that can be achieved between the EC plate and the reservoir is the electrocaloric temperature change, which is therefore used to calculate the material cooling power. It follows that the material cooling power is then:

$$\Pi = \frac{1}{2t_{hold}} \cdot \frac{\sqrt{\kappa}\sqrt{t_{hold}}}{\sqrt{\rho c_p}\sqrt{-\ln(\Theta)\cdot 10}} \cdot \rho c_p (1-\Theta)\Delta T. \tag{3.1.10}$$

Note that the temperature difference between the EC plate and the reservoir ΔT_{cold} is now replaced by the electrocaloric temperature change ΔT and the expression $(1-\Theta)$ denoting the degree of temperature equilibration between the EC plate and the reservoir. A dimensionless temperature of 1, meaning that the EC plate has initial temperature, results in no heat exchanged and zero material cooling power. A dimensionless temperature of 0, meaning that the EC plate reached the temperature of the reservoir (assumption of constant reservoir temperature), is not equivalent to maximum material cooling power as the dimensionless temperature itself is time dependent (see Equation 3.1.5). Further elucidation follows by the calculated material cooling power as function of the dimensionless temperature in Figure 3.1.3, Figure 3.1.4 and Figure 3.1.5.

The material cooling power can be determined by Equation 3.1.10 as a function of temperature dependent thermophysical properties and EC properties, the dimensionless temperature, holding time and the thickness of the EC plate.[††] First the sensitivity to the non-material specific parameters, i.e. holding time, dimensionless temperature and EC plate thickness, is considered. Figure 3.1.3 highlights the temperature dependent material cooling power as function of the dimensionless temperature for a) BT and b) PMN-PT. For the calculations the holding time was set to 0.5 s according to recent reports on EC device prototypes.[5, 6, 11-13, 15] For BT and PMN-PT the material cooling power largely increases right above the ferroelectric to paraelectric phase transition. The electric field induced phase transition with the accompanied enthalpy changes and latent heat leads to this behavior. This reflects the EC properties of BT and PMN-PT. It can be seen that PMN-PT exhibits a more constant material cooling power, in the temperature regime but also in the dimensionless temperature regime, compared to BT. Nevertheless, the material cooling power of BT slightly above the ferroelectric to paraelectric phase transition and in the medium dimensionless temperature regime, i.e. Θ=0.2-0.7, is much bigger than for PMN-PT. It

[††] The densities of BT are taken as 6020 kg m^{-3} and of PMN-PT as 7967 kg m^{-3}.

should be noted, that the maximum material cooling power for BT and PMN-PT over the whole temperature range is at a dimensionless temperature of ~0.28. The proportionality between the dimensionless temperature and the material cooling power is shown in Figure 3.1.3 c). The dependency can be expressed as:

$$\Pi \propto \frac{1}{\sqrt{-\ln(\Theta)}}(1-\Theta) \tag{3.1.11}$$

The local maximum for such a function, in the range of the dimensionless temperature between 0 and 1, is at ~0.28. The same maximum would be obtained if a smaller or larger holding time would be used, as the proportionality of the material cooling power on the holding time does not exhibit a local maximum. Such a maximum in the material cooling power at Θ=0.28 can be understood considering that for complete temperature equilibration between the EC plate and the reservoir infinitively large times would be needed, see Equation 3.1.5. A dimensionless temperature of 0.28 implies that only 72 % of Q_c was exchanged (Note that the exchanged heat is directly related to the temperature equilibration in this case, because no gradients in the EC plate are assumed at any time). In this case the material efficiency (Equation 1.3.19) will be 0.72 times the maximum material efficiency. This shows that the maximum material cooling power does not coincide with the maximum material efficiency.

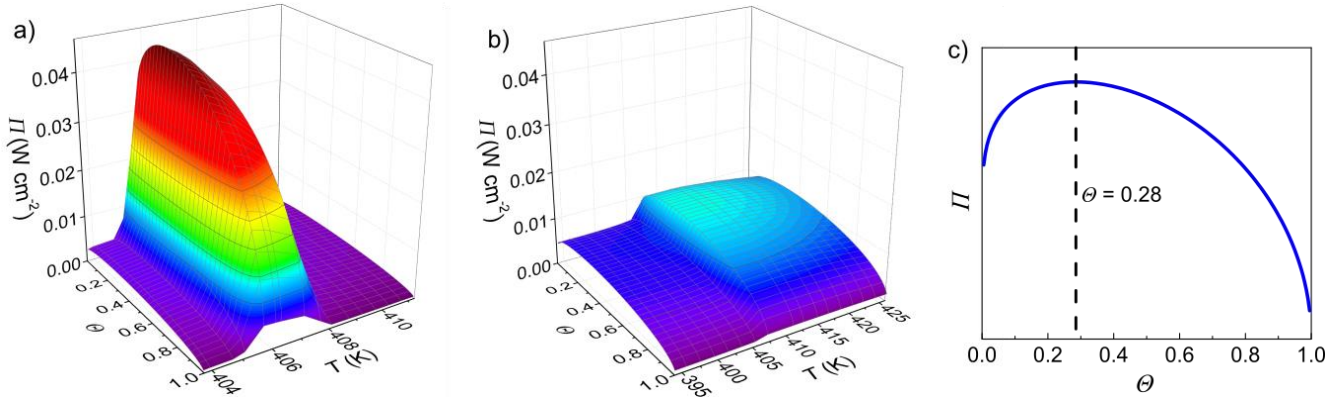

Fig. 3.1.3: The material cooling power (Π) as a function of temperature and dimensionless temperature (Θ) for a) BT and b) PMN-PT. Calculations were performed with a holding time t_{hold} = 0.5 s. The axis range for the material cooling power and surface color gradient in a) and b) are chosen equal. c) Proportionality between material cooling power and dimensionless temperature. A maximum in the material cooling power can be found at a dimensionless temperature of ~0.28.

The thickness of the EC plate is related to the dimensionless temperature by Equation 3.1.9. In Figure 3.1.4 the material cooling power as a function of the temperature and thickness of the EC plate is given in a) for BT and b) for PMN-PT. The holding time for the calculations is set to 0.5 s like for Figure 3.1.3. Similar behavior can be seen like for the dependency on the dimensionless temperature. The BT exhibits large material cooling power just above the ferroelectric to paraelectric phase transition temperature. For PMN-PT the same accounts, but the material cooling power is more constant over the whole temperature and thickness regime. For BT and PMN-PT a maximum material cooling power can be found

at a certain thickness. This thickness is related to the maximum in the dimensionless temperature of 0.28, but it is not constant as it depends on the thermophysical properties which vary with temperature. The optimum thickness, i.e. at Θ=0.28, for BT is depicted as function of temperature in Figure 3.1.4 c). In the highlighted temperature range where large EC properties occur the optimum thickness for BT varies only slightly from 0.2116 mm at 404 K to 0.2113 mm at 411 K. In this temperature range the thermophysical properties are nearly constant. It can be seen from Figure 3.1.2 a) and d) that the thermophysical properties can vary more strong if larger temperature ranges are considered. It plays a role at lower temperatures where the specific heat capacity drastically decreases and strong increase of the thermal conductivity can occur in ferroelectrics where the Umklapp-processes are vanishing.

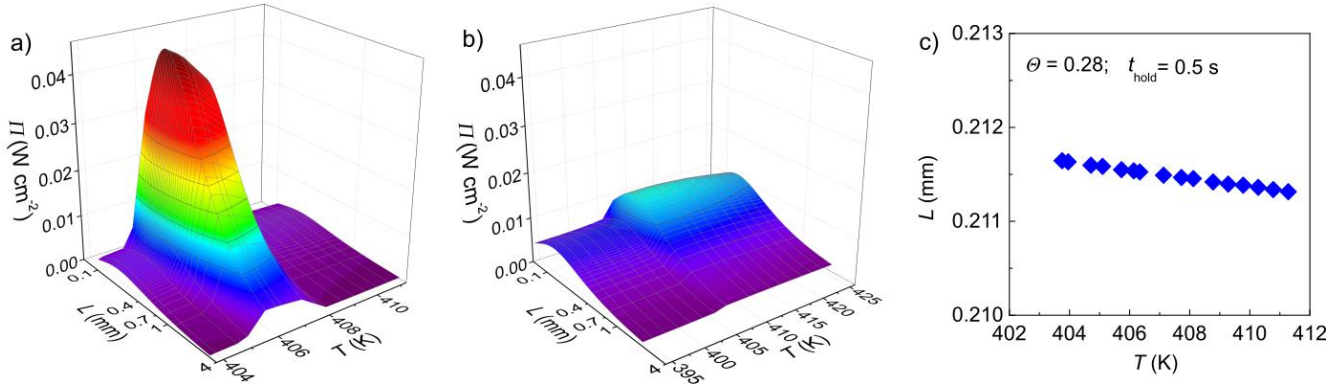

Fig. 3.1.4: The material cooling power (Π) as a function of temperature and thickness (L) for a) BT and b) PMN-PT. Calculations were performed with a holding time t_{hold} = 0.5 s. The axis range for the material cooling power and surface color gradient in a) and b) are chosen equal. c) Optimum thickness as function of temperature for barium titanate. Calculations were performed with Θ = 0.28 and t_{hold} = 0.5 s.

The dependency of the material cooling power on the holding time is depicted in Figure 3.1.5 a) for BT and b) for PMN-PT. For the calculations the dimensionless temperature is set to 0.28. The proportionality between the material cooling power and the holding time is given by:

$$\Pi \propto \frac{1}{\sqrt{t_{hold}}} \tag{3.1.12}$$

This demonstrates the behavior displayed in Figure 3.1.5 a) and b). The material cooling power is largely increasing if the holding time is decreased. This is best seen for BT just above the ferroelectric to paraelectric phase transition. At the calculations before with a holding time of 0.5 s the material cooling power was ~0.04 W cm^{-2}, whereas by decreasing the holding time to 0.02 s the material cooling power increased to ~0.2 W cm^{-2}. In Figure 3.1.5 c) the optimum thickness at Θ=0.28 as function of the holding time for BT at 407 K is shown. It is demonstrated that the optimum thickness decreases as the holding time decreases. The proportionality between the material cooling power and the holding time exhibits no local maximum and therefore the material cooling power can be arbitrarily increased by decreasing the holding time. It should be noted that this is just a consideration of the material and that the holding

time in a real device will be dictated by the device structure. Therefore, in a real device no arbitrarily small holding time can be chosen.

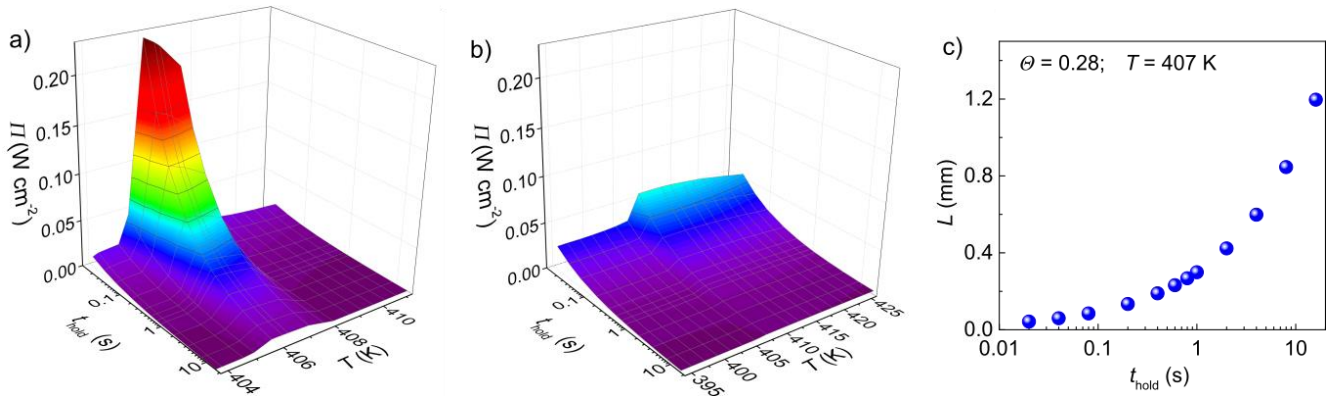

Fig. 3.1.5: The material cooling power (Π) as a function of temperature and holding time (t_{hold}) for a) BT and b) PMN-PT. Calculations were performed with a dimensionless temperature Θ = 0.28. The axis range for the material cooling power and surface color gradient in a) and b) are chosen equal. c) Optimum thickness as function of holding time for barium titanate at T = 407 K and a dimensionless temperature of Θ = 0.28.

Highlighted in Figure 3.1.3, Figure 3.1.4 and Figure 3.1.5 the material cooling power can be used to compare EC materials on basis of reasonable values if the holding time is set to 0.5 s (according to recent prototypes) and a dimensionless temperature of 0.28 (consistent with the maximum in the material cooling power). In Figure 3.1.6 a) the EC temperature change of BT and PMN-PT (same as Figure 3.1.2) is depicted as well as b) the optimum thickness for BT and PMN-PT and c) the material cooling power of BT and PMN-PT.

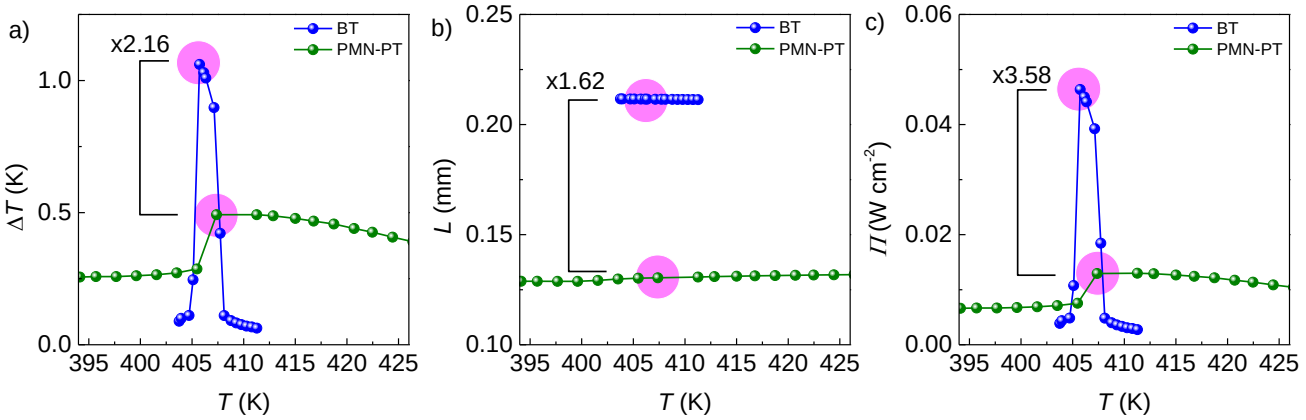

Fig. 3.1.6: a) Electrocaloric temperature change as a function of temperature for BT and PMN-PT. Data is the same as Figure 3.1.2 b). The peak electrocaloric temperature change (highlighted by pink areas) of BT is 2.16 times larger than for PMN-PT. b) Optimum thickness, according to the calculated material cooling power, as a function of temperature for BT and PMN-PT. The optimum thickness (highlighted by pink areas) of BT is 1.62 times larger than for PMN-PT. c) Material cooling power as a function of temperature for BT and PMN-PT. The peak material cooling power (highlighted by pink areas) of BT is 3.58 times larger than for PMN-PT.

Comparison of BT and PMN-PT is done at the temperature of peak values, i.e. 406 K for BT and 407 K for PMN-PT. It can be seen that the EC temperature change of BT is 2.16 times larger ($\Delta T_{BT}/\Delta T_{PMN-PT}$) than the one for PMN-PT. At the same time also the optimum thickness of BT is 1.62 times larger (L_{BT}/L_{PMN-PT}) than PMN-PT. This is related to the superior thermophysical properties of BT. The specific heat capacity as well as the thermal conductivity are larger for BT. Both, the EC properties and the thermophysical properties, influence the material cooling power. The peak material cooling power of BT is 3.58 times (Π_{BT}/Π_{PMN-PT}) the one of PMN-PT. This is the product of the superior EC temperature change and the thermophysical properties (2.16·1.62=3.5). The small discrepancy between 3.5 and 3.58 results from the volumetric specific heat capacity, i.e. $\rho \cdot c_p$ (compare Equation 3.1.10 with Equation 3.1.9). The volumetric specific heat capacity at 406 K for BT is 2859956 J m^{-3} K^{-1} and for PMN-PT at 407 K is 2788450 J m^{-3} K^{-1}. This means the volumetric heat capacity of BT is ~2 % larger than for PMN-PT. It can be concluded that the material cooling power is a useful figure of merit comparing EC materials with each other, because it includes the thermophysical properties that are not considered in the materials efficiency. Nevertheless, like the comparison on basis of the EC temperature change or the material efficiency, the material cooling power does not include the temperature range at which a material is superior to another. Even though the peak value of the material cooling power in BT is larger than in PMN-PT it should be taken care that those large values can only be achieved in a very narrow temperature range. In PMN-PT the temperature range of slowly varying material cooling power is much larger.

Considering the above discussion it is found that the thermophysical properties of EC materials are important and can be included together with the EC properties in a figure of merit. The material cooling power has a proportionality to the thermophysical and EC properties:

$$\Pi \propto \sqrt{\kappa}\sqrt{\rho c_p}\Delta T \tag{3.1.13}$$

The material cooling power can be increased by increasing the thermal conductivity. The volumetric specific heat capacity might be similar for most ferroelectrics. To conclude the development of the material cooling power, it should be recognized that thermophysical properties are important in the consideration of EC materials and superior thermal conductivity can compensate partly for lower EC responses.

3.2. The $Ba(Zr_xTi_{1-x})O_3$ System

The $Ba(Zr_xTi_{1-x})O_3$ system is advantageous in studying the influence of phase transition behavior on the beforehand derived figure of merit, i.e. the material related cooling power. By increasing the zirconium content, starting from pure barium titanate, the phase transition behavior changes from first order character to second order character, diffusive and relaxor-like behavior. Those differing phase transition characteristics determine the EC properties and thermophysical properties. The $Ba(Zr_xTi_{1-x})O_3$ system was considered as an EC material before, especially because the phase transition of BT can be shifted towards room temperature by increasing the zirconium content. Nevertheless, no detailed study was conducted on the thermophysical properties.

In this section several $Ba(Zr_xTi_{1-x})O_3$ compositions are characterized. The crystal structure and microstructure is analyzed. Dielectric permittivity data is used to describe the phase transition characteristics. Those phase transition characteristics are as well reflected in the specific heat capacity and thermal conductivity. The thermophysical properties and directly measured EC temperature changes are used to compare the $Ba(Zr_xTi_{1-x})O_3$ compositions on basis of the material related cooling power. Furthermore, the material related cooling power is used to compare the different caloric effects, i.e. mechanocaloric effect, magnetocaloric effect and electrocaloric effect, with each other. This section is based on unpublished results.

The investigated $Ba(Zr_xTi_{1-x})O_3$ compositions ranged from pure BT (as a reference material for the thermophysical behavior) to $Ba(Zr_{0.35}Ti_{0.65})O_3$. To assess the phase purity and incorporation of zirconium into the BT lattice the XRD patterns were recorded at room temperature. Note that at room temperature the crystal structure is different depending on the composition. The recorded XRD patterns are depicted in Figure 3.2.1 a) and b). No secondary phases could be observed within the detection limit of the measurement system. To determine the unit cell volume, and by this see if the zirconium was incorporated into the BT lattice, the peak at $2\theta \sim 45°$ was analyzed. For the tetragonal P4mm structure a peak splitting should be observed, which is the case for pure BT.[193] For the compositions from $x=0.08$ to $x=0.20$ only one peak was observed, because at room temperature those compositions were in the rhombohedral R3m phase.[201, 204, 252] The compositions with $x \geq 0.25$ exhibit a cubic $Pm\bar{3}m$ structure with one peak in the angular range.[73, 206, 212] It is found that the peaks shift towards lower angles with increasing zirconium content. This suggests an increasing unit cell volume, which is in accordance to the larger ionic radius of Zr^{4+} in comparison with Ti^{4+} and Vegard's law.[253, 254]

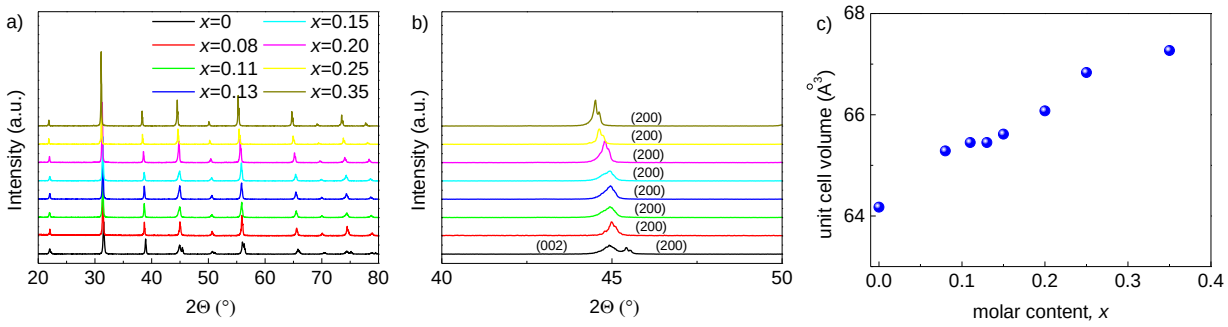

Fig. 3.2.1: a) XRD pattern recorded at room temperature of $Ba(Zr_xTi_{1-x})O_3$ compositions in the range from 2θ=20° - 80°. b) XRD pattern recorded at room temperature of $Ba(Zr_xTi_{1-x})O_3$ compositions in the range from 2θ=40° - 50°. c) Unit cell volume of $Ba(Zr_xTi_{1-x})O_3$ compositions calculated from the recorded XRD pattern.

To confirm the incorporation of zirconium into the BT lattice the unit cell volume was calculated, shown in Figure 3.2.1. c). The unit cell volume of BT is with ~64.17 Å^3 in accordance to literature.[193] With increasing zirconium content, the unit cell volume increases. It has to be noted that the unit cell volume for the compositions in the rhombohedral R3m phase were calculated with an angle of 90°. Nevertheless, by structural investigations it was demonstrated that the angle in the rhombohedral phase is only slightly different from 90° and therefore minor mistakes are made in the calculation of the unit cell volume.[201, 204] From the presented XRD results it can be concluded that zirconium was fully incorporated into the BT lattice.

For BT based materials it was demonstrated that the grain size can have large influences on the properties for fine grained materials, i.e. grain size below 1 μm.[255, 256] This was related to elastic constraints that develop during the paraelectric to ferroelectric phase transition. The elastic constraints are inhomogeneously stressed grain boundary regions that substantially reach into the grain for small grain sizes. This grain clamping prevents full transformation strain, tending the structure towards a cubic symmetry.[257] The grain size for the investigated samples was determined from optical microscope images, which were analyzed by a linear intercept method. The determined grain size is depicted in Figure 3.2.2. It can be seen that all compositions have much larger grain sizes than 1 μm and therefore negligible influence from internal stresses is expected. The density from samples of all compositions was measured by the Archimedes method and relative densities over 94 % were found.

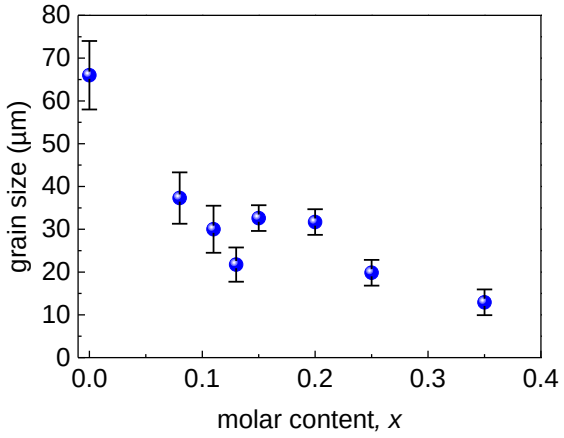

Fig. 3.2.2: Grain size for $Ba(Zr_xTi_{1-x})O_3$ compositions determined from optical microscope images.

To assess the phase transition characteristics of the investigated $Ba(Zr_xTi_{1-x})O_3$ compositions, dielectric measurements were performed, see Figure 3.2.3 a) and b). It is observed that by increasing the zirconium content, the paraelectric to ferroelectric phase transition temperature decreases. For $Ba(Zr_{0.08}Ti_{0.92})O_3$ three consecutive phase transitions can be observed as peaks in the imaginary dielectric permittivity. The cubic structure transforms into a tetragonal one at ~368 K, followed by a transition into an orthorhombic structure at ~343 K and into a rhombohedral one at ~322 K. For $Ba(Zr_{0.11}Ti_{0.89})O_3$ only one phase transition ~349 K can be deduced from the dielectric measurements. This does not necessarily mean that there is only one phase transition, moreover the three consecutive phase transitions might be pinched together so that the single phase transitions cannot be resolved anymore experimentally. The $Ba(Zr_{0.13}Ti_{0.87})O_3$ composition exhibits the largest maximum dielectric permittivity with a paraelectric to ferroelectric phase transition at ~345 K. For the compositions with x=0.15-0.35 the peak in the dielectric permittivity consecutively broadens with increasing zirconium content and the maximum dielectric permittivity decreases.

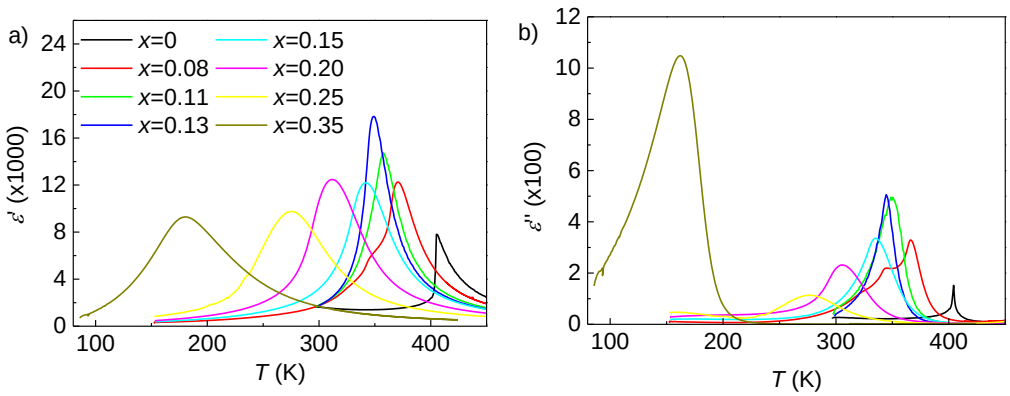

Fig. 3.2.3: a) real and b) imaginary part of dielectric permittivity of $Ba(Zr_xTi_{1-x})O_3$ compositions measured at an excitation frequency of 10 kHz.

From the dielectric permittivity curves depicted in Figure 3.2.3 it can be concluded that the $Ba(Zr_{0.13}Ti_{0.87})O_3$ composition displays the border from compositions with first order paraelectric to ferroelectric phase transition, i.e. $x<0.13$, towards compositions with second order paraelectric to ferroelectric phase transition. The second order phase transition character in the $Ba(Zr_{0.13}Ti_{0.87})O_3$ composition can be deduced from the large maximum dielectric permittivity and the twice as large slope in the dielectric permittivity below T_C compared to above T_C. This is in accordance to phenomenological theory. The dielectric permittivity at T_C should be infinitely large from phenomenological theory but this is never seen under experimental conditions. To further highlight the phase transition characteristics, the dielectric permittivity under heating and cooling is depicted in Figure 3.2.4.

For pure BT a jump in the dielectric permittivity is observed at T_C. Furthermore, the rather strong first order phase transition characteristic (note that the first order character is strong for a ferroelectric but it is still a weak first order phase transition) leads to a temperature hysteresis of ~3 K between the dielectric permittivity under heating and under cooling conditions. This temperature hysteresis is a strong indication for a first order phase transition and results from the phase coexistence range, where either the paraelectric phase is metastable or the ferroelectric phase is metastable. For the $Ba(Zr_{0.08}Ti_{0.92})O_3$ composition the first order phase transition at T_C is less pronounced than for BT but still a small temperature hysteresis of ~2 K in the dielectric permittivity is observed. The interferroelectric phase transition between the tetragonal and orthorhombic phase exhibits as well a temperature hysteresis in the dielectric permittivity. The interferroelectric phase transitions are always of a first order character, because the differing ferroelectric phases share no group-subgroup relationship. Differing from BT and $Ba(Zr_{0.08}Ti_{0.92})O_3$, the $Ba(Zr_{0.15}Ti_{0.85})O_3$ composition shows no jump in the dielectric permittivity at T_C and no temperature hysteresis. Moreover, the peak in the dielectric permittivity broadens compared to $Ba(Zr_{0.13}Ti_{0.87})O_3$ indicating an onset of diffusive phase transition character.

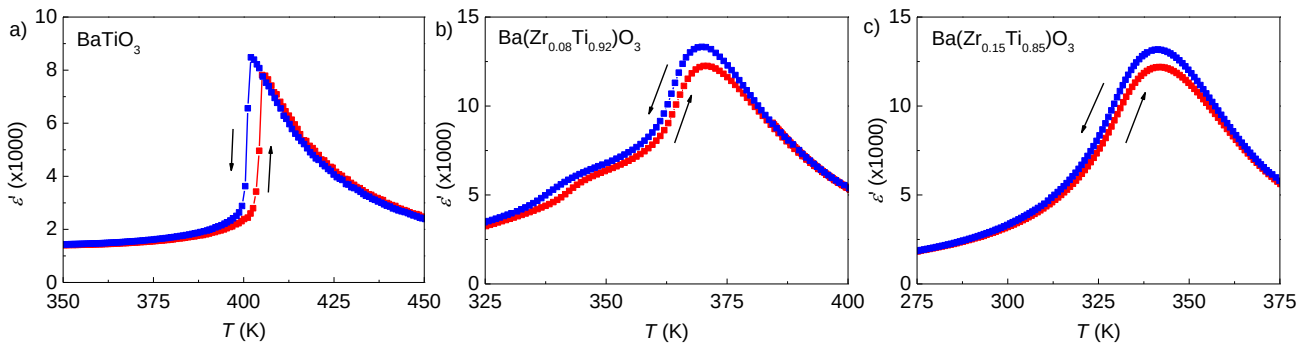

Fig. 3.2.4: Real part of the dielectric permittivity for $Ba(Zr_xTi_{1-x})O_3$ compositions under heating (red squares) and cooling (blue squares). The excitation frequency was 10 kHz. a) $BaTiO_3$, b) $Ba(Zr_{0.08}Ti_{0.92})O_3$ and c) $Ba(Zr_{0.15}Ti_{0.85})O_3$.

The diffusive character of the paraelectric to ferroelectric phase transition in $Ba(Zr_{0.15}Ti_{0.85})O_3$ is further pronounced for the compositions $Ba(Zr_{0.20}Ti_{0.80})O_3$ and $Ba(Zr_{0.25}Ti_{0.75})O_3$, depicted in Figure 3.2.5 a) and b), respectively. The dielectric permittivity for both compositions is shown as a function of the excitation frequency. No pronounced frequency dispersion is observed at the high temperature side of the maximum dielectric permittivity or the low temperature side. In other words, the dielectric permittivity behavior gives no indication of relaxor – like behavior. The relaxor – like behavior sets in at a larger zirconium content, i.e. $Ba(Zr_{0.35}Ti_{0.65})O_3$. The dielectric permittivity of $Ba(Zr_{0.35}Ti_{0.65})O_3$ measured over a broad range of excitation frequencies is displayed in Figure 3.2.5 c). The maximum in the dielectric permittivity constantly shifts towards lower temperatures with lower excitation frequency. This happens over a broad temperature range from ~215 K for a frequency of 10 MHz to ~165 K for a frequency of 10 mHz. The $Ba(Zr_{0.35}Ti_{0.65})O_3$ composition will be called relaxor – like, because crucial differences to classical relaxor materials, like PMN, exist (see section 1.3.5). It was demonstrated that dipolar glasses, which exhibit no electric field induced transition into a ferroelectric state, can show frequency dispersion of the dielectric permittivity similar to classical relaxor systems.[223]

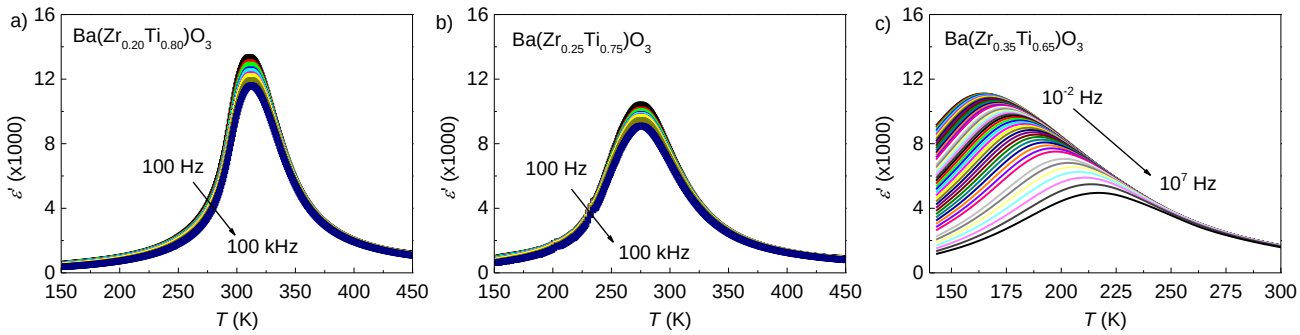

Fig. 3.2.5: Real part of the dielectric permittivity for a) $Ba(Zr_{0.20}Ti_{0.80})O_3$, b) $Ba(Zr_{0.25}Ti_{0.75})O_3$ and c) $Ba(Zr_{0.35}Ti_{0.65})O_3$ under heating conditions. Arrows indicate increasing excitation frequency.

The remanent polarization over temperature response and a Vogel-Fulcher type fitting of the dielectric response for the $Ba(Zr_{0.35}Ti_{0.65})O_3$ composition is shown in Figure 3.2.6. The remanent polarization gradually decreases with increasing temperature and vanishes around ~160 K. The highest loss in remanent polarization occurs between 100 K and 140 K. The ferroelectrically active clusters become thermally activated, which leads to a randomization of the dipolar vector in neighboring clusters and a vanishing macroscopic polarization. The Vogel-Fulcher temperature, which is often denoted as the freezing temperature, was determined as ~135.7 K. This is in good agreement with the measured behavior of remanent polarization. Note that the freezing temperature here does not necessarily denote a complete freezing, i.e. divergence of the relaxation time constant.[223]

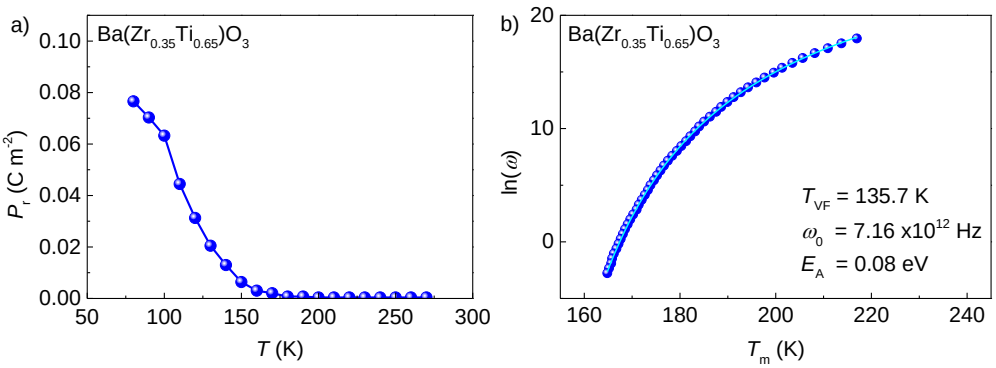

Fig. 3.2.6: a) Remanent polarization for $Ba(Zr_{0.35}Ti_{0.65})O_3$ deduced from bipolar polarization loops with a maximum amplitude of the electric field of 2 kV mm^{-1}. The polarization loops exhibited saturation and were recorded with increasing temperature after thermal annealing at 420 K. b) Vogel-Fulcher type fitting of the temperature of maximum dielectric permittivity versus the angular frequency of the excitation voltage. Frequencies used are the ones depicted in Figure 3.2.5 c).

From the dielectric permittivity measurements described, a temperature – composition phase diagram is constructed. For comparison the phase transition temperatures determined by Zhi et al. are included.[198] The phase transition temperatures determined in this work coincide well with the ones reported in literature.[73, 194, 201, 204, 209, 258] It can be summarized that x=0-0.08 exhibits first order paraelectric to ferroelectric phase transition, around x~0.13 a second order phase transition is observed. The exact composition where the first order character goes over into a second order character cannot be determined experimentally. It cannot be clarified, if this composition is the same as the composition where the paraelectric to ferroelectric and interferroelectric phase transitions merge together. With increasing zirconium content, i.e. x=0.15-0.25, the second order phase transition goes over into a diffusive phase transition. At x=0.35 relaxor – like behavior is observed, indicated by the frequency dispersion of the dielectric permittivity.

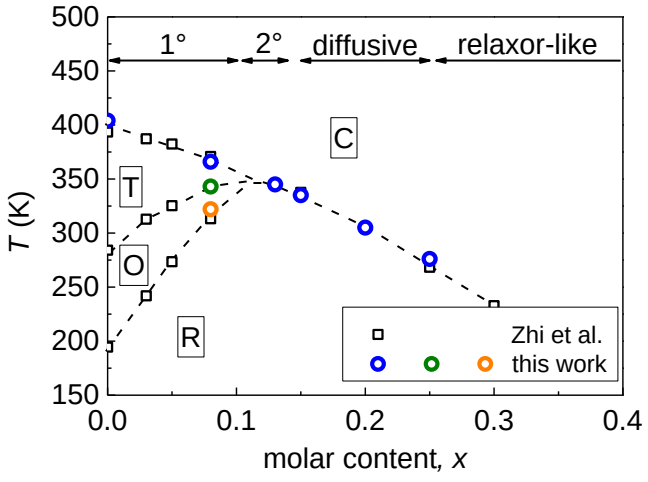

Fig. 3.2.7: Temperature – Composition phase diagram deduced from the phase transition temperatures obtained by dielectric permittivity measurements. For comparison the phase transition temperatures from Zhi et al. are included.[198] The ranges highlighted in the graph are derived from the dielectric permittivity behavior.

Crucial for electrocaloric materials in the application is their thermophysical behavior. In Figure 3.2.8 a) the specific heat capacity is depicted. It is observed that by increasing the zirconium content the specific heat capacity is slightly shifting to lower values. This is related to the lower heat capacity of BZ in comparison to BT.[154, 259] BT (black squares) exhibits a strong anomaly, in comparison to the other compositions. The T_C determined from the specific heat capacity, i.e. the jump in the specific heat capacity, coincides with the previous dielectric measurements. An extensive pretransitional specific heat capacity change can be seen. Note that the specific heat capacities depicted were measured by the ac calorimetry technique and hence do not include contributions from latent heat. The pretransitional anomaly of BT is a result of the consecutive entropy change in the tetragonal phase. With increasing temperature the c/a – ratio decreases leading to a decreasing spontaneous polarization and connected with that the change in the entropy. The anomaly at T_C for the $Ba(Zr_{0.08}Ti_{0.92})O_3$ composition is smaller compared to BT and no distinct jump in the specific heat capacity can be observed. This coincides with the dielectric response of $Ba(Zr_{0.08}Ti_{0.92})O_3$.

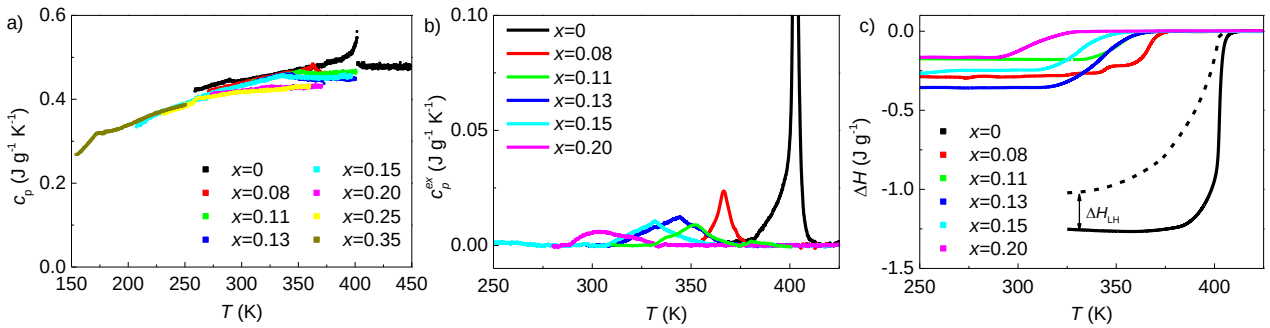

Fig. 3.2.8: a) Specific heat capacity of $Ba(Zr_xTi_{1-x})O_3$ compositions measured by ac calorimetry. Note that here the enthalpy change due to latent heat is not included. b) Excess specific heat capacity for selected $Ba(Zr_xTi_{1-x})O_3$ compositions measured by DSC. The excess specific heat capacity is determined by fitting the hard mode specific heat capacity with the Haas – Fisher approach[260] and subtracting it from the total specific heat capacity. The obtained excess specific heat capacity from DSC measurements for the compositions with second order character or diffusive phase transition coincide with the ac calorimetry measurements. c) Calculated enthalpy change for $Ba(Zr_xTi_{1-x})O_3$ compositions around the paraelectric to ferroelectric phase transition. Solid lines are derived from DSC measurements and the dashed line for BT is derived from ac calorimetry measurements. The difference in the overall enthalpy change for BT is related to the enthalpy change due to latent heat, which is included in DSC measurements but not in the ac calorimetry measurements.

With increasing zirconium content the specific heat capacity anomaly becomes smaller and broader. To highlight the anomaly, the excess specific heat capacity is depicted in Figure 3.2.8 b). The hard mode specific heat capacity was fitted by a Haas – Fisher approach and then subtracted from the measurement data to obtain the excess specific heat capacity.[260] The data in Figure 3.2.8 b) is deduced from DSC measurements. The excess specific heat capacity obtained from ac calorimetry measurements is the same except for BT. It can be expected that the latent heat of the phase transition in $Ba(Zr_{0.08}Ti_{0.92})O_3$ gives a differing behavior for both techniques but within the errors of the fitting procedure no difference was

found. This reflects the small latent heat at the paraelectric to ferroelectric phase transition for this composition. The temperatures of the excess specific heat capacity anomalies coincide with the phase transition temperatures determined from dielectric measurements. For $Ba(Zr_{0.11}Ti_{0.89})O_3$, $Ba(Zr_{0.13}Ti_{0.87})O_3$ and $Ba(Zr_{0.15}Ti_{0.85})O_3$ the peak values of the excess specific heat capacity are similar. For $Ba(Zr_{0.20}Ti_{0.80})O_3$ the excess specific heat capacity is smaller and $Ba(Zr_{0.35}Ti_{0.65})O_3$ does not exhibit any anomaly in this temperature range. The enthalpy change for the compositions is shown in Figure 3.2.8 c). The enthalpy change is obtained by integration of the excess specific heat capacity, where the high temperature paraelectric phase is set to zero. For BT the difference in the two measurement techniques can be clearly seen. The latent heat included in the DSC measurements lead to a different enthalpy change. By comparison of both curves for BT the latent heat can be determined to $\Delta H_{LH} \sim 0.25\ \mathrm{J\ g^{-1}}$. From the latent heat, the spontaneous polarization is determined as $P_s = 0.1 - 0.16\ \mathrm{C\ m^2}$. After BT the $Ba(Zr_{0.13}Ti_{0.87})O_3$ composition exhibits the largest enthalpy change between the paraelectric and ferroelectric phase.

Until now the anomaly in the specific heat capacity of $Ba(Zr_{0.35}Ti_{0.65})O_3$ was not discussed. In previous reports disagreement is found if an anomaly exists in relaxor – like $Ba(Zr_xTi_{1-x})O_3$ compositions.[261, 262] Nagasawa et al. compared $Ba(Zr_{0.35}Ti_{0.65})O_3$ with PMN and found no anomaly in the specific heat capacity of $Ba(Zr_{0.35}Ti_{0.65})O_3$.[262] This was explained by the order – disorder mechanism in the formation of PNRs in the case of PMN and the displacive mechanism in the case of $Ba(Zr_{0.35}Ti_{0.65})O_3$. On the other hand, Gorev et al. found an anomaly in the specific heat capacity between 150 K – 200 K.[261] They demonstrated that such an anomaly in the specific heat capacity is in accordance to the spherical random bond – random field model.[263] The measurements performed in this work clearly demonstrate that $Ba(Zr_{0.35}Ti_{0.65})O_3$ exhibits an anomaly between 150 K – 200 K in agreement with the measurements performed by Gorev et al., see Figure 3.2.9. The peak of the anomaly in the dielectric permittivity coincides with the excess specific heat capacity peak.

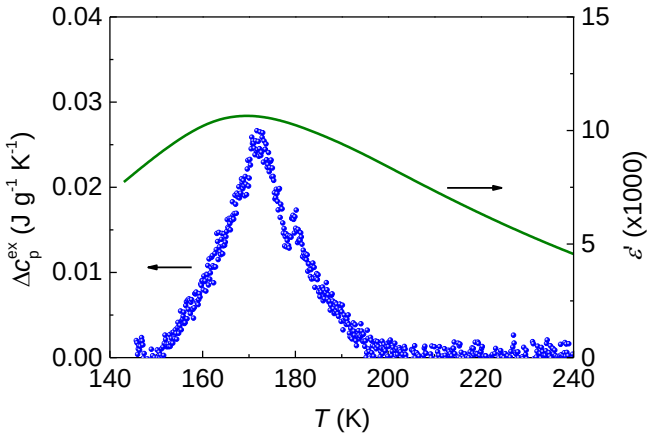

Fig. 3.2.9: Excess specific heat capacity and real part of the dielectric permittivity of $Ba(Zr_{0.35}Ti_{0.65})O_3$. The excitation frequency of the dielectric permittivity measurement was ~1 Hz.

Equation 3.2.13 indicates that the thermal conductivity is an important parameter for EC materials. Furthermore, it was demonstrated that the thermal conductivity behavior is different for classical ferroelectrics compared to ferroelectrics exhibiting relaxor – like behavior.[147, 148] In Figure 3.2.10 the low temperature thermal conductivity for selected $Ba(Zr_xTi_{1-x})O_3$ compositions is depicted. BT exhibits a classical behavior for crystalline materials with a peak around ~50 K. This peak is associated with the change in the dominant scattering mechanism. At large temperatures the thermal conductivity is limited by the mean free path for thermal phonons. The dominant scattering process is the intrinsic phonon – phonon interaction.[250] At lower temperatures, i.e. below the peak in thermal conductivity, scattering by defects and impurities becomes dominant.[250] The sample size can be another limiting factor for the mean free path of thermal phonons. Nevertheless, this usually occurs at the lowest temperatures, i.e. $T<1$ K.[250] The anomaly around ~200 K in the thermal conductivity can be attributed to the rhombohedral to orthorhombic phase transition in BT. The influence of the interferroelectric phase transition on the thermal conductivity was related to the transverse optic modes responsible for the ferroelectricity.[145] Around the phase transition those phonon branches have energies similar to the energy of the heat carrying acoustic phonons. The increase in phonon scattering events leads to a decrease in the thermal conductivity.

By increasing the zirconium content the peak in the thermal conductivity gets suppressed. For the compositions $Ba(Zr_{0.08}Ti_{0.92})O_3$ and $Ba(Zr_{0.11}Ti_{0.89})O_3$ a small peak is found around ~60 K. Whereas, for $Ba(Zr_{0.25}Ti_{0.75})O_3$ and $Ba(Zr_{0.35}Ti_{0.65})O_3$ the peak vanished. The behavior of those compositions is similar to what is found in glasses.[148] The behavior of thermal conductivity gradually changes from that of crystalline materials to a glasslike behavior. A similar transition can be found in partially crystallized glasses and polymers, which have submicrometer – sized crystalline regions dispersed in an amorphous matrix.[264-266] The behavior of thermal conductivity was explained by the elastic mismatch between crystalline and amorphous regions, which leads to a boundary resistance. Hence, with increasing zirconium content, the boundary resistance between titanium rich regions and zirconium rich regions might lead to the glasslike behavior in $Ba(Zr_xTi_{1-x})O_3$ compositions with $x>0.25$. From the results of this work it can be concluded that classical ferroelectrics and relaxor – like ferroelectrics behave very different in the evolution of the thermal conductivity. The thermal conductivity of relaxor – like ferroelectrics is lower than for classical ferroelectrics, which is detrimental to the material related cooling power.

More important for EC applications is the thermal conductivity at elevated temperatures, where the paraelectric to ferroelectric phase transition occurs. The high temperature thermal conductivity for $Ba(Zr_xTi_{1-x})O_3$ compositions is shown in Figure 3.2.10 b). The BT ceramic sample shows similar values for the thermal conductivity like the BT single crystal with [001] cut depicted in Figure 3.1.2 d). This demonstrates that the grain boundaries have diminishing influence on the overall thermal conductivity

in large grained ceramics. An influence from grain boundaries is expected for submicrometer grained ceramics, where the grain size and the smaller domain size approach the mean free path of thermal phonons.[141, 142] With increasing the zirconium content the thermal conductivity gradually decreases. The $Ba(Zr_xTi_{1-x})O_3$ compositions with x=0.08 – 0.35 show a nearly linear increase in the thermal conductivity between 300 K and 500 K. No anomaly can be observed, even though compositions with x=0.08 – 0.15 exhibit a paraelectric to ferroelectric phase transition in this temperature range. It should be noted that the phase transition range for those compositions is broader than for BT and an anomaly might be not observable in the depicted measurements. The gradual decrease in thermal conductivity with increasing zirconium content is shown in Figure 3.2.10 c). The temperature at which the thermal conductivities were extracted is 460 K and therefore in the cubic phase for all compositions. A similar decrease in thermal conductivity of around ~35 % from BT to $Ba(Zr_{0.35}Ti_{0.65})O_3$ was observed in PZT, by increasing the zirconium content from pure PT to $Pb(Zr_{0.50}Ti_{0.50})O_3$.[140]

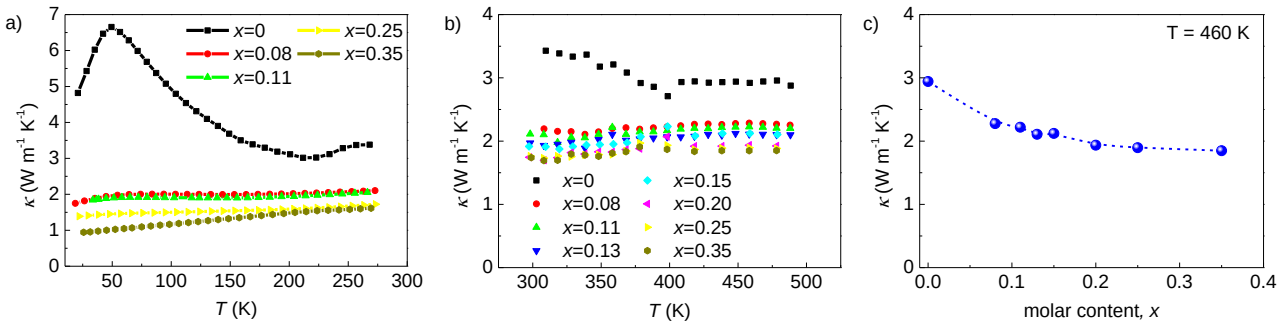

Fig. 3.2.10: Thermal conductivity of $Ba(Zr_xTi_{1-x})O_3$ compositions measured by a) a quasi – steady – state method at low temperatures and b) a transient method at elevated temperatures. c) Thermal conductivity as function of $Ba(Zr_xTi_{1-x})O_3$ composition at 460 K.

After discussing the different phase transition characteristics and thermophysical properties of the $Ba(Zr_xTi_{1-x})O_3$ compositions, the directly measured electrocaloric temperature changes are displayed in Figure 3.2.11. For $Ba(Zr_{0.08}Ti_{0.92})O_3$ the largest EC temperature change is observed at the paraelectric to ferroelectric phase transition at 365 K. The first order phase transition leads to a jump in the EC temperature change, i.e. between the measurement temperature of 365 K and 370 K, observed for electric field changes between 5 kV mm^{-1} and 20 kV mm^{-1}. The jump of around ~0.04 K is the same for all electric field changes and is therefore related to the latent heat of the paraelectric to ferroelectric phase transition. Nevertheless, the latent heat and therefore the related temperature change is small compared to BT, where the latent heat leads to temperature changes of around ~1 K.[116] The diminishing small latent heat was already assumed from the analysis of the excess specific heat capacity and the comparison of data from DSC measurements and ac calorimetry measurements.[‡‡] For the

[‡‡] A temperature change of ~0.04 K corresponds to a latent heat of ΔH_{LH}~0.018 J g^{-1}.

interferroelectric phase transitions no jumps in the EC temperature change from latent heat are observable. The latent heat from the interferroelectric phase transitions are even smaller than from the paraelectric to ferroelectric phase transition. A small influence of the interferroelectric phase transitions might be visible by the shoulder in the EC temperature change between 320 K and 360 K. For $Ba(Zr_{0.13}Ti_{0.87})O_3$ a nearly symmetric thermal evolution of the EC temperature change is found around the peak at 350 K. Such a behavior is in accordance to the phenomenological theory.[18, 110] By increasing the zirconium content to x=0.15, x=0.20 and x=0.25, a similar behavior like in $Ba(Zr_{0.11}Ti_{0.89})O_3$ is observed. A maximum in the EC response is found at the phase transition temperature. The peak in the EC temperature change broadens with an increase in zirconium content, going from a second order phase transition to diffusive phase transition behavior. $Ba(Zr_{0.35}Ti_{0.65})O_3$ exhibits a broad maximum in the EC temperature change at ~200 K, for all electric field changes. This is contrary to relaxor ferroelectrics, where the maximum in the EC temperature change shifts to higher temperatures with increasing the electric field change. The origin of this difference is the field induced phase transition into a ferroelectric phase for relaxor, whereas this is not possible in dipolar glasses.[110]

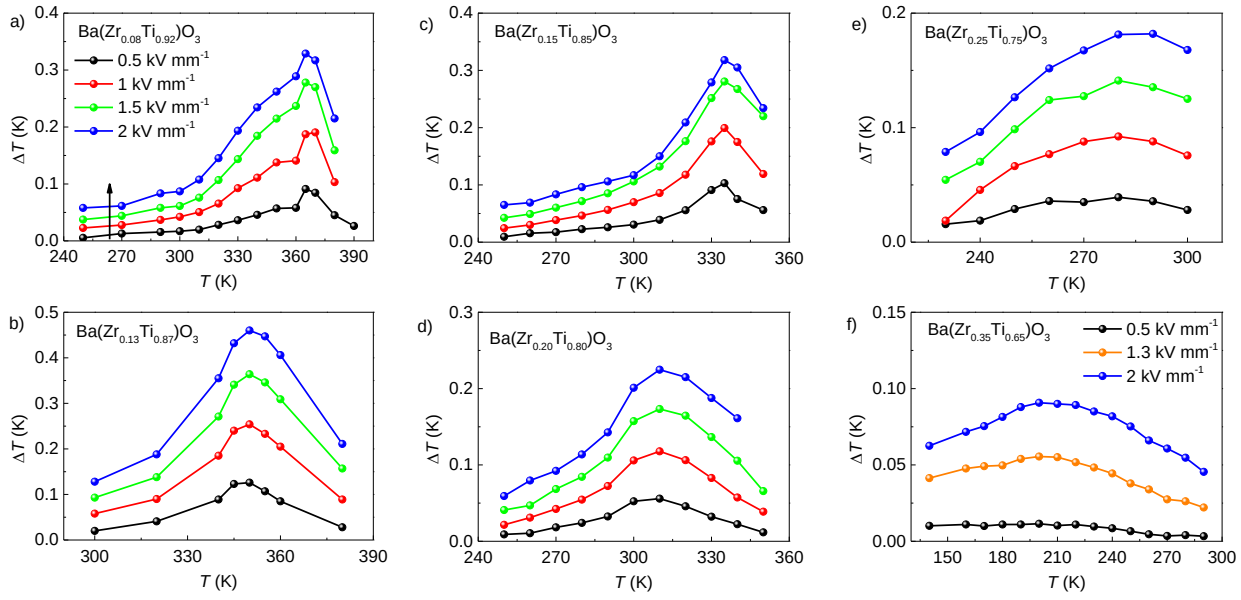

Fig. 3.2.11: Directly measured electrocaloric temperature change for a) $Ba(Zr_{0.08}Ti_{0.92})O_3$, b) $Ba(Zr_{0.13}Ti_{0.87})O_3$, c) $Ba(Zr_{0.15}Ti_{0.85})O_3$, d) $Ba(Zr_{0.20}Ti_{0.80})O_3$, e) $Ba(Zr_{0.25}Ti_{0.75})O_3$ and f) $Ba(Zr_{0.35}Ti_{0.65})O_3$.

To better compare the EC response of the $Ba(Zr_xTi_{1-x})O_3$ compositions, the EC temperature changes at an electric field change of 2 kV mm^{-1} are depicted in Figure 3.2.12 a). The largest EC response is found for $Ba(Zr_{0.13}Ti_{0.87})O_3$. $Ba(Zr_{0.08}Ti_{0.92})O_3$ and $Ba(Zr_{0.15}Ti_{0.85})O_3$ exhibit similar maximum EC responses at the respective phase transition temperature. With increasing the zirconium content x>0.15 the maximum EC response gradually decreases. From the equations for the EC temperature change derived from the Maxwell relations and phenomenological theory, i.e. Equation 1.3.6 and Equation 1.3.16, it

can be seen that the EC temperature change depends on the temperature, density and specific heat capacity at the respective measurement temperature. To exclude the influence of the lower measurement temperature for increasing zirconium content, the isothermal entropy change is calculated from the directly measured EC temperature changes.

$$\Delta S = \frac{c_p}{T} \cdot \Delta T. \tag{3.2.1}$$

The isothermal entropy change for the $Ba(Zr_xTi_{1-x})O_3$ compositions is depicted in Figure 3.2.12 b). Furthermore, the isothermal entropy change of the $Ba(Zr_xTi_{1-x})O_3$ compositions was corrected for the larger amount of non-ferroelectrically active BZ compared to the ferroelectrically active BT, shown in Figure 3.2.12 c).

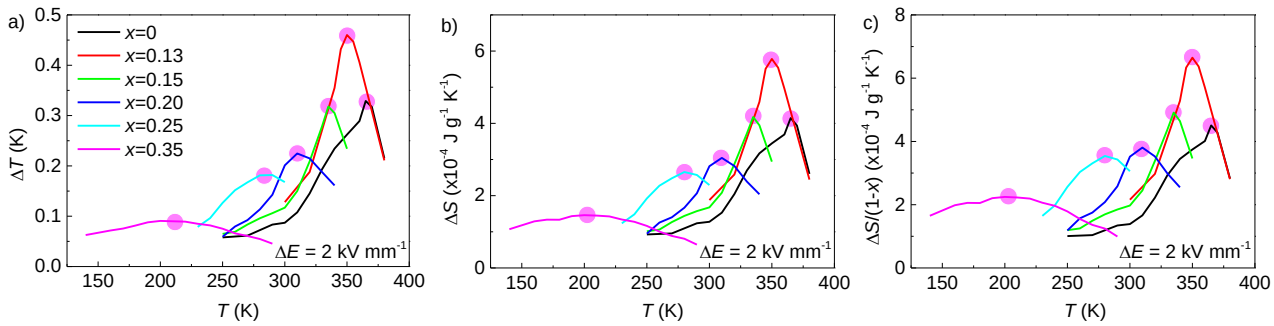

Fig. 3.2.12: a) Directly measured electrocaloric temperature change under an electric field change of 2 kV mm^{-1} for $Ba(Zr_xTi_{1-x})O_3$ compositions. b) Isothermal entropy change of $Ba(Zr_xTi_{1-x})O_3$ compositions, calculated from the directly measured electrocaloric temperature change. c) Isothermal entropy change of $Ba(Zr_xTi_{1-x})O_3$ compositions divided by the fraction of ferroelectrically active titanium ions. The pink dots highlight the maximum point for the respective quantity.

The respective maximum values (highlighted by pink dots) are compared in table 3.2.1.

Table 3.2.1: Comparison of maximum values of EC temperature change, isothermal entropy change and composition corrected isothermal entropy change for $Ba(Zr_xTi_{1-x})O_3$ compositions.

Molar content, x	$\Delta T_x / \Delta T_{0.13}$	$\Delta S_x / \Delta S_{0.13}$	$(\frac{\Delta S_x}{1-x}) / (\frac{\Delta S_{0.13}}{1-0.13})$
0.08	0.71	0.71	0.68
0.13	1	1	1
0.15	0.68	0.72	0.74
0.20	0.49	0.53	0.57
0.25	0.40	0.46	0.53
0.35	0.19	0.25	0.34

The general trend between the ratios of the EC temperature change is kept for the comparison of isothermal entropy change and composition corrected entropy change. Important is that the difference

in the EC temperature change between the $Ba(Zr_xTi_{1-x})O_3$ compositions is neither a result of the different phase transition temperatures nor the decreasing amount of ferroelectrically active BT. In fact, the origin of the differences is the differing phase transition characteristic.

A caloric figure of merit (W), derived from the material related cooling power, is used to compare the $Ba(Zr_xTi_{1-x})O_3$ compositions, depicted in Figure 3.2.13. The caloric figure of merit is defined by the material properties influencing the material related cooling power, according to Equation 3.1.13 as:

$$W = \sqrt{\kappa} \cdot \sqrt{\rho c_p} \cdot \Delta T. \tag{3.2.2}$$

The same trends like in Figure 3.2.12 a) are observed. The decreasing thermal conductivity and specific heat capacity for increasing zirconium content are reflected in the caloric figure of merit, but the influence is small. A much larger influence of the thermophysical properties is expected if different material systems are compared. The comparison based on the caloric figure of merit is not restricted solely to the electrocaloric effect. The caloric figure of merit can be calculated as well for other caloric effects, i.e. mechanocaloric effect and magnetocaloric effect. A comparison of the three caloric effects is provided from literature data on the caloric temperature changes and thermophysical properties for representative materials.

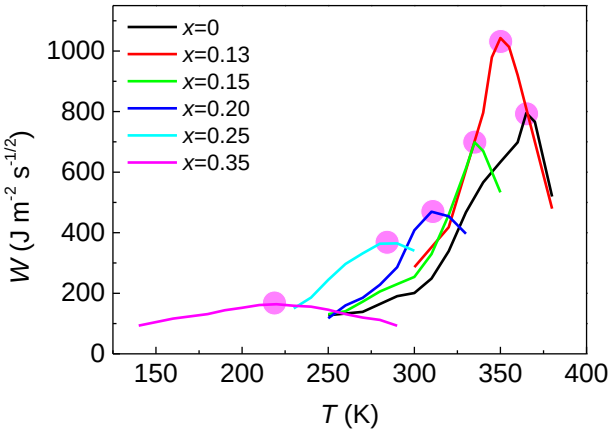

Fig. 3.2.13: The caloric figure of merit W for $Ba(Zr_xTi_{1-x})O_3$ compositions. The pink dots highlight the maximum points.

In Figure 3.2.14 the caloric figure of merit is displayed for NiTi[267, 268], Gd[269, 270], $Ni_{0.50}Mn_{0.337}In_{0.163}$[271, 272], $La(Fe,Co,Si)_{13}$[273, 274], $Ba(Zr_xTi_{1-x})O_3$, $Pb(Sc_{1/2}Ta_{1/2})O_3$[275] and $0.9Pb(Mg_{1/3}Nb_{2/3}O_3\text{-}0.1PbTiO_3$[151, 276]. The largest W is found for the mechanocaloric effect in NiTi. Here, the mechanically induced phase transition between a martensitic and an austenitic phase leads to large temperature changes of around ~15 K, accompanied by large thermal conductivity ~10 W m^{-1} K^{-1} due to the metallic character with electronic thermal conductivity. This makes NiTi from the standpoint of the caloric figure of merit an attractive material. The lead-based EC materials in Figure 3.2.14 can compete with the magnetocaloric

materials. To use the EC materials in devices, multilayer structures with large electric breakdown field must be developed as the key to achieve substantial EC temperature changes is the application of large electric fields. The specific application of caloric cooling is of importance in the decision which caloric effect is the most suitable. For large scale coolers, like household refrigerators or air conditioners, the mechanocaloric effect with its large caloric figure of merit might be preferential. For small scale coolers or non-stationary coolers the electrocaloric effect might be attractive as the integration into electronic circuits is facile.

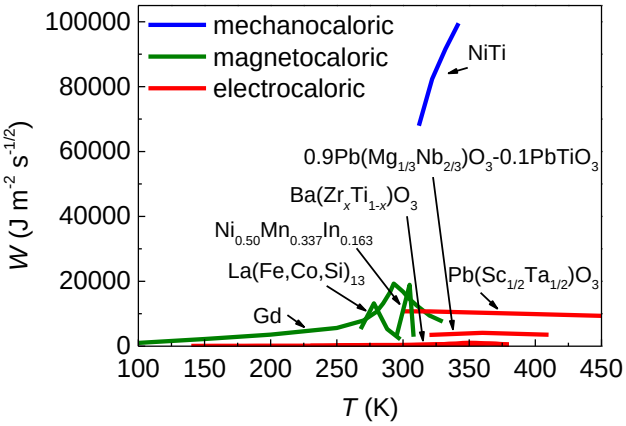

Fig. 3.2.14: The caloric figure of merit *W* for selected materials of the three caloric effects, i.e. mechanocaloric effect, magnetocaloric effect and electrocaloric effect.

From the results provided it can be seen that the caloric figure of merit *W*, which was introduced in this work, is useful in comparing EC materials and furthermore caloric effects with each other. It was found that the second order phase transition characteristic leads to an enhanced EC response and that the focus for material development should be set on this type of ferroelectrics. Nevertheless, it is necessary to define the working parameters of a specific application to select the most suitable material. Therefore, graphs comparing materials on basis of the caloric figure of merit provide guidance in the material selection.

3.3. The Phenomenological Theory of the Electrocaloric Effect in the $Ba(Zr_xTi_{1-x})O_3$ System

In studying ferroelectric materials, the classical Ginzburg-Landau-Devonshire theory of weak first order phase transitions has been extensively used. To reproduce the behavior of a specific ferroelectric material, experimental data is required to determine the parameters in the phenomenological theory. Such parametrization was conducted for BT in the early work of Devonshire[98, 99] and later on by others[277-281] in order to reproduce the experimental data. With different parameters the experimental observations could be reproduced with varying degree of agreement. For example, Perez Moyet extracted a set of parameters for BT in his work and compared it with parameters developed by others.[282] He could reproduce the curvature in P(T) approaching the paraelectric phase transition, which was not observed using parameters earlier developed. This demonstrates the importance of the set of parameters used to reproduce experimental data. Furthermore, as there are several sets of parameters for BT, parameters for solid solutions and compounds are sparely reported. In solid solutions the dependence of the parameters on the composition must be included, complicating the extraction of accurate parameters.[283, 284]

Here, we used parameters for barium zirconate titanate from Khakpash & Rossetti.[285] First the phenomenological theory is applied to BT to demonstrate the applicability of the parameters. The free energy is calculated to obtain the phase transition temperatures and zero electric field and electric field dependent polarization are highlighted. The calculation focused on the temperature range of ferroelectric to paraelectric phase transition and the electric field – temperature phase diagram is calculated. Calculation of the electrocaloric temperature change is provided with good agreement to literature. We further demonstrate, that the temperature change at T_C is mainly a result of the latent heat of the electric field induced paraelectric to ferroelectric phase transition. By subtracting the effect of the latent heat we demonstrate that the largest ECE is obtained at the temperature of the critical end point. The focus is then pointed towards the barium zirconate titanate system and the adequate reproduction of the composition – phase diagram by the used parameters. Furthermore, the composition exhibiting a tricritical point and the one exhibiting a triple point are determined. By calculating the critical end points for compositions with a zero electric field first order phase transition, a composition – temperature – electric field phase diagram was obtained for the first time. The EC temperature changes are calculated over the compositional and temperature space. The calculations conducted give further insight into the ECE of solid solutions and demonstrate that with suitable parameters the behavior of ferroelectric materials can be accurately determined. This section is based on unpublished results.

The $m\bar{3}m$ point symmetry of the cubic perovskite allows for the transformation into seven possible ferroelectric phases, i.e. one tetragonal, one orthorhombic, one rhombohedral, three monoclinic and one triclinic. Here, we restrict the calculations to the tetragonal (4mm), orthorhombic (3m) and

rhombohedral (mm2) phases, allowing the treatment with a 2-4-6 Landau polynomial. The used Landau polynomial (for a stress free ferroelectric) differs from the common Devonshire expression and explicitly separates the isotropic ($G_{1,\mathrm{iso}}$) and anisotropic ($G_{1,an\mathrm{iso}}$) contributions to the free energy.[286-288]

$$G_1 = G_{1,\mathrm{iso}} + G_{1,an\mathrm{iso}}. \tag{3.3.1}$$

The isotropic part of the free energy describes a polarized state with a polarization modulus larger than zero with no preferential polarization direction.

$$G_{1,\mathrm{iso}} = \frac{1}{2}A_1P^2 + \frac{1}{4}B_1P^4 + \frac{1}{6}C_1P^6. \tag{3.3.2}$$

The anisotropic part of the free energy determines the dependence of the free energy on the direction of the polarization vector.

$$G_{1,an\mathrm{iso}} = \frac{1}{4}[B_2(P_1^4 + P_2^4 + P_3^4)] + \frac{1}{6}[C_2(P_1^6 + P_2^6 + P_3^6) + C_3(P_1^2P_2^2P_3^2)]. \tag{3.3.3}$$

For the tetragonal (T), orthorhombic (O) and rhombohedral (R) phase the polarization vector is oriented along the <001>, <110> and <111> directions of the cubic prototype phase, respectively. To study the ECE, the electric field dependence of the polarization must be included in Equation 3.3.1 (Note that the electric field was always applied along the spontaneous polarization direction of the respective ferroelectric phase). The final free energy function is:

$$G_1 = \frac{1}{2}A_1P^2 + \frac{1}{4}B_1P^4 + \frac{1}{6}C_1P^6 + \frac{1}{4}[B_2(P_1^4 + P_2^4 + P_3^4)] + \frac{1}{6}[C_2(P_1^6 + P_2^6 + P_3^6) + C_3(P_1^2P_2^2P_3^2)] - E_1P_1 - E_2P_2 - E_3P_3 \tag{3.3.4}$$

The temperature dependent stable phases for BT can be seen in Figure 3.3.1 a). Reducing the temperature from the high temperature cubic phase, the free energy of the tetragonal phase becomes lower than the cubic phase at T_C=403.2 K. By lowering the temperature further the interferroelectric phase transition temperatures into the orthorhombic and rhombohedral phases are found. These calculated phase transition temperatures coincide well with literature data and measurements in this work.[90] In Figure 3.3.1 b) the spontaneous polarization of BT as a function of temperature is highlighted. In the cubic phase no spontaneous polarization develops and a jump in the polarization is found at T_C. The spontaneous polarization is ~0.19 C m^{-2} in agreement with calculations by Bell.[278] For BT the defect chemistry is very important for the value of the spontaneous polarization and it was demonstrated that by slight off-stoichiometry the spontaneous polarization can change.[170] The largest ECE is expected around T_C, where the largest changes in polarization with temperature occur. This temperature region slightly above T_C is of special importance in the case of BT. It is possible to induce a phase transition from the cubic phase to the tetragonal phase by the application of a large enough electric

field.[116, 278, 289] The electric field induced phase transition is of the first order, but the first order character gradually decreases and vanishes at the critical end point which is of the second order.[94, 116] This is seen in Figure 3.3.1 c) and d).

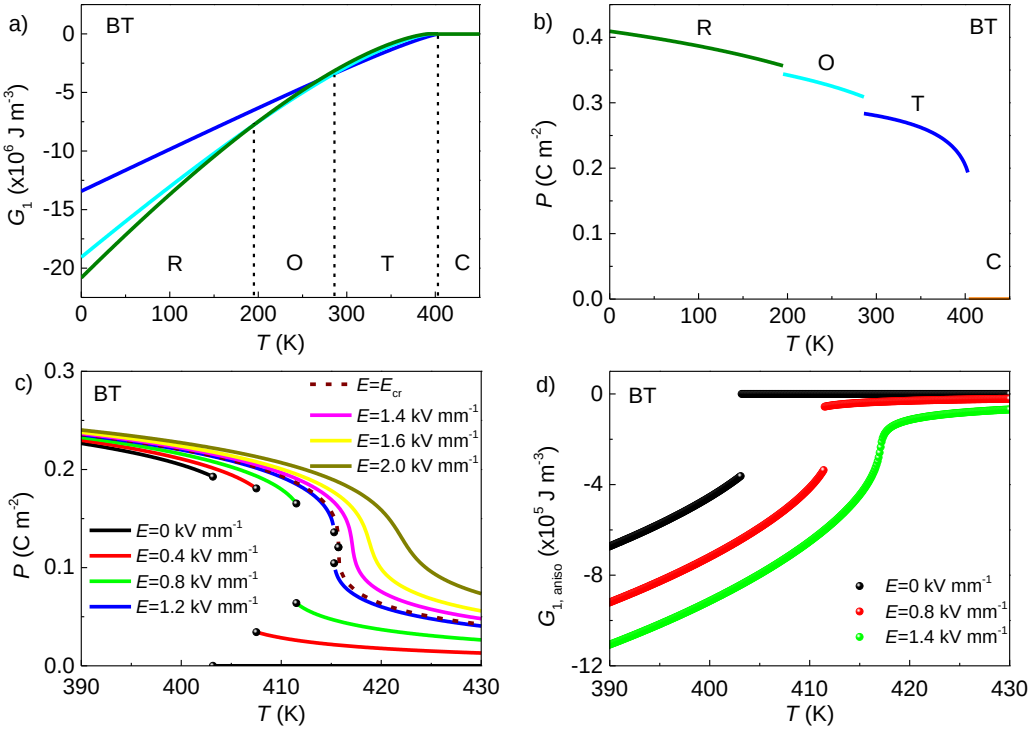

Fig. 3.3.1: a) Free energy of ferroelectric and paraelectric phases of BT as function of temperature. b) Spontaneous polarization of BT in the ferroelectric phases as a function of temperature. c) Polarization of BT as a function of temperature around the paraelectric to ferroelectric phase transitions for several electric field values. The critical electric field is denoted as E_{cr}. d) Anisotropic free energy of BT for several electric field values.

With increasing the electric field, the phase transition temperature shifts to higher temperatures and the jump in the polarization becomes smaller. At a critical field (E_{cr}) the temperature dependence of the polarization becomes continuous and the phase transition changes to the second order. The same is observed for the anisotropic free energy, which depends on the direction of the polarization. Above E_{cr} the temperature dependence of the polarization and anisotropic free energy is continuous and supercritical behavior was deduced from specific heat capacity and dielectric measurements.[116, 121]

To further elucidate the electric field induced paraelectric to ferroelectric phase transition, the electric field – temperature phase diagram is calculated and the free energy over polarization for three selected temperatures is shown in Figure 3.3.2.

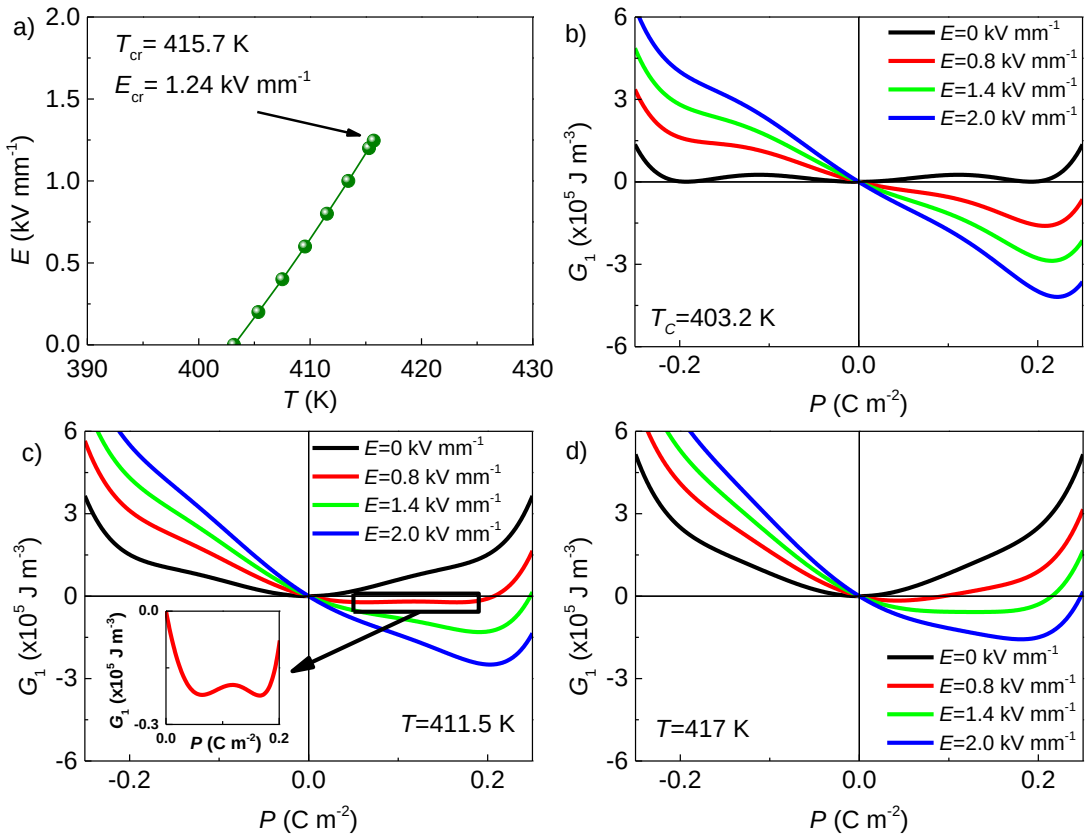

Fig. 3.3.2: a) Electric field – temperature phase diagram of BT with the critical end point. Free energy as function of polarization at selected electric fields at b) 403.2 K, c) 411.5 K and d) 417 K.

The phase transition temperatures are obtained from the free energy with applied electric field and the critical end point is calculated from the necessary conditions of the critical end point, i.e. $(\partial E/\partial P)_T = 0$ and $(\partial^2 E/\partial P^2)_T = 0$.[113] It follows for the critical electric field and critical temperature (T_{cr}):

$$E_{cr} = \left(\frac{24}{25}\right)\sqrt{\frac{3}{5}}\left(\frac{2}{B_1+B_2}\right)^{-\frac{5}{2}}(C_1+C_2)^{-\frac{3}{2}}, \tag{3.3.5}$$

$$T_{cr} = T_0 + \frac{9}{20}\frac{(B_1+B_2)^2}{A_0(C_1+C_2)}. \tag{3.3.6}$$

Note that here A_0 results from the temperature dependent coefficient $A_1 = A_0(T - T_0)$. The critical parameters for BT are calculated as T_{cr}=415.7 K and E_{cr}=1.24 kV mm^{-1}. These values are in agreement with measurements on a [001] single crystal.[116] The line of first order phase transitions in BT is nearly linear and terminates at the critical end point. It is found that over a range of 12.5 K, i.e. between T_C and T_{cr}, a first order phase transition can be induced by a sufficiently large electric field. In Figure 3.3.2 b) the free energy over polarization at T_C is depicted. At zero electric field the free energy of the paraelectric phase, i.e. at P=0, is equal to the free energy of the ferroelectric phase, i.e. at $P=\pm P_S$. By increasing the electric field, the ferroelectric phase becomes the only stable phase with a polarization in

the direction of the electric field. At zero electric field an energy barrier separates the polarization in the paraelectric and ferroelectric phase. At 411.5 K, i.e. between T_C and T_{cr}, the only stable phase at zero electric field is the paraelectric phase with a polarization at P=0. By increasing the electric field, the free energy of the ferroelectric phase gets lowered. At an electric field E=0.8 kV mm^{-1} the free energy of the paraelectric and ferroelectric (in the direction of the electric field) phase are equal. Here, an energy barrier between the both phases is observed, demonstrating the first order character of the phase transition. At larger electric fields the ferroelectric phase in the direction of the electric field gets stabilized. At 417 K the paraelectric phase is stable. This is now at a temperature above T_{cr} and no first order phase transition is expected. The minimum in the free energy moves in the direction of the applied electric field without the appearance of an energy barrier, indicating the supercritical behavior. Nevertheless, a substantial polarization can be induced in the direction of the electric field.

The electric field induced first order phase transition leads to a latent heat that is released during the phase transition from the paraelectric to ferroelectric phase, i.e. by electric field increase, and absorbed during the phase transition from the ferroelectric phase to the paraelectric phase, i.e. by electric field decrease. If the released or absorbed latent heat is not exchanged with the environment, it leads to a temperature increase or decrease of the material. The latent heat can be calculated by the Clausius – Clapeyron equation,

$$\Delta S_L = \Delta P(E_t(T))\left(\frac{dE_t}{dT}\right), \tag{3.3.7}$$

and Equation 1.3.17 and 1.3.18. In Equation 3.3.7 E_t denotes the transition field at which the free energy of the paraelectric and ferroelectric phase are equal. The latent heat and the resultant temperature change is depicted in Figure 3.3.3 a). The latent heat gradually decreases with increasing temperature and vanishes at the critical temperature. The temperature change due to the latent heat is large with a maximum value of ~2 K at T_C.

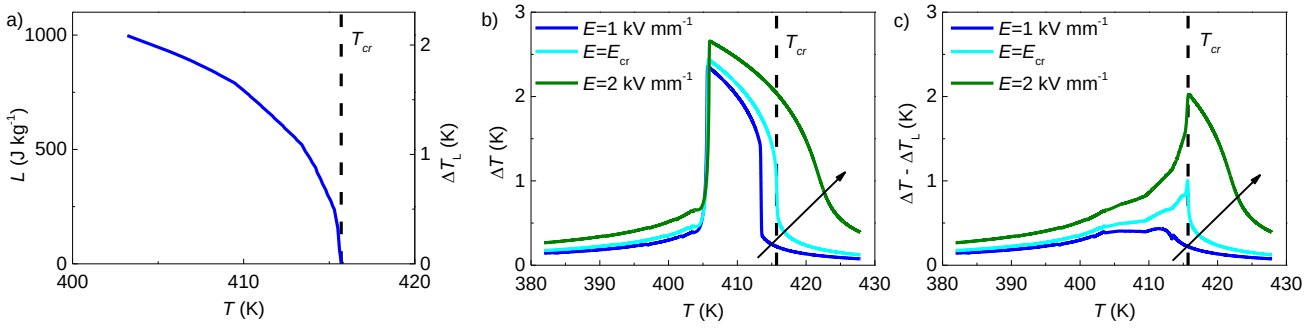

Fig. 3.3.3: a) Latent heat and corresponding temperature change as a function of temperature. b) EC temperature change under an electric field change from the maximum electric field indicated in the legend to zero electric field. c) EC temperature change subtracted by the contribution from the latent heat.

From the electric field dependent polarization as function of temperature curves the EC temperature change can be calculated using a phenomenological approach, i.e. by Equation 1.3.16. Here, iterations were performed to calculate the cooling temperature change, i.e. starting from the polarization at applied electric field. The temperature change of BT is depicted in Figure 3.3.3 b) at three starting electric fields. The final electric field was always zero. With increasing the temperature, the EC temperature change gradually increases and a large jump in the EC temperature change is observed slightly above T_C.[§§] Here, the latent heat contribution due to the tetragonal to cubic phase transition is the largest. With the decrease in latent heat for increasing temperature, the EC temperature change gradually decreases. For an electric field of E=1 kV mm^{-1}, i.e. below E_{cr}, a second jump in the EC temperature change is observed at around ~413 K. At this temperature the electric field is not strong enough to induce the tetragonal phase, and hence the contribution from the latent heat is absent. For the electric fields E=E_{cr} and E=2 kV mm^{-1} a continuous decrease in the EC temperature change is observed.

In Figure 3.3.3 c) the pure ECE, i.e. the temperature change due to the phase transition is subtracted from the total temperature change, is depicted. Now for the electric field E=E_{cr}, the maximum in the temperature change is found at T_{cr}. This demonstrates that the ECE at the critical end point is the largest. Of course the EC temperature change scales with the electric field change and therefore at an electric field of E=2 kV mm^{-1} the temperature change is larger than for E=E_{cr}. Nevertheless, also at this electric field the maximum in the temperature change is observed at T_{cr}. For electric fields below E_{cr} the critical end point cannot be reached and therefore no maximum temperature change is observed at T_{cr}. The results demonstrate the importance of the critical end point in maximization of properties. For BT this was shown with respect to piezoelectric properties and for relaxor ferroelectrics with respect to piezoelectric properties, electrocaloric properties and energy storage performance.[115, 121, 289-291]

Now the focus is set towards the $Ba(Zr_xTi_{1-x})O_3$ system. To demonstrate the suitability of the used parameters for the $Ba(Zr_xTi_{1-x})O_3$ system, the composition – temperature – free energy phase diagram and the composition and temperature dependent spontaneous polarization in the different ferroelectric phases is depicted in Figure 3.3.4. From the free energy in Figure 3.3.4 a) the stable ferroelectric phases are determined. The phase with the lowest free energy determines the stable phase and it can be seen that for low zirconium concentrations the three consecutive phase transitions from cubic to tetragonal to orthorhombic and to rhombohedral are observed. At larger zirconium concentrations only one

[§§] For an electric field increase, the largest value in the EC temperature change is observed at T_C. The EC temperature changes are depicted as a function of the starting temperature of the calculation. Therefore, the largest EC temperature change is observed slightly above T_C at a temperature at which the polarization goes back to zero for zero electric field. In other words, the final temperature is T_C. For illustration, see Figure 1.3.2 a).

ferroelectric phase, i.e. the rhombohedral phase, is stable down to the lowest temperature of 0 K. For the determined stable ferroelectric phases, the corresponding spontaneous polarization is displayed in Figure 3.3.4 b). The direction of the spontaneous polarization is [001], [110] and [111] for the tetragonal, orthorhombic and rhombohedral phase, respectively. To highlight some trends in the spontaneous polarization of the $Ba(Zr_xTi_{1-x})O_3$ system, the spontaneous polarization of four selected compositions is depicted in Figure 3.3.4 c). For BT a large discontinuity in the spontaneous polarization is observed at T_C. The discontinuity in the spontaneous polarization at the interferroelectric phase transitions is much lower. For $Ba(Zr_{0.08}Ti_{0.92})O_3$ the discontinuity in the spontaneous polarization at T_C is much smaller than for BT and the discontinuities in the spontaneous polarization at the interferroelectric phase transitions are vanishingly small. For $Ba(Zr_{0.15}Ti_{0.85})O_3$ only one phase transition from the cubic phase to the rhombohedral phase is observed. This phase transition is of second order character with continuous spontaneous polarization. With increasing the zirconium concentration the spontaneous polarization gets smaller, i.e. for $Ba(Zr_{0.20}Ti_{0.80})O_3$. The general trends are that by increasing the zirconium concentration, the first order character of the phase transition gets smaller. At a certain concentration the first order character changes into a second order phase transition from the paraelectric to ferroelectric phase.

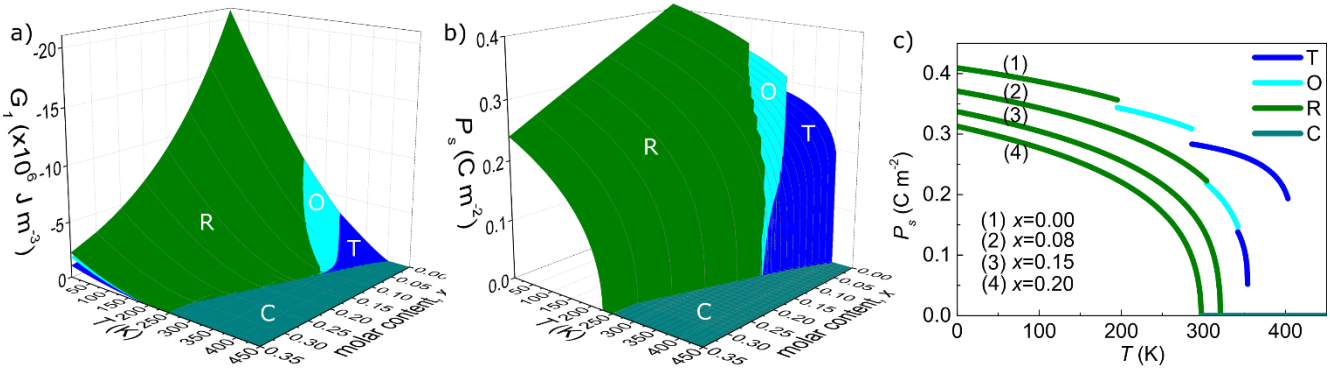

Fig. 3.3.4: a) Composition – temperature – free energy phase diagram for the $Ba(Zr_xTi_{1-x})O_3$ system. b) Spontaneous polarization in the stable phases as function of the compositional and temperature range. c) Spontaneous polarization as function of temperature for the $Ba(Zr_xTi_{1-x})O_3$ systems with x=0, x=0.08, x=0.15 and x=0.2.

From the phase diagram and the corresponding spontaneous polarization in Figure 3.3.4 it can be deduced that two special compositions occur in the $Ba(Zr_xTi_{1-x})O_3$ system. At one composition the line of first order phase transitions passes over into a line of second order phase transitions, i.e. the tricritical point (TCP). At one composition the line of cubic to tetragonal phase transition passes over into a line of cubic to rhombohedral phase transitions, i.e. the triple point. The necessary condition[288] for the TCP is,

$$B_1 + B_2 = 0, \tag{3.3.8}$$

and for the triple point,

$$B_2 = 0. \tag{3.3.9}$$

This means that at the composition of the TCP the sum of the isotropic quartic coefficient and the anisotropic quartic coefficient, i.e. B_1+B_2, vanishes at T_C. Whereas, at the composition of the triple point the anisotropic quartic coefficient, i.e. B_2, vanishes at T_C. The sum of the isotropic and anisotropic quartic coefficients and the anisotropic quartic coefficient are shown at T_C of the respective composition in Figure 3.3.5 a). The TCP is found at a zirconium content of around ~0.09 and the triple point is found at a zirconium concentration of around ~0.11.

With the above considerations a phase diagram for the $Ba(Zr_xTi_{1-x})O_3$ system is calculated, see Figure 3.3.5 b). The differently colored lines denote the phase transition lines, where black denotes the cubic to tetragonal phase transition, red denotes the tetragonal to orthorhombic phase transition, blue denotes the orthorhombic to rhombohedral phase transition and pink denotes the cubic to rhombohedral phase transition. Furthermore, the TCP and the triple point are indicated in the phase diagram by orange stars. The calculated phase transition lines coincide well with the experimentally observed phase transition temperatures in this work and by Zhi et al.[198].

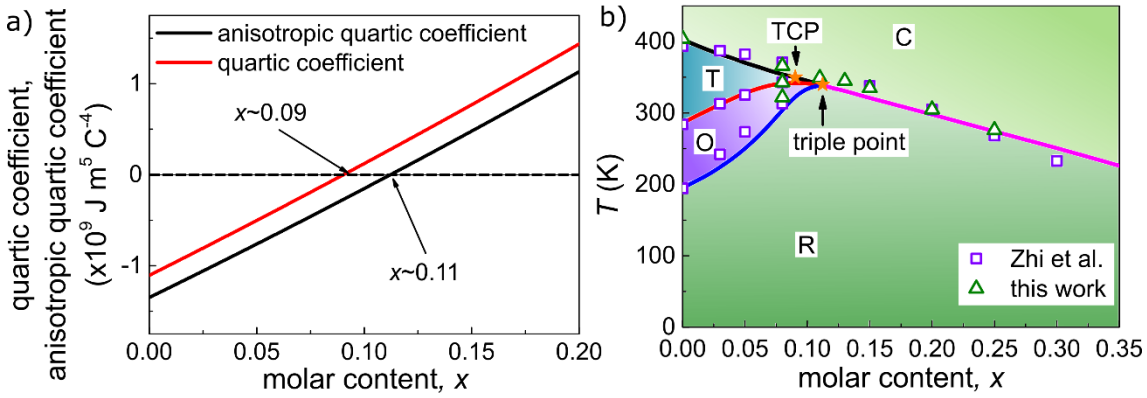

Fig. 3.3.5: a) Quartic coefficient, i.e. B_1+B_2, and anisotropic quartic coefficient, i.e. B_2, as function of composition. b) Calculated phase diagram for the $Ba(Zr_xTi_{1-x})O_3$ system. Black line denotes the phase transition line between the cubic and tetragonal phase. Red line denotes the phase transition line between the tetragonal and orthorhombic phase. Blue line denotes the phase transition line between the orthorhombic and rhombohedral phase. Pink line denotes the phase transition line between the cubic and rhombohedral phase. The tricritical point (TCP) and the triple point are indicated by orange stars. Data points for the phase transition temperatures deduced from this work and from Zhi et al.[198] are included as green triangles and purple squares, respectively.

To elucidate that truly the composition at the TCP and the triple point are different, the anisotropic free energies for the three ferroelectric phases are depicted for four selected compositions in Figure 3.3.6. The anisotropic free energy is chosen, as it is clearer to see which ferroelectric phase exhibits the lowest energy and therefore is the stable phase. For $Ba(Zr_{0.08}Ti_{0.92})O_3$ three consecutive phase transitions are

found (all with first order character). The composition at the TCP also exhibits three consecutive phase transitions but the cubic to tetragonal phase transition is of second order. For $Ba(Zr_{0.10}Ti_{0.80})O_3$ the cubic to tetragonal phase transition is also of second order and still three consecutive phase transitions are found. At the composition of the triple point the anisotropic free energy of the phases is equal at T_C but at lower temperatures the rhombohedral phase is the only stable one.

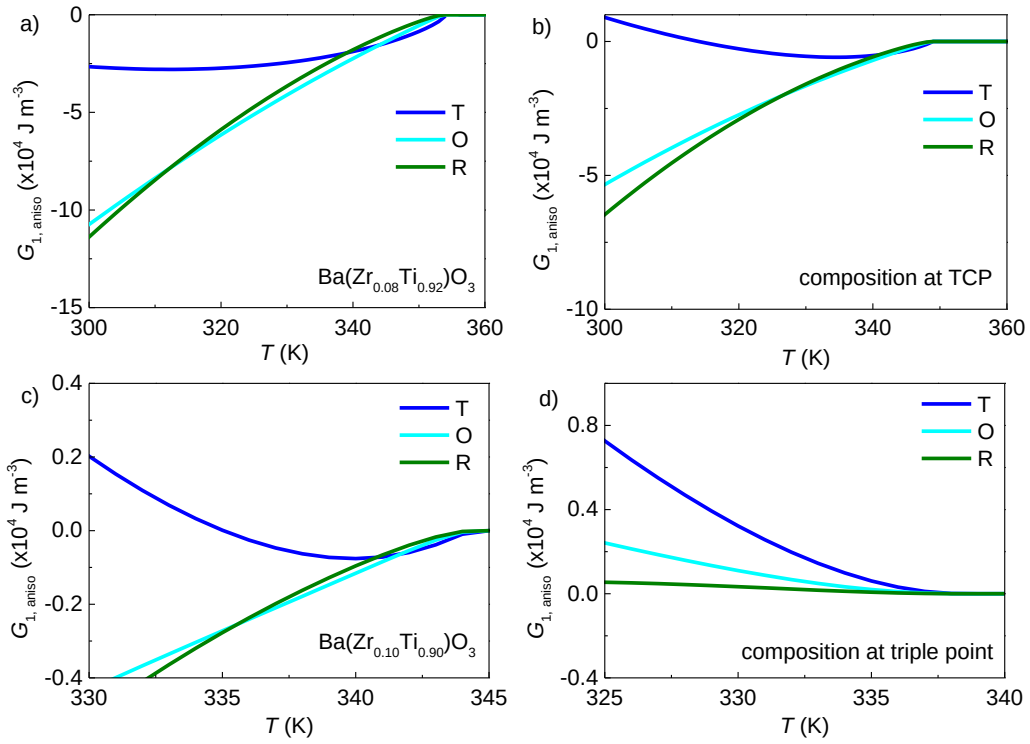

Fig. 3.3.6: Anisotropic free energy of the three ferroelectric phases as function of temperature for a) $Ba(Zr_{0.08}Ti_{0.92})O_3$, b) the composition at the tricritical point (TCP), c) $Ba(Zr_{0.10}Ti_{0.90})O_3$ and d) composition at the triple point. The stable ferroelectric phase is the one with the most negative or least positive anisotropic free energy.

As pointed out, at the TCP the features of a first order phase transition disappear and a continuous phase transition appears. Furthermore, from electric field – pressure – temperature phase diagrams it was shown that at the TCP three lines of critical phase transitions converge.[94] This lines of critical phase transitions are a line of second order phase transitions, which, in fact are also critical phase transitions, and two lines of electrical critical end points. Here, the two lines of critical end points are related to opposite electric field directions.

In the case of the $Ba(Zr_xTi_{1-x})O_3$ system the pressure parameter can be exchanged by the compositional parameter and the TCP can be found in the electric field – composition – temperature phase diagram. The critical end points are calculated for the compositions from BT to the composition at the TCP. In Figure 3.3.7 a) the critical electric fields are depicted as function of the compositional range. With increasing zirconium content E_{cr} gradually decreases, rapidly for lower zirconium content and then

converges to E_{cr}=0 kV mm^{-1} approaching the composition at the TCP. A similar behavior is observed for the temperature range between T_C and the critical temperature in Figure 3.3.7 b). A large temperature range is observed for BT with ~12.5 K which gradually decreases and converges to zero approaching the composition at the TCP.

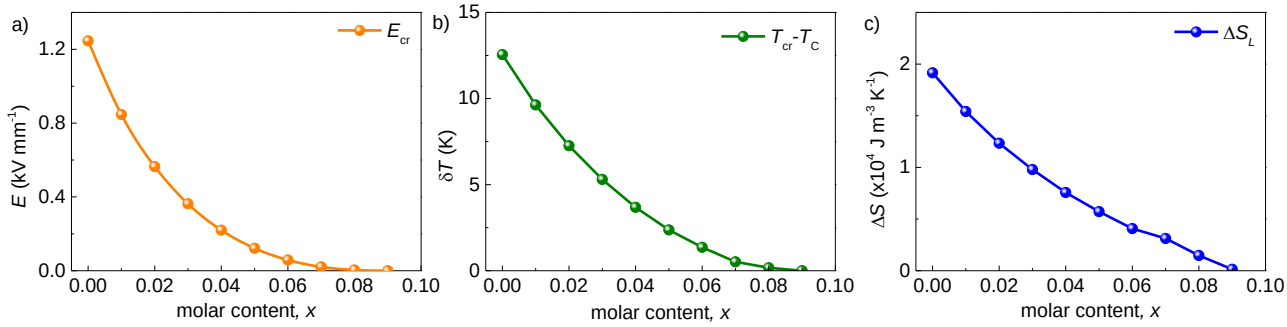

Fig. 3.3.7: a) Electric field of the critical end point as function of composition. b) Temperature range between the Curie temperature and the temperature of the critical end point as function of composition. c) Entropy change as function of composition from the latent heat calculated with the Clausius – Clapeyron equation.

From the calculated electric field – temperature phase diagrams and the polarization discontinuities at T_C, the entropy change due to the latent heat can be calculated by the Clausius – Clapeyron equation (Equation 3.3.7). The entropy change at the respective Curie temperatures of the compositions gradually decreases with increasing zirconium content. Approaching the composition at the TCP the entropy change due to a first order phase transition disappears. For BT the disappearance of the latent heat was connected to an electric field increase to E=E_{cr}. Here, the disappearance of the latent heat is connected to an increase of zirconium content.

By using the calculated critical end points, an electric field – composition – temperature phase diagram is constructed. This was never done before for a ferroelectric material system. The phase diagram is depicted in Figure 3.3.8. Here, the orange line denotes the line of first order phase transitions, the green line denotes the line of second order phase transitions and the blue lines denote the lines of critical end points at E=+E_{cr} and E=-E_{cr}. The TCP is indicated by a brown dot.

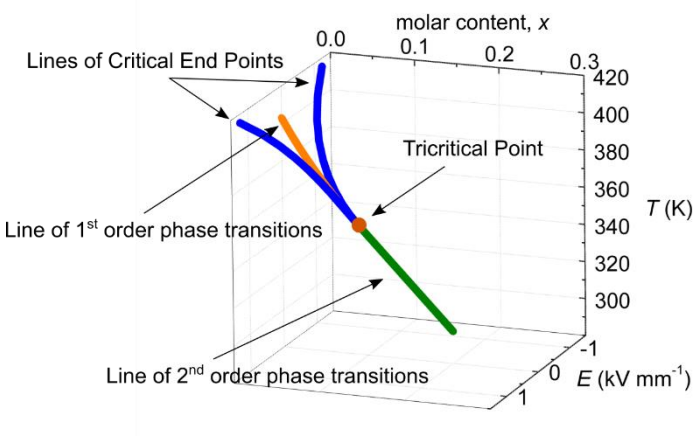

Fig. 3.3.8: Electric field – composition – temperature phase diagram of the $Ba(Zr_xTi_{1-x})O_3$ system. The orange line denotes a line of first order phase transitions. The green line denotes a line of second order phase transitions. The two blue lines denote the lines of critical end points for $E=+E_{cr}$ and $E=-E_{cr}$. The tricritical point is indicated by a brown dot. At the tricritical point the three lines with critical phase transitions, i.e. line of second order phase transitions and the two lines of critical end points, converge.

The EC properties of the $Ba(Zr_xTi_{1-x})O_3$ system are depicted in Figure 3.3.9 a). A typical behavior in the EC temperature change for materials with first order phase transitions can be seen for compositions between $x=0$ and $x=0.08$. The latent heat of the electric field induced first order phase transition leads to a jump in the EC temperature change slightly above T_C (see discussion for BT). As seen, the latent heat of the electric field induced phase transition decreases with increasing zirconium content. In the same manner, the maximum EC temperature change decreases. No enhanced EC properties are found for the composition at the TCP. Here, the zero electric field phase transition is from cubic to tetragonal phase. For $Ba(Zr_{0.10}Ti_{0.80})O_3$ the maximum EC temperature change is lower than for the composition at the TCP. For the composition at the triple point an increase in the maximum EC temperature change is observed compared to slightly higher or lower zirconium contents. Such an increase in the EC performance was found experimentally for a composition of $x=0.13$ in this work. With increasing zirconium content the maximum EC temperature change gradually decreases. The same behavior is found for the entropy change calculated for the same compositions and depicted in Figure 3.3.9 b). From the contour plot in Figure 3.3.9 c) it can be seen that the maxima in the EC temperature change follow the paraelectric to ferroelectric phase transition temperatures in the phase diagram. Following the dark blue area in the contour plot it is seen that a temperature change of around ~0.5 K or larger is found over a temperature range of around ~40 K independent on the composition. In other words, materials with first order phase transitions exhibit equal ECE over the same temperature ranges as materials with second order phase transitions but superimposed by a peak in the EC temperature change due to the electric field induced first order phase transition.

The increase in the EC temperature change for the composition at the triple point compared to compositions with slightly larger and lower zirconium content can be explained by taking a look at the polarization that can be induced by an electric field. In Figure 3.3.9 d) the polarization under an electric

field of E=2 kV mm^{-1} at the Curie temperature is depicted as a function of the composition. For BT the largest polarization can be induced by the electric field. This induced polarization at T_C decreases with increasing zirconium content for the compositions that exhibit a cubic to tetragonal phase transition. Approaching the composition at the triple point, the induced polarization suddenly increases and decreases again for larger zirconium content. This increase in the induced polarization is responsible for the increase in the maximum EC temperature change for the composition at the triple point. Note that above T_C, i.e. in the paraelectric phase for zero applied electric field, the polarization is zero.

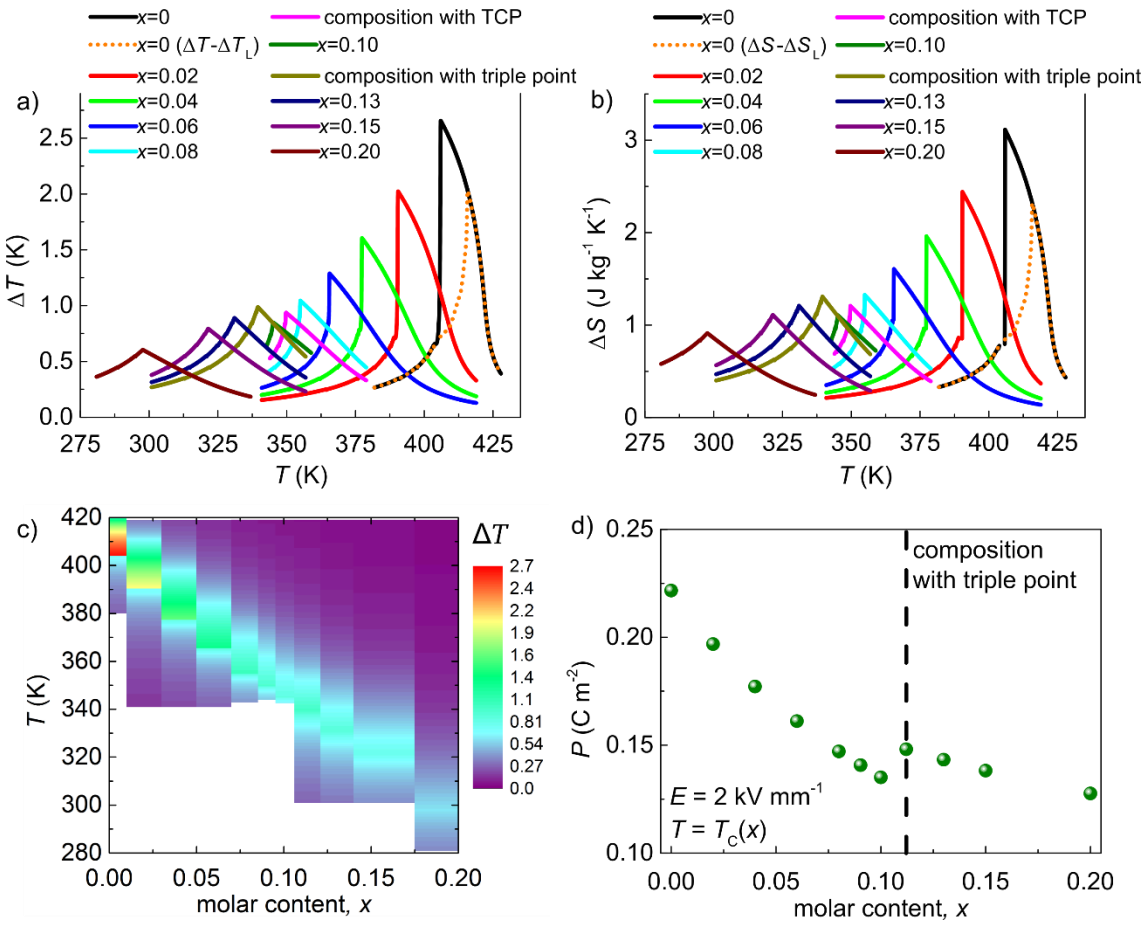

Fig. 3.3.9: a) EC temperature change calculated for selected compositions under the electric field removal from E=2 kV mm^{-1} to E=0 kV mm^{-1}. The orange dots denote the temperature change for BT subtracted by the temperature change due to the latent heat. b) Entropy change calculated for selected compositions under the electric field removal from E=2 kV mm^{-1} to E=0 kV mm^{-1}. The orange dots denote the entropy change for BT subtracted by the entropy change due to the latent heat. c) Contour plot of the EC temperature change as function of the composition and temperature range. d) Polarization as function of composition at the respective Curie temperature and an electric field E=2 kV mm^{-1}.

It is seen that for suitable parameters in the phenomenological theory phase diagrams and EC properties of the $Ba(Zr_xTi_{1-x})O_3$ system can be determined. For a material exhibiting a first order paraelectric to ferroelectric phase transition at zero electric field, the existence of the critical end point was demonstrated. By subtracting the contribution of the latent heat from the EC temperature change it was shown that the largest EC response is found at the critical end point. For the $Ba(Zr_xTi_{1-x})O_3$ system a

complete composition – temperature phase diagram was calculated with a TCP and triple point. Furthermore, by taking into account the electric field induced phase transition an electric field – composition – temperature phase diagram was constructed. The EC temperature changes of the $Ba(Zr_xTi_{1-x})O_3$ system were calculated and it was demonstrated that the triple point has an influence on enhancing the EC properties due to larger electric field induced polarization above the Curie temperature.

3.4. Long Term Stability of the Electrocaloric Effect

Most studies on the electrocaloric effect focus on the EC temperature change that can be achieved. It must be considered that a possible electrocaloric device has to operate over a huge number of cycles, depending on the specific device design and area of operation that might be more than 10^6 cycles.[27, 65] With respect to that, the information on the long term stability of the ECE in electrocaloric materials is presently lacking. The first investigation was recently published by Fulanović et al. and demonstrated the fatigue-less behavior of PMN multilayer elements.[292] Nevertheless, the behavior of other EC materials, considering the ECE, was not investigated so far.

Here, a $Ba(Zr_{0.2}Ti_{0.8})O_3$ composition was chosen as the largest ECE occurs slightly above room temperature. The temperature range of operation for mobile devices, where EC cooling is considered to be a possible candidate, is between room temperature and 350 K.[1, 293, 294] Therefore, the $Ba(Zr_{0.2}Ti_{0.8})O_3$ composition is considered as a possible EC material if substantial EC temperature changes can be achieved and long term stability is ensured.

The following section is based on published results.[295] The investigated $Ba(Zr_{0.2}Ti_{0.8})O_3$ sample was characterized based on structural and crystallographic features. Direct measurements of the EC temperature change were conducted over a broad temperature range and for a large number of cycles. It was shown that the EC temperature change is stable till 10^5 cycles but an increased leakage current occurs after 10^6 cycles. The increased leakage current lead to Joule heating and prevented further measurement of the EC temperature change. The origin of the increased leakage current was investigated by means of dielectric permittivity measurements, current density measurements and impedance spectroscopy. In the end a solution to the stability problem is given which leads to a constant EC temperature change up to 10^6 cycles.

To determine the microstructural and crystallographic features of the investigated $Ba(Zr_{0.2}Ti_{0.8})O_3$ sample, images of the grain morphology were taken with an optical microscope and room temperature XRD scans were conducted with a diffractometer. Figure 3.4.1 depicts a) the microstructure and b) the XRD pattern. The grain size was analyzed by the linear intercept method[296] and a mean grain size of $\sim$24 μm was determined. All peaks of the XRD pattern can be assigned to the $Ba(Zr_{0.2}Ti_{0.8})O_3$ sample and no evidence of secondary phases could be found, thus suggesting pure perovskite phase. The pure phase leads to the assumption that Zr^{4+}-ions are fully incorporated in the lattice, despite the larger ionic radius of Zr^{4+}-ions (0.084 nm) compared to Ti^{4+}-ions (0.061 nm).[191] Furthermore, the calculated cell volume of 66.43 Å^3 is comparable to earlier studies and larger than the cell volume of barium titanate, which suggests the full incorporation of Zr^{4+}-ions without the forming of secondary phase.[204, 297] The

room temperature structure is assumed to be pseudo-cubic as no peak splitting could be observed within the resolution of the diffractometer.

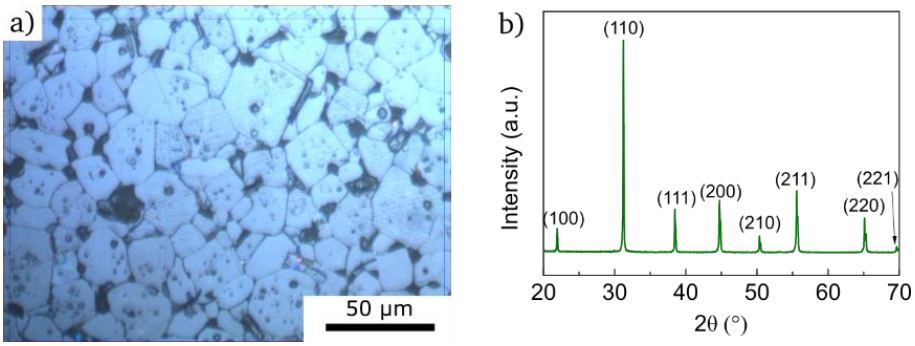

Fig. 3.4.1: a) Microstructure of a $Ba(Zr_{0.2}Ti_{0.8})O_3$ sample sintered at 1623 K for 30 min. Image was taken with an optical microscope. b) X-ray diffraction spectrum taken at room temperature for a sintered $Ba(Zr_{0.2}Ti_{0.8})O_3$ sample. Diffraction peaks are indicated with the corresponding (hkl) values.

An exemplary EC measurement at 300 K (note that all cycling experiments were conducted at room temperature) is depicted in Figure 3.4.2 a). The electric field was applied and removed four times with increasing magnitude of the electric field. It is highlighted by the dashed lines that the EC temperature changes at electric field increase and removal, i.e. heating and cooling, are the same. This illustrates that the hysteretic losses as well as leakage current, which might lead to Joule heating, is negligible at room temperature. At an electric field change of 2 kV mm^{-1} the EC temperature change is 0.2 K. The EC temperature change as a function of measurement temperature for four electric field changes is depicted in Figure 3.4.2 b). The EC temperature change steadily increases with increasing temperature from 250 K to 310 K where a peak in the EC response is observed. On the high temperature side of the ECE peak the EC temperature change decreases steadily. A nearly symmetric behavior can be observed, which mimics the dielectric behavior. The investigated $Ba(Zr_{0.2}Ti_{0.8})O_3$ sample was sintered at the same temperature as the samples in section 3.2., but with a holding time at the sintering temperature of 0.5 h instead of 2 h. To demonstrate that the reduced holding time has no influence on the EC response the EC temperature change of a sample sintered with 2 h holding time is provided as dashed line in Figure 3.4.2 b). It can be seen that the EC response is the same for samples with 0.5 h and 2 h holding time.

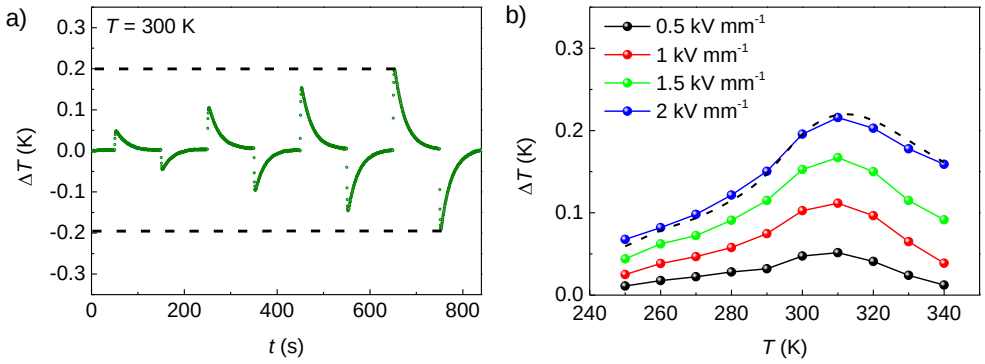

Fig. 3.4.2: a) Electrocaloric temperature change of a $Ba(Zr_{0.2}Ti_{0.8})O_3$ sample sintered at 1623 K for 30 min. The applied electric fields were 0.5 kV mm^{-1}, 1 kV mm^{-1}, 1.5 kV mm^{-1}, and 2 kV mm^{-1}. The measurements were conducted at 300 K chamber temperature. The black dotted lines are guides to the eye, showing that at 300 K the heating peak at electric field application and the cooling peak at electric field removal exhibit the same absolute value. b) Electrocaloric temperature change as a function of measurement temperature of a $Ba(Zr_{0.2}Ti_{0.8})O_3$ sample sintered at 1623 K for 30 min. The applied electric fields were 0.5 kV mm^{-1}, 1 kV mm^{-1}, 1.5 kV mm^{-1}, and 2 kV mm^{-1}. The black dashed line shows the electrocaloric temperature change for a $Ba(Zr_{0.2}Ti_{0.8})O_3$ sample sintered at 1623 K for 120 min, at an applied electric field of 2 kV mm^{-1}.

For the long term stability measurements of the EC response of a $Ba(Zr_{0.2}Ti_{0.8})O_3$ sample an electric field function with fast application/removal of the electric field and holding times with constant electric fields in between was used (depicted in the inset of Figure 3.4.3 a)). One cycle included the application and the removal of the electric field. The repetition rate was 10 cycles per second, to conduct a substantial amount of cycles in a reasonable time. It was checked by an oscilloscope connected by high voltage terminals that the rise and fall time of the voltage signal (produced by the high voltage amplifier) was fast enough for the repetition rate. The rise/fall time between zero and maximum applied electric field was 500 μs, which is 100 times smaller than the holding time at constant electric field. The rising electric field exhibited an overload of about 8 % that got damped within one oscillation to the desired electric field. This shows that with the measurement arrangement used the long term stability of EC response can be tested. After certain amounts of cycles the electric field signal was stopped to measure the EC temperature change. Afterwards, the electric field signal of cycling was applied again.

The EC response as function of the cycle number is depicted in Figure 3.4.3 a). The cycling as well as the EC measurement were conducted with an electric field change of 2 kV mm^{-1}. The EC temperature change is shown normalized to the EC temperature change before the cycling. A constant EC response is found up to 10^5 cycles. After cycling further up to 10^6 cycles the EC temperature change cannot be determined anymore (depicted by a red cross in Figure 3.4.3 a)). The difference in the EC measurement after 10^5 and 10^6 cycles can be seen in Figure 3.4.3 b) and c), respectively. After 10^5 cycles sharp changes in the sample temperature are measured when the electric field is applied and removed. In comparison after 10^6 cycles the temperature rises in an exponential manner towards ~3.7 K temperature difference between sample and the surrounding. When the electric field was removed, the sample temperature

relaxed back to the temperature of the surrounding. The observed behavior can be assigned to substantial leakage current and therefore Joule heating. At t=200 s the produced heat (Joule heating) is approximately the same as the heat that goes out of the sample to the surrounding (steady state). This can be expressed as:

$$\dot{Q}_{Joule} = \dot{Q}_{out}. \tag{3.4.1}$$

For the produced Joule heat the electrical power can be inserted and the rate of the heat that goes to the surrounding can be described by the thermal conductance (inverse of thermal resistance) and the temperature difference.

$$I \cdot U = K \cdot \Delta T = \frac{1}{R}\Delta T. \tag{3.4.2}$$

The thermal conductance can be expressed as the convective heat transfer coefficient (h) and the total surface area of the sample (A=5x10^{-5} m^2).

$$I \cdot U = h \cdot A \cdot \Delta T. \tag{3.4.3}$$

The convective heat transfer coefficient can be assumed to be in the range between 4 W m^{-2} K^{-1} and 10 W m^{-2} K^{-1}.[241, 242] Using the approximations described above a leakage current in the range I=1.8x10^{-6} A to I=4.5x10^{-6} A is expected.

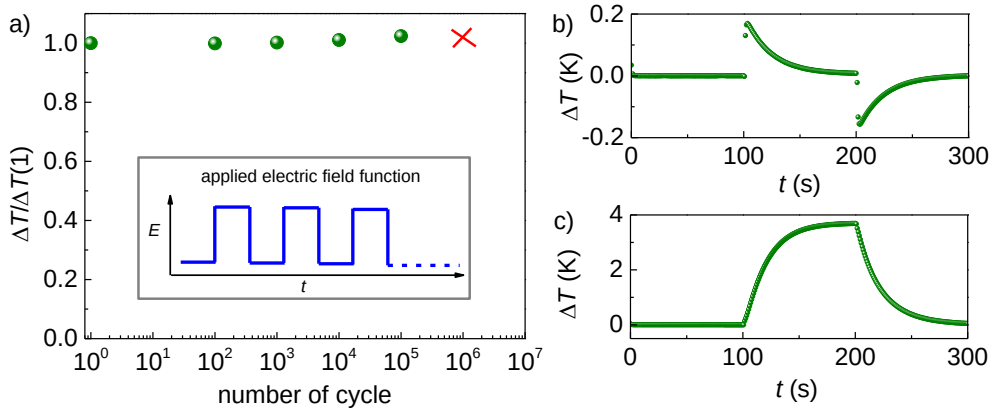

Fig. 3.4.3: a) Electrocaloric temperature change as function of the number of cycles normalized to the electrocaloric temperature change at the first electric field cycle. The red cross indicates that the electrocaloric temperature change could not be determined after 10^6 cycles, because of tremendous Joule heating. The inset depicts the shape of the electric field function applied during cycling. b) Measurement of the electrocaloric temperature change after 10^5 cycles. c) Measurement of the electrocaloric temperature change after 10^6 cycles.

The effect of the leakage current can also be seen in Figure 3.4.4, where polarization measurements are shown. The polarization loops were measured after every cycling step. After the cycling electric field was

stopped first the EC temperature change was measured and second the polarization response. For the polarization measurement the first increase in the applied electric field (positive electric field axis) had the same polarity as the cycling electric field. Note that the bipolar polarization measurements had no influence on the further cycling. This was tested by cycling 10^5 times without intermediate measurements and the same results were obtained. It is observed that the saturation polarization at the positive electric field axis is constant till 10^5 cycles. In the negative electric field axis the polarization response only slightly changes. After 10^6 cycles the measured polarization response drastically increases and shows rectifying behavior. The leakage current increases the measured polarization values by charging the reference capacitor in the measurement setup. This seems to occur more pronounced if the applied electric field has the same polarity as the cycling electric field. Therefore, at the second cycle the reference capacitor is more charged than in the first cycle. The leakage current may be different in magnitude depending on the polarity of the applied electric field. After thermal annealing the sample at 420 K for 10 min the polarization response was measured again and the initial behavior was fully regained. This suggests that by thermal activation the thermodynamically favored state of the $Ba(Zr_{0.2}Ti_{0.8})O_3$ sample can be recovered.

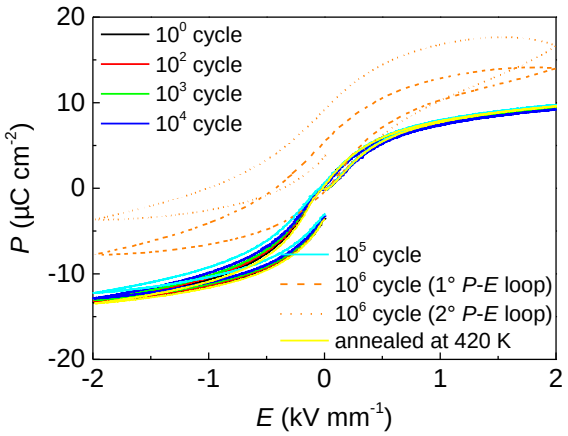

Fig. 3.4.4: Measurement of the bipolar polarization loop after the cycles denoted in the legend. The polarity of the first electric field increase (positive electric field values) is the same as the cycling square wave. After 10^6 cycles the first measurement of polarization loop (dashed orange line) and the subsequent second polarization loop (dotted orange line) are depicted. The polarization loop (subsequent to poling cycle) after annealing the cycled sample at 420 K for 10 min is shown (yellow line).

To investigate the origin of the drastically increased leakage current after 10^6 cycles, the dielectric permittivity and loss tangent were measured in the temperature range from 220 K to 400 K. The sample was cooled down subsequent to cycling 10^6 times and then measured under heating. The real part and the imaginary part of the dielectric permittivity can be seen in Figure 3.4.5 a) and b) for the initial sample, c) and d) for the sample after 10^6 cycles, and e) and f) for the sample after thermally annealing at 420 K for 10 min. In the initial state the $Ba(Zr_{0.2}Ti_{0.8})O_3$ sample exhibits a broad peak in the real part of the dielectric permittivity around the peak temperature (T_m) at 310 K. This coincides with the EC

behavior observed by EC temperature change measurements. No shift with measurement frequency is observed around T_m. In the imaginary part of the dielectric permittivity an asymmetry in the peak is observed and the peak shifts to higher temperatures with increasing measurement frequency.

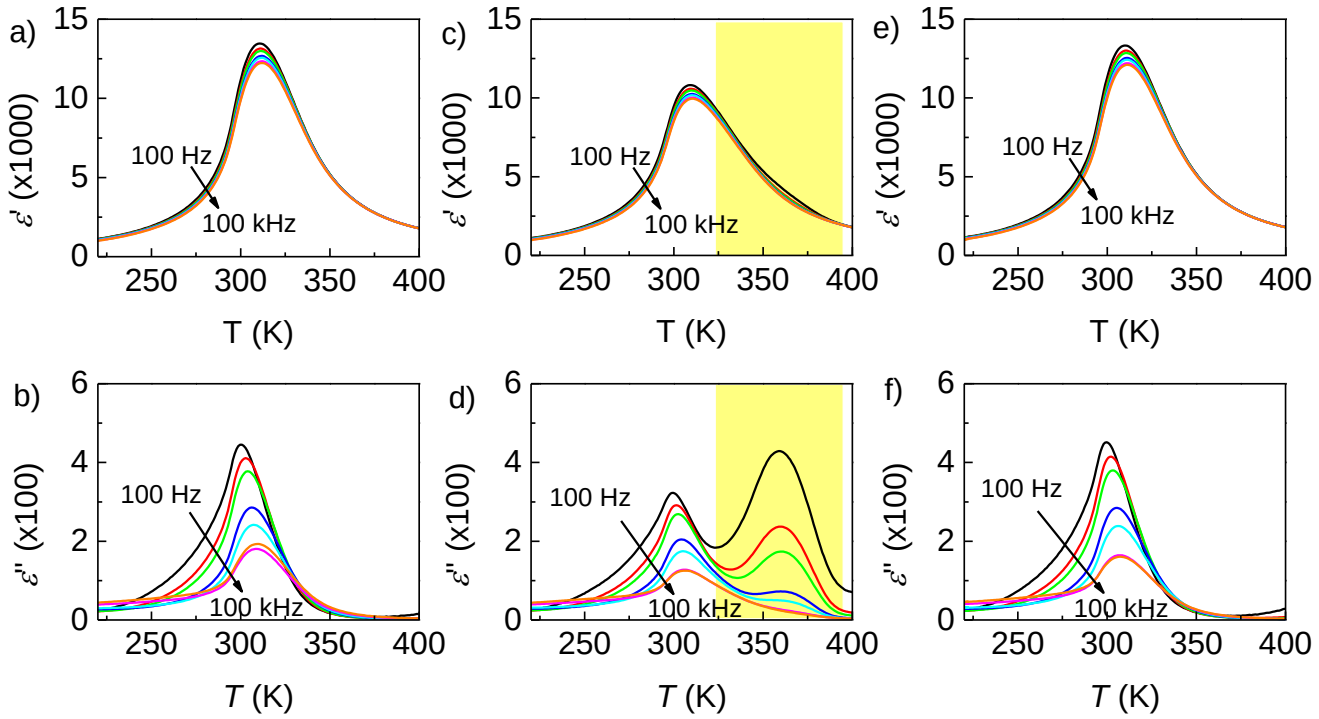

Fig. 3.4.5: Real and imaginary part of the dielectric permittivity as a function of temperature measured at several excitation frequencies: 100 Hz, 500 Hz, 1 kHz, 5 kHz, 10 kHz, 50 kHz, 100 kHz. a) and b) before cycling, c) and d) after 10^6 cycles, and e) and f) after thermal annealing at 420 K for 10 min. The yellow shaded temperature range in c) and d) denotes the appearance of a second peak in the real and imaginary part of the dielectric permittivity after 10^6 cycles.

After cycling 10^6 times, the real part and imaginary part of the dielectric permittivity decreases by ~25 % at T_m. The temperature position of the peaks is the same as for the sample at the initial state. After cycling a second peak in the imaginary part of the dielectric permittivity appears at higher temperatures ~360 K (depicted by the yellow area in Figure 3.4.5 d)). This second peak is more pronounced for lower measurement frequencies. After thermally annealing the sample at 420 K for 10 min, the second peak observed for the cycled sample disappears and the initial measurement response is recovered. Dielectric relaxation above the ferroelectric to paraelectric phase transition temperature was demonstrated for several titanate ferroelectrics, i.e. strontium titanate, barium titanate, and calcium titanate, and was connected to oxygen vacancies.[298, 299]

From the EC, polarization and dielectric measurements it can be assumed that migration of oxygen vacancies over the 10^6 electric field cycles leads to a change in the defect chemistry of the $Ba(Zr_{0.2}Ti_{0.8})O_3$ sample. This might be also the origin of the reduction of the dielectric permittivity at T_m. The movement of oxygen vacancies by the applied electric field into one direction can result in an inhomogeneous sample. The catalytic behavior of the electrode material, in this case silver, determines the incorporation

and excorporation of oxygen vacancies at the electrodes. The incorporation and excorporation can be equal, it can be unequal, or it can be hindered with no exchange between the material and the electrode. Hence, the oxygen vacancies can pile up, deplete or both at the electrodes. To restore charge neutrality in those regions, the electronic charge carrier concentration can change.[165, 169] The electronically different regions around the anode and cathode can lead to the different dielectric response.

To demonstrate the effect of oxygen vacancy movement on the dc conductivity, the leakage current density was measured over time under an applied electric field of 2 kV mm^{-1} (=410 V). In Figure 3.4.6 the leakage current density is depicted for a sample in the initial state (blue points). After the measurement was conducted, the polarity of the electric field was changed and the leakage current density was measured with reversed electric field polarity (orange points).

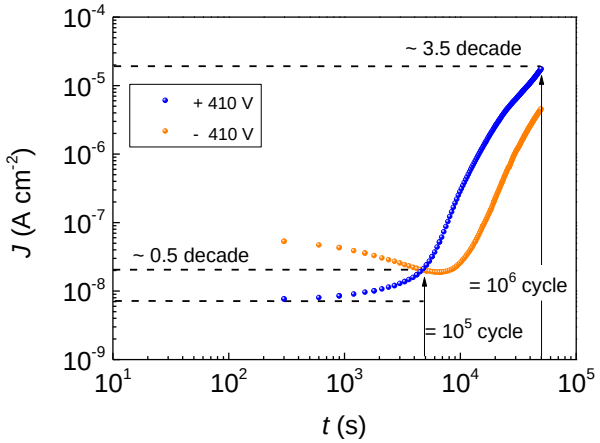

Fig. 3.4.6: Leakage current density as a function of time measured at room temperature with an applied potential of 410 V (= 2 kV mm^{-1}). The + and – denote that the polarity of the potential was changed between the two measurements. The first measurement on an uncycled sample is denoted with + (blue points). The second measurement denoted with a – (orange points) was conducted on the same sample subsequent to the first measurement. Arrows depicted with 10^5 cycle and 10^6 cycle are included as guide to the eye (the conversion from cycles to the time scale was conducted by considering the time of constant applied maximum electric field). The remarks 0.5 decade and 3.5 decade refer to the increase of leakage current density with respect to the first measurement point of the uncycled sample (blue points).

In the initial state the $Ba(Zr_{0.2}Ti_{0.8})O_3$ sample exhibits a leakage current density of 7x10^{-9} A cm^{-2}. After 5000 s (this corresponds to 10^5 cycles) the leakage current density is three times larger. After 50000 s (this corresponds to 10^6 cycles) the leakage current density increased by 3.5 decades, showing the drastic change in the defect chemistry. In the subsequent measurement with reversed polarity of the electric field, the leakage current at the beginning of the measurement is 5x10^{-8} A cm^{-2}. The leakage current density starts to slowly decrease until it increases again after ~6000 s. To further demonstrate the behavior of the leakage current on the polarity of the applied voltage, *I* – *V* curves are provided in Figure 3.4.7. Here, the *I* – *V* characteristic of the sample after 10^6 cycles (blue points) and after thermal annealing at 420 K for 10 min (green points) is shown. The positive voltage axis coincides with the

polarity of the voltage applied during the cycling. At 400 V the leakage current of the cycled sample increased to ~1x10^{-6} A (note this is the current range that was calculated from the EC measurement of the sample after 10^6 cycles). In the reverse direction the leakage current stays low. The observed behavior looks similar to the *I* – *V* characteristic of a diode. During the voltage sweep a peak at low voltages is observed for both polarities and for the cycled and annealed sample. This peak is related to the switching current and does not reflect the leakage current of the sample. After thermal annealing the sample does not show a drastic increase of the leakage current and the same behavior independent on the polarity of the applied voltage is found. The measurements highlight that due to the oxygen vacancy movement a rectifying behavior is induced in the sample, meaning that current flow is preferred in one direction.

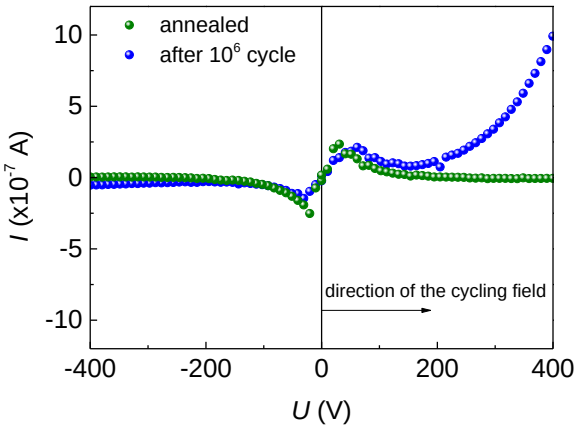

Fig. 3.4.7: Leakage current as function of applied potential. The potential was stepwise increased and held at every step for 2 s. The measurement points denote the leakage current at the end of every step. Depicted are the measurements of a thermally annealed sample (green points) and of a sample after 10^6 cycles (blue points). For the sample cycled 10^6 times, the positive potential axis denotes that the polarity of the potential was in accordance with the cycling potential (depicted by the arrow).

To elucidate the changes in the conductivity, impedance measurements were conducted. The complex impedance of a $Ba(Zr_{0.2}Ti_{0.8})O_3$ sample in the initial state is shown in Figure 3.4.8 a) in the Nyquist representation. It is found that the semicircles usually observed in such a representation cannot be fully resolved due to the large resistivity at the low temperatures. With increasing temperature the resistivity decreases and the semicircles start to build up (note that the description here is based on the measurement frequency). At high temperatures the semicircle is fully seen and even a second semicircle is observed. The second full semicircle is seen in the inset of Figure 3.4.8 a), measured at 573 K. The semicircles in the Nyquist representation can be ascribed to different processes, i.e. grain or grain boundary response. Usually the grain has a smaller resistivity than the grain boundary. Therefore, the first semicircle can be related to the grains of the sample and the second semicircle that appears at higher temperatures to the grain boundaries. Note that the grain boundary resistance is also existent at low temperatures but outside the measurement frequency range, i.e. <10^{-2} Hz. The observation of the second semicircle already leads to the assumption that the first semicircle is related to the grains. This can be

proven by taking the capacitance of the process, see Figure 3.4.8 b).[300] The capacitance follows a temperature behavior similar to the measured dielectric permittivity. Therefore, the response comes from the grains. The capacitance from the grain boundary regions should be nearly temperature insensitive.

The complex impedance of the $Ba(Zr_{0.2}Ti_{0.8})O_3$ sample is now highlighted in Figure 3.4.8 for a cycled and a thermally annealed sample at c) 300 K, d) 360 K, e) 380 K and f) 420 K.

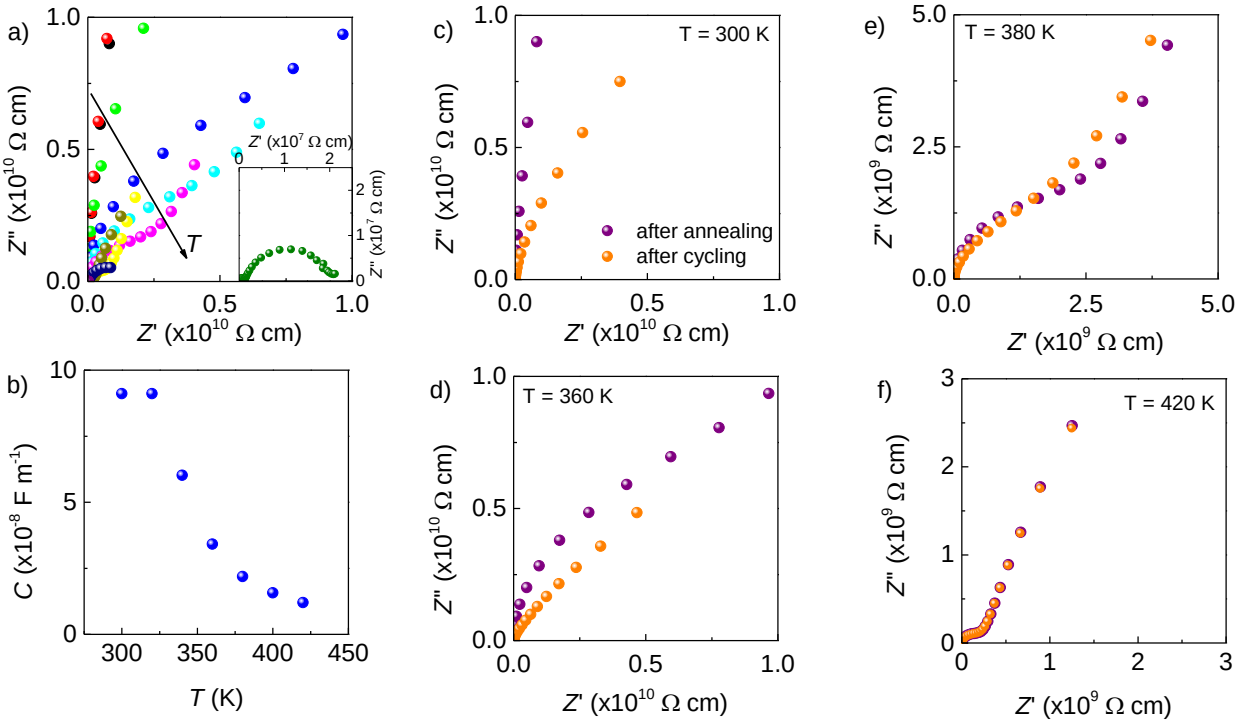

Fig. 3.4.8: a) Complex impedance plot of a $Ba(Zr_{0.2}Ti_{0.8})O_3$ sample at several temperatures: 300 K, 320 K, 340 K, 360 K, 370 K, 380 K, 390 K, 400 K, 420 K, 473 K, and 573 K. The measured frequency range was 10^{-2} Hz to 10^7 Hz. The arrow indicates increasing temperature. The inset is a reduced axis range to highlight the semicircle linked to the grain boundary response in the complex impedance at 573 K (note: the semicircle linked to the grain response is at lower complex impedance and cannot be seen in the chosen axis range). b) Capacitance as a function of temperature. The capacitance values are deduced from the complex modulus data. c) – f) Complex impedance of the sample after 10^6 cycles (orange points) and the sample thermally annealed at 420 K for 20 min (purple points). The measurement temperature was stepwise increased from 300 K to 420 K. Note that the axis ranges are different.

The observed semicircles (or parts of it) can be fitted to an RC element that represents the grain response. If a semicircle is fitted to the measured data, the axis intercept to the real part of the impedance can be determined to obtain the dc resistivity. It is observed that the dc grain resistivity of a cycled sample is lower than after thermal annealing. In other words, the sample with inhomogeneous defect chemistry has a lower resistivity than a homogeneous one. The difference in the complex impedance data becomes less at 360 K. At 380 K the semicircle of the grain response for the cycled and the thermally annealed sample is already similar and at 420 K the complex impedance of the cycled sample recovered the response of a thermally annealed sample. This behavior highlights that by increasing the temperature

the initial defect chemistry can be restored. It can be assumed that after cycling with large electric fields, the oxygen vacancies move towards the cathode and a concentration gradient is established along the axis between cathode and anode. If the cycling is stopped a driving force might exist due to the concentration gradient that oxygen vacancies want to move back towards the anode to reestablish the thermodynamic equilibrium. This is prevented by the low thermal activation at 300 K. If the temperature is increased, the thermal activation increases and oxygen vacancy movement is facilitated. At large temperature, i.e. 420 K, the thermal equilibrium can be achieved again.

To further elucidate the conduction process by the activation energy, the impedance measurements are used for an Arrhenius-type fitting. In Figure 3.4.9 a) the dc conductivities, i.e. the inverse of the dc resistivity, of the grain response are depicted for a cycled (orange points) and a thermally annealed (purple points) sample.

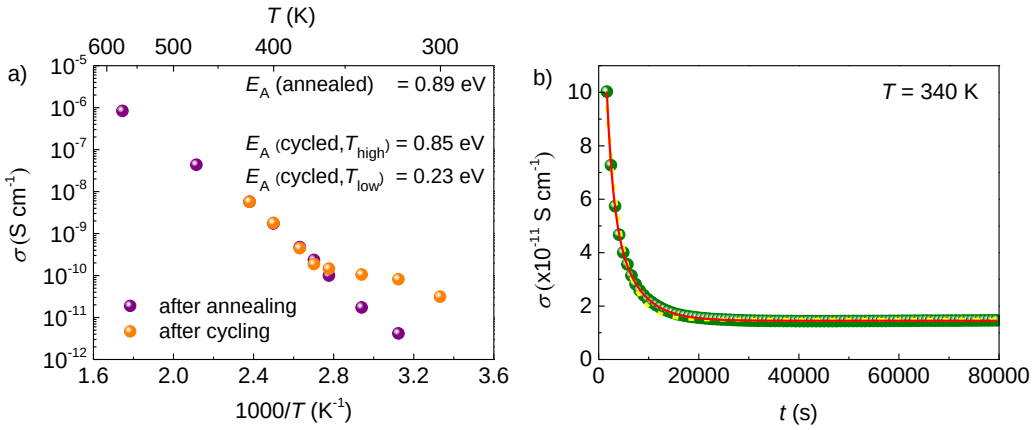

Fig. 3.4.9: a) Arrhenius-type plots of bulk conductivity for $Ba(Zr_{0.2}Ti_{0.8})O_3$. Data points for the sample after annealing at 420 K for 20 min (purple points) and for a sample after 10^6 cycles (orange points) are deduced from the complex impedance. b) Change of bulk conductivity with time for a sample cycled 10^6 times. Subsequent to cycling the sample was heated to 340 K and the complex impedance was measured continuously for 22 h. The first and the last data point show good agreement with corresponding data points of a cycled and thermally annealed sample in a). The time dependent bulk conductivity was fitted with an exponential decay function with one time constant (yellow dashed line) and with two time constants (red solid line).

An Arrhenius-type equation can be used to obtain the activation energy of the respective process:

$$\sigma = \sigma_o \cdot \exp(\frac{-E_A}{k_B T}), \tag{3.4.4}$$

where σ, σ_o, E_A and k_B are the dc conductivity, a prefactor, the activation energy and the Boltzmann constant, respectively. Plotting the y-axis with the natural logarithm of the dc conductivity (note that in Figure 3.4.9 a) the logarithm to the basis 10 is used for clarity) and the x-axis with the inverse temperature, the slope determines E_A/k_B. By this analysis an activation energy for a thermally annealed sample of 0.89 eV across the measured temperature range is found. An activation energy ~0.9 eV is

usually ascribed to long-range movement of oxygen vacancies and was found e.g. in BT.[301, 302] The constant slope in the Arrhenius plot for the thermally annealed sample denotes that ionic conduction is the main mechanism in the measured temperature range. The cycled sample exhibits a smaller slope with an activation energy of 0.23 eV from 300 K to 360 K. This indicates that another conduction mechanism is dominant in the cycled sample compared to the thermally annealed one. The low activation energy might be ascribed to an electronic conduction. Whether this is driven by electrons, holes or both cannot be determined by this analysis. The slope, i.e. the activation energy, of the cycled sample changes above 360 K. Here, an activation energy of 0.85 eV is found, which coincides with the thermally annealed sample and hence long range movement of oxygen vacancies dominates the conduction process again. It is noted that the temperature of change in the activation energy, i.e. 360 K, is the temperature where the second relaxation peak occurs in the dielectric permittivity (see Figure 3.4.5 d)). The thermal annealing effect can be observed in Figure 3.4.9 b). The complex impedance of a cycled sample was measured continuously at 340 K for 22 h. From the measurements the time dependence of the dc conductivity is obtained. It is observed that the dc conductivity at the beginning is equal to the dc conductivity depicted in Figure 3.4.9 a) (orange point at 340 K). With increasing time the dc conductivity exhibits an exponential decrease and the dc conductivity after 22 h is equal to the dc conductivity obtained for a thermally annealed sample (see Figure 3.4.9 a), purple point at 340 K). This demonstrates that the driving force to reach the initial defect chemistry, i.e. thermal equilibrium, is sufficient below 360 K, where the change in activation energy occurs. Nevertheless, the process is slow with a long time constant. A fit to the data by an exponential decay function gave a time constant of 2083 s (yellow dashed line). A better fit could be obtained if two time constants were assumed (red solid line). The time constants were 843 s and 3346 s. The time constant is dependent on the diffusion coefficient, which itself is dependent not solely but also on the activation energy.[303, 304] It might be that the diffusion coefficient changes. A detailed investigation about the diffusion coefficient is outside the scope of this work, but is an interesting open question for further research.

From the analysis of the complex impedance measurements it can be concluded that the thermally annealed sample exhibits mainly ionic conductivity driven by the movement of oxygen vacancies. By cycling the conductivity increases and the main conduction mechanism changes from ionic to electronic conduction. The exact degradation mechanism cannot be determined from the presented measurements but two possibilities can be considered based on the movement of oxygen vacancies. One possibility would include the pile up and depletion of oxygen vacancies at the cathode and anode, respectively.[165, 169] Electrons and holes are then generated to compensate for the inhomogeneous distribution of oxygen vacancies. Those electronic entities contribute then to the increased conductivity. Another possibility would be that only one oxygen transport process at the electrodes is blocked. This would lead to an

oxidized or reduced material with a homogeneous electrical response dominated by large electronic conductivity either by electrons or holes.[164, 305]

From the discussion above it can be seen that the $Ba(Zr_{0.2}Ti_{0.8})O_3$ sample suffers from the movement of oxygen vacancies by the large voltages applied. This changes the defect chemistry and hence leads to increased leakage current density and Joule heating. The Joule heating makes the material impracticable for cooling applications. Increased leakage current density by degradation can also be found in other ferroelectrics like lead zirconate titanate (PZT), but it usually takes longer times.[168] The degradation of ferroelectric properties in PZT or lead-free ferroelectrics, like potassium sodium niobate (KNN), results from trapped charges at the grain boundaries.[306-308] It is suggested that the defect migration across grain boundaries is easier in $Ba(Zr_{0.2}Ti_{0.8})O_3$ samples and therefore degradation occurs over shorter time spans. Nevertheless, the degradation of the long term stability of the EC response might be also given in other ferroelectric materials and a solution should be found to increase the long term stability and make ferroelectric materials practicable for cooling applications.

It was demonstrated by thermal annealing that the degradation process can be reversed, meaning the oxygen vacancies can be redistributed. Oxygen vacancies are electrically positive and move towards the cathode. It is suggested that by changing the polarity of the applied voltage, i.e. exchanging cathode and anode, the redistribution of oxygen vacancies can be triggered. From the leakage current density measurements it is deduced that after 5000 s, i.e. equivalent to 10^5 cycles, the leakage current density strongly increases. Therefore, the cycling is conducted by changing the polarity of the applied voltage every 10^5 cycles (see inset of Figure 3.4.10 a)). The measurements of the EC temperature change under this cycling condition is displayed in Figure 3.4.10 a) and the corresponding polarization response after every 10^5 cycles is depicted in Figure 3.4.10 b).

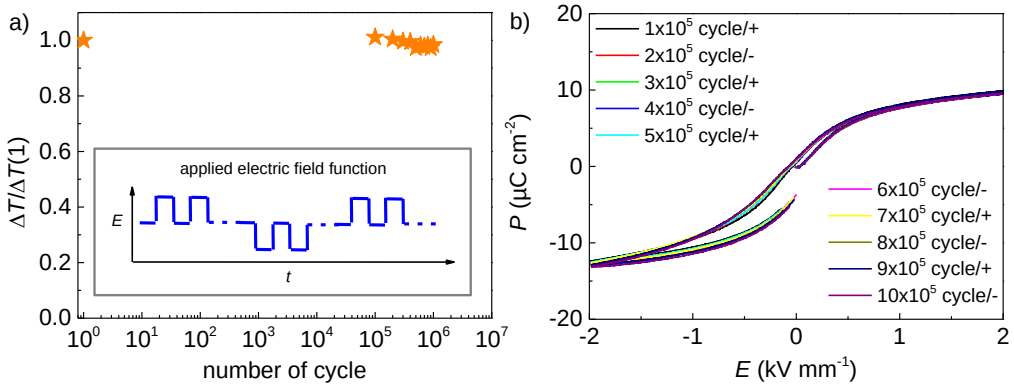

Fig. 3.4.10: a) Electrocaloric temperature change as function of the number of cycles normalized to the electrocaloric temperature change at the first electric field cycle. The polarity of the electric field was changed after every 10^5 cycles. The measurement of the electrocaloric temperature change was conducted with the polarity of the electric field according to the preceding 10^5 cycles. The inset depicts the shape of the electric field function applied during cycling. b) Measurement of the bipolar polarization loop after every 10^5 cycles. The polarity of the first electric field increase (positive electric field values) is the same as the preceding 10^5 cycles. The + and - in the legend denotes that the polarity of the electric field during cycling was switched.

The EC temperature change exhibits stable behavior even after 10^6 cycles. No Joule heating in the EC measurement is observed any more. The EC temperature change decreases by only ~3 % between the measurement before cycling and after 10^6 cycles. The polarization behavior shows similar results and stable maximum polarization in the positive electric field axis. This demonstrates that by reversing the polarity of the applied voltage every 10^5 cycles a stable EC response can be obtained and large cycle numbers, necessary for practical cooling applications, can be achieved.

4. Conclusion

The electrocaloric effect opens the opportunity of solid state cooling devices with possible integration into electronic circuits for on board cooling. In this work the understanding of electrocaloric materials was further promoted by including considerations on the basis of thermophysical properties and long term stability of the electrocaloric temperature change.

To take the right choice of material for the construction of a cooling device, it is necessary to include the thermophysical properties of the material. A material related cooling power was developed as a measure to compare electrocaloric materials. The material related cooling power depends on the dimensionless temperature, the thickness of the electrocaloric plate and the holding time for heat transfer. With a reasonable choice of those parameters the electrocaloric materials can be compared and the difference in the material related cooling power will then depend on the electrocaloric and thermophysical properties of the material. In the development of the material related cooling power the properties of BT and PMN-PT single crystals with [001] orientation were compared. It was found that the higher thermal conductivity of BT significantly contributes to the larger material related cooling power. At temperatures slightly above the Curie temperature, the electric field induced phase transition leads to large electrocaloric temperature changes and hence, the large material related cooling power. For the relaxor-like PMN-PT a much broader range of peak material related cooling power was found, which might be useful for widening the operational temperature range.

From the developed material related cooling power a figure of merit for the electrocaloric effect, as well as for other caloric effects, was deduced. The caloric figure of merit $W = \sqrt{\kappa}\sqrt{\rho c_p}\Delta T$ depends solely on electrocaloric and thermophysical properties and can be used to compare electrocaloric materials as well as other caloric effects with each other. A figure of merit is commonly used to compare thermoelectric materials, but to date no such figure of merit was available for caloric materials.

The caloric figure of merit was used to compare materials of the $Ba(Zr_xTi_{1-x})O_3$ system. Several compositions were prepared and the different paraelectric to ferroelectric phase transition behavior was depicted by dielectric permittivity measurements. For compositions with $x=0$ and $x=0.08$ a first order paraelectric to ferroelectric phase transition with temperature hysteresis between a heating and cooling run was observed. At compositions around $x=0.11$ and $x=0.13$ a transition from the first order character to second order character for the paraelectric to ferroelectric phase transition occurs. For the compositions $x=0.15$, $x=0.20$ and $x=0.25$ the phase transition range broadened with a continuous decrease of the temperature of maximum dielectric permittivity. For the composition $x=0.35$ a relaxor-like behavior with frequency dispersion at the low temperature side of the maximum dielectric permittivity was observed. The phase transition characteristics are reflected in the thermophysical

properties, i.e. thermal conductivity and specific heat capacity. The enthalpy changes, deduced from the specific heat capacity measurements, decrease with increasing zirconium content and the peaks in the excess specific heat capacity shift to lower temperatures coinciding with the paraelectric to ferroelectric phase transition temperatures. With increasing zirconium content the thermal conductivity decreases by ~35 % for x=0.35 compared to BT. Furthermore, glass-like amorphous behavior of the thermal conductivity was observed for x=0.35. The electrocaloric temperature change of the $Ba(Zr_xTi_{1-x})O_3$ system was measured by a direct measurement method. The peaks in the electrocaloric temperature change broadens with increasing zirconium content and a maximum temperature change of ~0.45 K at an electric field change of 2 kV mm^{-1} was found for x=0.13. A maximum caloric figure of merit was obtained for x=0.13 with a value of 1000 J m^{-2} $s^{-1/2}$ due to the largest electrocaloric temperature change of the $Ba(Zr_xTi_{1-x})O_3$ compositions. This is one order of magnitude smaller than the best electrocaloric materials which are the lead containing PMN-PT and PST. The large electric fields that PMN-PT and PST can withstand lead to large electrocaloric temperature changes with a substantial caloric figure of merit, which is comparable to magnetocaloric materials. In comparison the caloric figure of merit of the mechanocaloric NiTi is five times larger than that of magnetocaloric materials. Nevertheless, the right choice of caloric effect for device application also depends on the possible implementation of the driving force, i.e. electric field, magnetic field or mechanical force.

To elaborate on the effect of the paraelectric to ferroelectric phase transition behavior phenomenological theory was used. Ferroelectrics with first order paraelectric to ferroelectric phase transition feature a temperature range above the Curie temperature where the ferroelectric phase can be induced by an electric field. This electric field induced phase transition is possible till the temperature of the liquid-vapor like critical end point. The electric field – temperature phase diagram of BT and the exact position of the critical end point were calculated. First order phase transition character is observed between the Curie temperature and the temperature of the critical end point. At the temperature of the critical end point the phase transition is of second order. The electrocaloric temperature change for BT was calculated for an electric field change from maximum electric field to zero electric field. The value of the maximum electric field was varied from an electric field below the critical electric field, exactly the critical electric field and above the critical electric field. For all three electric field changes, the maximum in the electrocaloric temperature change was found slightly above the Curie temperature. Here, the latent heat of the electric field induced phase transition is the largest, leading to the largest temperature change. Subtracting the temperature change contribution of the latent heat to the temperature change leads to a maximized electrocaloric temperature change at the temperature of the critical end point for the electric field of the critical end point and the electric field above the critical end point. For the electric field below the critical end point no maximum effect is found at the temperature of the critical end point as the electric field is too low to reach the critical end point.

With a suitable set of parameters for the $Ba(Zr_xTi_{1-x})O_3$ system a complete phase diagram was constructed from calculations of the free energy. Furthermore, it was highlighted that the $Ba(Zr_xTi_{1-x})O_3$ system features a tricritical point at $x\sim0.09$, where the first order paraelectric to ferroelectric phase transition goes over into a second order phase transition, and a triple point at $x\sim0.11$, where the paraelectric to ferroelectric phase transition goes over from a cubic to tetragonal transition to a cubic to rhombohedral transition. This zero electric field phase diagram was expanded to the dimension of the electric field and an electric field – composition – temperature phase diagram was calculated. It was demonstrated that the two lines of critical end points converge with the line of second order phase transition into the tricritical point. Over the compositional range of $x=0$ – 0.20 the electrocaloric temperature change was calculated. It was found that the large electrocaloric temperature changes for compositions with a first order paraelectric to ferroelectric phase transition are mainly a result of the large latent heat at the electric field induced phase transition. For the composition at the tricritical point no enhancement in the electrocaloric properties was found. For the composition at the triple point a slight enhancement in the electrocaloric properties was found compared to compositions with slightly more or less zirconium content. The phase transition for the composition at the triple point takes place from a cubic to rhombohedral structure and it was found that the polarization at maximum electric field is larger than for a composition with slightly less zirconium and a phase transition from cubic to tetragonal structure.

The long term stability of the electrocaloric temperature change in $Ba(Zr_{0.20}Ti_{0.80})O_3$ was investigated. After 10^6 cycles an increased leakage current was observed which produced substantial Joule heating and overwhelmed the electrocaloric temperature change. The activation energy of ~0.9 eV of the initial conduction mechanism was in good agreement with the migration enthalpy of oxygen vacancies in oxide ceramics. After cycling the activation energy changed to ~0.23 eV. A drastic change in the leakage current started around 10^5 cycles. During the electric field cycling the defect chemistry is assumed to change due to the migration of oxygen vacancies. The different defect chemistry lead to the enhanced electronic conduction and hence, increased leakage current. It was demonstrated that the oxygen vacancies can be redistributed by thermal annealing. Furthermore, the redistribution can be as well activated by reversal of the electric field, resulting in migration of oxygen vacancies in the opposite direction. To achieve a stable electrocaloric temperature change up to 10^6 cycles, the polarity of the electric field was reversed every 10^5 cycles. Thus a solution was provided to the problem of oxygen vacancy migration that might as well occur in other electrocaloric materials.

5. Acknowledgement

First and foremost, I want to thank my supervisor Dr. Nikola Novak for the help and support throughout the whole Ph.D. time. I learned so much from you about approaching a scientific question. This thesis would not be possible without your excellent guidance and critical review.

My sincere gratitude goes to Prof. Dr. J. Rödel who gave me the opportunity to do my Ph.D. in his research group. I appreciated the steady guidance and the good organization of the research group.

I want to thank Prof. Dr. K. Albe for agreeing to review this work. I want to thank Prof. Dr. B. Albert and Prof. Dr. Y. Genenko for being part of the examination commission.

The German Research Foundation (DFG) is highly acknowledged for funding this work under the grant number NO 1221/2-1.

I want to thank Prof. Dr. G. A. Rossetti Jr. whom I had the pleasure to visit at the University of Connecticut for two month. I learned a lot from you about the thermodynamics of ferroelectrics and got another view on how science and research can work. For this I am really thankful.

I want to thank my collaborators with whom I worked over the past years: Prof. Dr. A. Pramanick, Prof. Dr. H. Zhang, Prof. Dr. S. Patel, Prof. Dr. R. Vaish, Prof. Dr. H. Du, Dr. Y. Ehara, Dr. M. Acosta, Dr. R. Hayati, L. Fulanovic, A. Bradesko and C. Molin.

I want to thank Patrick Breckner, Daniel Isaia and Michael Weber for their contribution in designing the measurement setups. Without your help the development of new setups would not be possible.

I want to thank Gila Völzke for all the help in administrative questions and Michael Heiße for help in the sample preparation.

I want to thank all NAW group members for the nice working environment and especially Jan, Peter and Sebastian for the enjoyable time during and after work.

A special thanks goes to Peter and Sebastian with whom I went through the Bachelor, Master and Ph.D. program. It would not have been the same without you.

I want to thank my family for their love and support during the whole process of education. In particular my wife Shantall who had to deal with a lot of late night and weekend working. Thanks for all your support and patience.

6. References

[1] T. M. Correia, Q. Zhang, *Electrocaloric Materials New Generation of Coolers*, Springer, Berlin, Heidelberg, **2014**.

[2] O. V. Pakhomov, S. F. Karmanenko, A. A. Semenov, A. S. Starkov, A. V. Es'kov, *Technical Physics* **2010**, *55*, 1155-1160.

[3] U. Plaznik, M. Vrabelj, Z. Kutnjak, B. Malič, A. Poredoš, A. Kitanovski, *EPL (Europhysics Letters)* **2015**, *111*, 57009.

[4] Y. V. Sinyavsky, N. D. Pashkov, Y. M. Gorovoy, G. E. Lugansky, L. Shebanov, *Ferroelectrics* **1989**, *90*, 213-217.

[5] Y. V. Sinyavsky, V. M. Brodyansky, *Ferroelectrics* **1992**, *131*, 321-325.

[6] Y. Jia, Y. Sungtaek Ju, *Applied Physics Letters* **2012**, *100*, 242901.

[7] Y. S. Ju, *Journal of Electronic Packaging* **2010**, *132*, 041004.

[8] T. Zhang, X.-S. Qian, H. Gu, Y. Hou, Q. M. Zhang, *Applied Physics Letters* **2017**, *110*, 243503.

[9] H. Gu, X. Qian, H.-J. Ye, Q. M. Zhang, *Applied Physics Letters* **2014**, *105*, 162905.

[10] H. Gu, X. Qian, X. Li, B. Craven, W. Zhu, A. Cheng, S. C. Yao, Q. M. Zhang, *Applied Physics Letters* **2013**, *102*, 122904.

[11] H. Gu, B. Craven, X. Qian, X. Li, A. Cheng, Q. M. Zhang, *Applied Physics Letters* **2013**, *102*, 112901.

[12] P. Blumenthal, C. Molin, S. Gebhardt, A. Raatz, *Ferroelectrics* **2016**, *497*, 1-8.

[13] U. Plaznik, A. Kitanovski, B. Rožič, B. Malič, H. Uršič, S. Drnovšek, J. Cilenšek, M. Vrabelj, A. Poredoš, Z. Kutnjak, *Applied Physics Letters* **2015**, *106*, 043903.

[14] A. Bradeško, D. Juričić, M. Santo Zarnik, B. Malič, Z. Kutnjak, T. Rojac, *Applied Physics Letters* **2016**, *109*, 143508.

[15] D. Sette, A. Asseman, M. Gérard, H. Strozyk, R. Faye, E. Defay, *APL Materials* **2016**, *4*, 091101.

[16] R. Ma, Z. Zhang, K. Tong, D. Huber, R. Kornbluh, Y. S. Ju, Q. Pei, *Science* **2017**, *357*, 1130-1134.

[17] S.-G. Lu, Q. Zhang, *Advanced Materials* **2009**, *21*, 1983-1987.

[18] Z. Kutnjak, B. Rožič, R. Pirc, *Wiley Encyclopedia of Electrical and Electronics Engineering* **2015**, *1–19*.

[19] X. Moya, S. Kar-Narayan, N. D. Mathur, *Nature Materials* **2014**, *13*, 439-450.

[20] X. Moya, E. Defay, V. Heine, N. D. Mathur, *Nature Physics* **2015**, *11*, 202-205.

[21] J. F. Scott, *Annual Review of Materials Research* **2011**, *41*, 229-240.

[22] S. Crossley, N. D. Mathur, X. Moya, *AIP Advances* **2015**, *5*, 067153.

[23] S. Kar-Narayan, N. D. Mathur, *Ferroelectrics* **2012**, *433*, 107-110.

[24] M. Ožbolt, A. Kitanovski, J. Tušek, A. Poredoš, *International Journal of Refrigeration* **2014**, *40*, 174-188.

[25] M. Ožbolt, A. Kitanovski, J. Tušek, A. Poredoš, *International Journal of Refrigeration* **2014**, *37*, 16-27.

[26] S. Fähler, U. K. Rößler, O. Kastner, J. Eckert, G. Eggeler, H. Emmerich, P. Entel, S. Müller, E. Quandt, K. Albe, *Advanced Engineering Materials* **2012**, *14*, 10-19.

[27] S. P. Alpay, J. Mantese, S. Trolier-McKinstry, Q. Zhang, R. W. Whatmore, *MRS Bulletin* **2014**, *39*, 1099-1111.

[28] Y. Liu, G. Zhang, Q. Li, L. Bellaiche, J. F. Scott, B. Dkhil, Q. Wang, *Physical Review B* **2016**, *94*.

[29] X. Li, S.-G. Lu, X.-Z. Chen, H. Gu, X. Qian, Q. M. Zhang, *Journal of Materials Chemistry C* **2013**, *1*, 23-37.

[30] M. Valant, *Progress in Materials Science* **2012**, *57*, 980-1009.

[31] W. Thomson, M. A., *The London, Edinburgh, and Dublin Philosophical Magazine and Journal of Science* **1877**, *5*, 4-27.

[32] R. Straubel, *Nachrichten von der Gesellschaft der Wissenschaften zu Göttingen, Mathematisch-Physikalische Klasse,* **1902**, 161-164.

[33] F. Lange, Dissertation thesis, philosophische Fakultät zu Jena (Jena), **1905**.

[34] W. Thomson, M. A., *Philosophical Magazine* **1893**, *5*, 453.

[35] W. Voigt, *Abhandlungen der Königlichen Gesellschaft der Wissenschaften in Göttingen* **1890**.

[36] W. Voigt, *Wiedemann'sche Annalen.* **1895**, *55*, 701.

[37] E. Riecke, *Wiedemann'sche Annalen* **1893**, *49*, 430.

[38] W. Voigt, *Lehrbuch der Kristallphysik*, B. G. Teubner, Leipzig und Berlin, **1910**.

[39] F. Pockels, *Beziehungen zwischen elektrostatischen und magnetostatischen Zustandsänderungen einerseits und elastischen und thermischen andererseits,* B. G. Teubner, Leipzig, **1906**.

[40] J. Valasek, *Physical Review* **1921**, *17*, 475-481.

[41] P. Kobeko, J. Kurtschatov, *Zeitschrift für Physik A Hadrons and Nuclei* **1930**, *66*, 192-205.

[42] A. Kikuchi, E. Sawaguchi, *Journal of the Physical Society of Japan* **1964**, *19*, 1497-1498.

[43] G. Lombardo, R. O. Pohl, *Physical Review Letters* **1965**, *15*, 291-293.

[44] I. W. Shepherd, *Journal of Physics and Chemistry of Solids* **1967**, *28*, 2027-2051.

[45] R. O. Pohl, V. L. Taylor, W. M. Goubau, *Physical Review* **1969**, *178*, 1431-1436.

[46] S. B. Lang, *Ferroelectrics* **1976**, *11*, 519-523.

[47] W. N. Lawless, *Physical Review B* **1977**, *16*, 433-439.

[48] W. N. Lawless, A. J. Morrow, *Ferroelectrics* **1977**, *15*, 159-165.

[49] R. Radebaugh, W. N. Lawless, J. D. Siegwarth, A. J. Morrow, *Cryogenics* **1979**.

[50] J. D. Childress, *Journal of Applied Physics* **1962**, *33*, 1793-1798.

[51] P. D. Thacher, *Journal of Applied Physics* **1968**, *39*, 1996-2002.

[52] R. B. Olsen, W. F. Butler, D. A. Payne, B. A. Tuttle, P. C. Held, *Physical Review Letters* **1980**, *45*, 1436-1438.

[53] B. A. Tuttle, D. A. Payne, *Ferroelectrics* **1981**, *37*, 603-606.

[54] E. Birks, *Physica Status Solidi (a)* **1986**, *94*, 523.

[55] E. Birks, L. Shebanov, A. Sternberg, *Ferroelectrics* **1986**, *69*, 125-129.

[56] L. A. Shebanov, E. H. Birks, K. J. Borman, A. R. Sternberg, *Ferroelectrics* **1989**, *94*, 305-305.

[57] L. Shebanov, K. Borman, *Ferroelectrics* **1992**, *127*, 143-148.

[58] Y. V. Sinyavsky, *Chemical and Petroleum Engineering* **1995**, *31*.

[59] Y. V. Sinyavsky, *Chemical and Petroleum Engineering* **1995**, *31*.

[60] D. Q. Xiao, Y. C. Wang, R. L. Zhang, S. Q. Peng, J. G. Zhu, B. Yang, *Materials Chemistry and Physics* **1998**, *57*, 182-185.

[61] R. Zhang, S. Peng, D. Xiao, Y. Wang, B. Yang, J. Zhu, P. Yu, W. Zhang, *Crystal Research and Technology: Journal of Experimental and Industrial Crystallography* **1998**, *33*, 827-832.

[62] L. Shebanovs, K. Borman, W. N. Lawless, A. Kalvane, *Ferroelectrics* **2002**, *273*, 137-142.

[63] A. S. Mischenko, Q. Zhang, J. F. Scott, R. W. Whatmore, N. D. Mathur, *Science* **2006**, *311*, 1270-1271.

[64] B. Neese, B. Chu, S. G. Lu, Y. Wang, E. Furman, Q. M. Zhang, *Science* **2008**, *321*, 821-823.

[65] X. Moya, E. Defay, N. D. Mathur, S. Hirose, *MRS Bulletin* **2018**, *43*, 291-294.

[66] M. Valant, A.-K. Axelsson, F. Le Goupil, N. M. Alford, *Materials Chemistry and Physics* **2012**, *136*, 277-280.

[67] S. Kar-Narayan, N. D. Mathur, *Applied Physics Letters* **2009**, *95*, 242903.

[68] S. Crossley, J. R. McGinnigle, S. Kar-Narayan, N. D. Mathur, *Applied Physics Letters* **2014**, *104*, 082909.

[69] S. Hirose, T. Usui, S. Crossley, B. Nair, A. Ando, X. Moya, N. D. Mathur, *APL Materials* **2016**, *4*, 064105.

[70] Y. Liu, H. Strozyk, B. Dkhil, E. Defay, *Applied Physics Letters* **2016**, *109*, 212902.

[71] Y. Liu, B. Dkhil, E. Defay, *ACS Energy Letters* **2016**, *1*, 521-528.

[72] R. Faye, H. Strozyk, B. Dkhil, E. Defay, *Journal of Physics D: Applied Physics* **2017**, *50*, 464002.

[73] T. Maiti, R. Guo, A. S. Bhalla, *Journal of the American Ceramic Society* **2008**, *91*, 1769-1780.

[74] J. Rödel, W. Jo, K. T. P. Seifert, E.-M. Anton, T. Granzow, D. Damjanovic, *Journal of the American Ceramic Society* **2009**, *92*, 1153-1177.

[75] T. Takenaka, H. Nagata, *Journal of the European Ceramic Society* **2005**, *25*, 2693-2700.

[76] M. D. Maeder, D. Damjanovic, N. Setter, *Journal of Electroceramics* **2004**, *13*, 385-392.

[77] D. Hennings, *International Journal of High Technology Ceramics* **1987**, *3*, 91-111.

[78] A. Tagantsev, V. Sherman, K. Astafiev, J. Venkatesh, N. Setter, *Journal of Electroceramics* **2003**, *11*, 5-66.

[79] J. F. Scott, *Science* **2007**, *315*, 954-959.

[80] R. Whatmore, *Reports on Progress in Physics* **1986**, *49*, 1335.

[81] J. Fraden, *Handbook of Modern Sensors: Physics, Designs, and Applications*, Springer Science & Business Media, **2004**.

[82] M. Lee, R. Guo, A. S. Bhalla, *Journal of Electroceramics* **1998**, *2*, 229-242.

[83] O. Auciello, J. F. Scott, R. Ramesh, *Physics Today* **1998**, *51*, 22-27.

[84] H. Ishiwara, M. Okuyama, Y. Arimoto, *Ferroelectric Random Access Memories: Fundamentals and Applications*, Springer Science & Business Media, **2004**.

[85] H. Ueoka, M. Yodogawa, *IEEE Transactions on Manufacturing Technology* **1974**, *3*, 77-82.

[86] C. Bowen, H. Kim, P. Weaver, S. Dunn, *Energy & Environmental Science* **2014**, *7*, 25-44.

[87] S. P. Beeby, M. J. Tudor, N. White, *Measurement Science and Technology* **2006**, *17*, R175.

[88] K. Uchino, *Ferroelectric Devices 2nd Edition*, CRC Press, **2009**.

[89] M. E. Lines, A. M. Glass, *Principles and Applications of Ferroelectrics and Related Materials*, Oxford University Press, **1977**.

[90] F. Jona, G. Shirane, *Ferroelectric Crystals,* Pergamon, **1962**.

[91] B. Jaffe, W. R. Cook, H. Jaffe, *Piezoelectric Ceramics,* Academic Press, London and New York, **1971**.

[92] G. A. Samara, *Ferroelectricity Revisited—Advances in Materials and Physics,* Solid State Physics, Academic Press, **2001**.

[93] R. E. Newnham, *Properties of Materials: Anisotropy, Symmetry, Structure*, Oxford University Press, **2005**.

[94] B. A. Strukov, A. P. Levanyuk, *Ferroelectric Phenomena in Crystals: Physical Foundations*, Springer Science & Business Media, **2012**.

[95] C. W. Ahn, C.-H. Hong, B.-Y. Choi, H.-P. Kim, H.-S. Han, Y. Hwang, W. Jo, K. Wang, J.-F. Li, J.-S. Lee, *Journal of the Korean Physical Society* **2016**, *68*, 1481-1494.

[96] D. Damjanovic, *Reports on Progress in Physics* **1998**, *61*, 1267.

[97] K. Uchino, S. Nomura, L. E. Cross, R. E. Newnham, S. J. Jang, *Journal of Materials Science* **1981**, *16*, 569-578.

[98] A. F. Devonshire, *The London, Edinburgh, and Dublin Philosophical Magazine and Journal of Science* **1949**, *40*, 1040-1063.

[99] A. F. Devonshire, *The London, Edinburgh, and Dublin Philosophical Magazine and Journal of Science* **1951**, *42*, 1065-1079.

[100] L. E. Cross, *Ferroelectrics* **1987**, *76*, 241-267.

[101] G. Smolenskii, A. Agranovskaya, *Zhurnal tekhniceskoj fiziki* **1958**, *28*.
[102] G. Smolenskii, V. Isupov, A. Agranovskaya, S. Popov, *Soviet Physics-Solid State* **1961**, *2*, 2584-2594.
[103] N. Setter, L. Cross, *Journal of Applied Physics* **1980**, *51*, 4356-4360.
[104] N. Setter, L. Cross, *Journal of Materials Science* **1980**, *15*, 2478-2482.
[105] V. Kirillov, V. Isupov, *Ferroelectrics* **1973**, *5*, 3-9.
[106] H. Vogel, *Physikalische Zeitschrift* **1921**, *22*, 645-646.
[107] G. S. Fulcher, *Journal of the American Ceramic Society* **1925**, *8*, 339-355.
[108] G. Tammann, W. Hesse, *Zeitschrift für anorganische und allgemeine Chemie* **1926**, *156*, 245-257.
[109] V. K. Pecharsky, K. A. Gschneidner Jr, *Journal of Magnetism and Magnetic Materials* **1999**, *200*, 44-56.
[110] R. Pirc, Z. Kutnjak, R. Blinc, Q. M. Zhang, *Journal of Applied Physics* **2011**, *110*, 074113.
[111] B. Rožič, M. Kosec, H. Uršič, J. Holc, B. Malič, Q. M. Zhang, R. Blinc, R. Pirc, Z. Kutnjak, *Journal of Applied Physics* **2011**, *110*, 064118.
[112] R. Pirc, B. Rožič, J. Koruza, B. Malič, Z. Kutnjak, *EPL (Europhysics Letters)* **2014**, *107*, 17002.
[113] J. Grindlay, *An Introduction to the Phenomenological Theory of Ferroelectricity*, Pergamon, Oxford, **1970**.
[114] E. Birks, M. Dunce, A. Sternberg, *Ferroelectrics* **2010**, *400*, 336-343.
[115] N. Novak, R. Pirc, Z. Kutnjak, *Physical Review B* **2013**, *87*.
[116] N. Novak, Z. Kutnjak, R. Pirc, *EPL (Europhysics Letters)* **2013**, *103*, 47001.
[117] T. Mitsui, E. Nakamura, M. Tokunaga, *Ferroelectrics* **1998**, *5*, 185-196.
[118] G. Akcay, S. P. Alpay, G. A. Rossetti Jr., J. F. Scott, *Journal of Applied Physics* **2008**, *103*, 024104.
[119] G. Sebald, S. Pruvost, L. Seveyrat, L. Lebrun, D. Guyomar, B. Guiffard, *Journal of the European Ceramic Society* **2007**, *27*, 4021-4024.
[120] G. Lin, X. Xiong, J. Zhang, Q. Wei, *Journal of Thermal Analysis and Calorimetry* **2005**, *81*, 41-44.
[121] Z. Kutnjak, J. Petzelt, R. Blinc, *Nature* **2006**, *441*, 956-959.
[122] J. Peräntie, J. Hagberg, A. Uusimäki, H. Jantunen, *Applied Physics Letters* **2009**, *94*, 102903.
[123] E. Sapper, N. Novak, W. Jo, T. Granzow, J. Rödel, *Journal of Applied Physics* **2014**, *115*, 194104.
[124] D. Damjanovic, *IEEE Transactions on Ultrasonics, Ferroelectrics, and Frequency Control* **2009**, *56*, 1574-1585.
[125] H. Fu, R. E. Cohen, *Nature* **2000**, *403*, 281.
[126] A. A. Heitmann, G. A. Rossetti Jr., *Journal of the American Ceramic Society* **2014**, *97*, 1661-1685.
[127] B. Jaffe, R. Roth, S. Marzullo, *Journal of Applied Physics* **1954**, *25*, 809-810.
[128] J. Kelly, M. Leonard, C. Tantigate, A. Safari, *Journal of the American Ceramic Society* **1997**, *80*, 957-964.

[129] W. Jo, J. E. Daniels, J. L. Jones, X. Tan, P. A. Thomas, D. Damjanovic, J. Rödel, *Journal of Applied Physics* **2011**, *109*, 014110.

[130] Y. Hiruma, R. Aoyagi, H. Nagata, T. Takenaka, *Japanese Journal of Applied Physics* **2004**, *43*, 7556.

[131] W. Liu, X. Ren, *Physical Review Letters* **2009**, *103*, 257602.

[132] T. Karaki, T. Katayama, K. Yoshida, S. Maruyama, M. Adachi, *Japanese Journal of Applied Physics* **2013**, *52*, 09KD11.

[133] Y. Bai, X. Han, X. C. Zheng, L. Qiao, *Scientific Reports* **2013**, *3*, 2895.

[134] J. W. McPherson, K. Jinyoung, A. Shanware, H. Mogul, J. Rodriguez, *IEEE Transactions on Electron Devices* **2003**, *50*, 1771-1778.

[135] J. McPherson, J. Kim, A. Shanware, H. Mogul, *Applied Physics Letters* **2003**, *82*, 2121-2123.

[136] G. Suchaneck, G. Gerlach, *Acta Physica Polonica A* **2018**, *133*, 1003-1005.

[137] S. Kar-Narayan, N. D. Mathur, *Journal of Physics D: Applied Physics* **2010**, *43*, 032002.

[138] S. Kar-Narayan, S. Crossley, X. Moya, V. Kovacova, J. Abergel, A. Bontempi, N. Baier, E. Defay, N. D. Mathur, *Applied Physics Letters* **2013**, *102*, 032903.

[139] E. Defay, S. Crossley, S. Kar-Narayan, X. Moya, N. D. Mathur, *Advanced Materials* **2013**, *25*, 3337-3342.

[140] B. M. Foley, E. A. Paisley, C. DiAntonio, T. Chavez, M. Blea-Kirby, G. Brennecka, J. T. Gaskins, J. F. Ihlefeld, P. E. Hopkins, *Journal of Applied Physics* **2017**, *121*, 205104.

[141] P. E. Hopkins, C. Adamo, L. Ye, B. D. Huey, S. R. Lee, D. G. Schlom, J. F. Ihlefeld, *Applied Physics Letters* **2013**, *102*, 121903.

[142] J. F. Ihlefeld, B. M. Foley, D. A. Scrymgeour, J. R. Michael, B. B. McKenzie, D. L. Medlin, M. Wallace, S. Trolier-McKinstry, P. E. Hopkins, *Nano Letters* **2015**, *15*, 1791-1795.

[143] J.-J. Wang, Y. Wang, J. F. Ihlefeld, P. E. Hopkins, L.-Q. Chen, *Acta Materialia* **2016**, *111*, 220-231.

[144] B. A. Strukov, A. A. Belov, *Phase Transitions* **1994**, *51*, 175-197.

[145] A. J. H. Mante, J. Volger, *Physics Letters* **1966**, *24A*, 139-140.

[146] M. Tachibana, T. Kolodiazhnyi, E. Takayama-Muromachi, *Applied Physics Letters* **2008**, *93*.

[147] M. Tachibana, K. Sasame, H. Kawaji, T. Atake, E. Takayama-Muromachi, *Physical Review B* **2009**, *80*.

[148] M. Tachibana, E. Takayama-Muromachi, *Physical Review B* **2009**, *79*, 100104.

[149] I. Yoshida, *Journal of the Physical Society of Japan* **1960**, *15*, 2211-2219.

[150] K. Morimoto, S. Sawai, K. Hisano, T. Yamamoto, *Thermochimica Acta* **2006**, *442*, 14-17.

[151] H. Uršič, M. Vrabelj, L. Fulanović, A. Bradeško, S. Drnovsek, B. Malič, *Journal of Microelectronics, Electronic Components and Materials* **2015**, *45*, 260-265.

[152] E. Martinez, S. Garcia, E. Marin, O. Vasallo, G. Pena-Rodriguez, A. Calderon, J. Siqueiros, *Journal of Materials Science* **2004**, *39*, 1233-1239.

[153] Y. He, *Thermochimica Acta* **2004**, 419, 135-141.

[154] S. Todd, R. Lorenson, *Journal of the American Chemical Society* **1952**, *74*, 2043-2045.

[155] Y. Bai, K. Ding, G.-P. Zheng, S.-Q. Shi, L. Qiao, *Physica Status Solidi (a)* **2012**, *209*, 941-944.

[156] D. C. Lupascu, J. Rödel, *Advanced Engineering Materials* **2005**, *7*, 882-898.

[157] W. Pan, C. F. Yue, O. Tosyali, *Journal of the American Ceramic Society* **1992**, *75*, 1534-1540.

[158] C. Verdier, D. C. Lupascu, J. Rödel, *Applied Physics Letters* **2002**, *81*, 2596-2598.

[159] C. Verdier, D. C. Lupascu, J. Rödel, *Journal of the European Ceramic Society* **2003**, *23*, 1409-1415.

[160] D. Wang, Y. Fotinich, G. P. Carman, *Journal of Applied Physics* **1998**, *83*, 5342-5350.

[161] T. Baiatu, R. Waser, K. H. Härdtl, *Journal of the American Ceramic Society* **1990**, *73*, 1663-1673.

[162] R. Waser, T. Baiatu, K. H. Härdtl, *Journal of the American Ceramic Society* **1990**, *73*, 1645-1653.

[163] R. Waser, T. Baiatu, K. H. Härdtl, *Journal of the American Ceramic Society* **1990**, *73*, 1654-1662.

[164] J. Rödel, G. Tomandl, *Journal of Materials Science* **1984**, *19*, 3515-3523.

[165] T. J. Bayer, J.-J. Wang, J. J. Carter, A. Moballegh, J. Baker, D. L. Irving, E. C. Dickey, L.-Q. Chen, C. A. Randall, *Acta Materialia* **2016**, *117*, 252-261.

[166] J.-J. Wang, H.-B. Huang, T. J. Bayer, A. Moballegh, Y. Cao, A. Klein, E. C. Dickey, D. L. Irving, C. A. Randall, L.-Q. Chen, *Acta Materialia* **2016**, *108*, 229-240.

[167] Y. Cao, J. Shen, C. Randall, L.-Q. Chen, D. Johnson, *Journal of the American Ceramic Society* **2014**, *97*, 3568-3575.

[168] H. Ossmer, C. Slouka, L. Andrejs, P. Blaha, G. Friedbacher, J. Fleig, *Solid State Ionics* **2015**, *281*, 49-59.

[169] S. Rodewald, J. Fleig, J. Maier, *Journal of the American Ceramic Society* **2000**, *83*, 1969-1976.

[170] S. Lee, G. A. Rossetti Jr., Z.-K. Liu, C. A. Randall, *Journal of Applied Physics* **2009**, *105*, 093519.

[171] B. Wul, *Nature* **1945**, *156*, 480.

[172] P. R. Coursey, K. Brand, *Nature* **1946**, *157*, 297.

[173] H. Jaffe, *Industrial & Engineering Chemistry* **1950**, *42*, 264-268.

[174] G. Shirane, K. Suzuki, A. Takeda, *Journal of the Physical Society of Japan* **1952**, *7*, 12-18.

[175] J. Harada, T. Pedersen, Z. Barnea, *Acta Crystallographica Section A: Crystal Physics, Diffraction, Theoretical and General Crystallography* **1970**, *26*, 336-344.

[176] A. L. Young, G. E. Hilmas, S. C. Zhang, R. W. Schwartz, *Journal of Materials Science* **2007**, *42*, 5613-5619.

[177] R. Gerson, T. C. Marshall, *Journal of Applied Physics* **1959**, *30*, 1650-1653.

[178] A. S. Mischenko, Q. Zhang, R. W. Whatmore, J. F. Scott, N. D. Mathur, *Applied Physics Letters* **2006**, *89*.

[179] G. Akcay, S. P. Alpay, J. V. Mantese, G. A. Rossetti Jr., *Applied Physics Letters* **2007**, *90*, 252909.
[180] G. Akcay, S. P. Alpay, G. A. Rossetti Jr., J. F. Scott, *Journal of Applied Physics* **2008**, *103*.
[181] J. H. Qiu, Q. Jiang, *Journal of Applied Physics* **2009**, *105*, 034110.
[182] H.-X. Cao, Z.-Y. Li, *Journal of Applied Physics* **2009**, *106*, 094104.
[183] Y. Bai, K. Ding, G.-P. Zheng, S.-Q. Shi, J.-L. Cao, L. Qiao, *AIP Advances* **2012**, *2*, 022162.
[184] X. Moya, E. Stern-Taulats, S. Crossley, D. Gonzalez-Alonso, S. Kar-Narayan, A. Planes, L. Manosa, N. D. Mathur, *Advanced Materials* **2013**, *25*, 1360-1365.
[185] J. Volger, *Philips Research Reports* **1952**, *7*, 21-27.
[186] H. F. Blattner, Dissertation thesis, ETH Zurich **1949**.
[187] G. Shirane, A. Takeda, *Journal of the Physical Society of Japan* **1952**, *7*, 1-4.
[188] V. Egorov, E. Smirnova, V. Lemanov, *Physics of the Solid State* **2007**, *49*, 1528-1531.
[189] S. Kar-Narayan, N. D. Mathur, *Journal of Physics D: Applied Physics* **2010**, *43*.
[190] Y. Bai, G. Zheng, S. Shi, *Applied Physics Letters* **2010**, *96*, 192902.
[191] X. Chou, J. Zhai, H. Jiang, X. Yao, *Journal of Applied Physics* **2007**, *102*, 084106.
[192] Y.-B. Ma, C. Molin, V. V. Shvartsman, S. Gebhardt, D. C. Lupascu, K. Albe, B.-X. Xu, *Journal of Applied Physics* **2017**, *121*, 024103.
[193] C. Laulhé, F. Hippert, R. Bellissent, A. Simon, G. J. Cuello, *Physical Review B* **2009**, *79*, 064104.
[194] D. Hennings, A. Schnell, G. Simon, *Journal of the American Ceramic Society* **1982**, *65*, 539-544.
[195] J. Li, H. Kakemoto, S. Wada, T. Tsurumi, H. Kawaji, *Journal of Applied Physics* **2006**, *100*, 024106.
[196] J. Li, H. Kakemoto, S. Wada, T. Tsurumi, *Ferroelectrics* **2007**, *356*, 134-139.
[197] P. W. Rehrig, S.-E. Park, S. Trolier-McKinstry, G. L. Messing, B. Jones, T. R. Shrout, *Journal of Applied Physics* **1999**, *86*, 1657-1661.
[198] Z. Yu, C. Ang, R. Guo, A. S. Bhalla, *Journal of Applied Physics* **2002**, *92*, 1489-1493.
[199] Z. Yu, C. Ang, R. Guo, A. S. Bhalla, *Journal of Applied Physics* **2002**, *92*, 2655-2657.
[200] T. Maiti, R. Guo, A. S. Bhalla, *Ferroelectrics* **2011**, *425*, 4-26.
[201] A. K. Kalyani, A. Senyshyn, R. Ranjan, *Journal of Applied Physics* **2013**, *114*, 014102.
[202] C. Kajtoch, W. Bak, B. Garbarz-Glos, K. Stanuch, W. Tejchman, K. Mroczka, T. Czeppe, *Ferroelectrics* **2014**, *463*, 130-136.
[203] J. N. Lin, T. B. Wu, *Journal of Applied Physics* **1990**, *68*, 985-993.
[204] L. Dong, D. S. Stone, R. S. Lakes, *Journal of Applied Physics* **2012**, *111*, 084107.
[205] R. Farhi, M. El Marssi, A. Simon, J. Ravez, *The European Physical Journal B* **1999**, *9*, 599-604.
[206] P. Sciau, G. Calvarin, J. Ravez, *Solid State Communications* **2000**, *113*, 77-82.
[207] A. Simon, J. Ravez, *Ferroelectrics* **2000**, *240*, 1601-1608.
[208] J. Ravez, A. Simon, *Journal of Solid State Chemistry* **2001**, *162*, 260-265.
[209] A. Simon, J. Ravez, M. Maglione, *Journal of Physics: Condensed Matter* **2004**, *16*, 963.

[210] P. Sciau, A. M. Castagnos, *Ferroelectrics* **2002**, *270*, 259-264.

[211] J. Kreisel, P. Bouvier, M. Maglione, B. Dkhil, A. Simon, *Physical Review B* **2004**, *69*.

[212] C. Laulhé, F. Hippert, J. Kreisel, M. Maglione, A. Simon, J. L. Hazemann, V. Nassif, *Physical Review B* **2006**, *74*.

[213] A. A. Bokov, M. Maglione, Z. G. Ye, *Journal of Physics: Condensed Matter* **2007**, *19*, 092001.

[214] S. Ke, H. Fan, H. Huang, H. L. W. Chan, S. Yu, *Journal of Applied Physics* **2008**, *104*, 034108.

[215] V. V. Shvartsman, J. Zhai, W. Kleemann, *Ferroelectrics* **2009**, *379*, 77-85.

[216] W. Kleemann, J. Dec, S. Miga, *Phase Transitions* **2014**, *88*, 234-244.

[217] W. Kleemann, S. Miga, J. Dec, J. Zhai, *Applied Physics Letters* **2013**, *102*, 232907.

[218] A. R. Akbarzadeh, S. Prosandeev, E. J. Walter, A. Al-Barakaty, L. Bellaiche, *Physical Review Letters* **2012**, *108*, 257601.

[219] S. Prosandeev, D. Wang, A. R. Akbarzadeh, B. Dkhil, L. Bellaiche, *Physical Review Letters* **2013**, *110*, 207601.

[220] D. Sherrington, *Physical Review Letters* **2013**, *111*, 227601.

[221] D. Nuzhnyy, J. Petzelt, M. Savinov, T. Ostapchuk, V. Bovtun, M. Kempa, J. Hlinka, V. Buscaglia, M. T. Buscaglia, P. Nanni, *Physical Review B* **2012**, *86*.

[222] J. Petzelt, D. Nuzhnyy, V. Bovtun, M. Kempa, M. Savinov, S. Kamba, J. Hlinka, *Phase Transitions* **2014**, *88*, 320-332.

[223] R. Pirc, Z. Kutnjak, *Physical Review B* **2014**, *89*.

[224] C. Filipič, Z. Kutnjak, R. Pirc, G. Canu, J. Petzelt, *Physical Review B* **2016**, *93*.

[225] H.-J. Ye, X.-S. Qian, D.-Y. Jeong, S. Zhang, Y. Zhou, W.-Z. Shao, L. Zhen, Q. M. Zhang, *Applied Physics Letters* **2014**, *105*, 152908.

[226] Y. Hou, L. Yang, X. Qian, T. Zhang, Q. M. Zhang, *Applied Physics Letters* **2016**, *108*, 133501.

[227] Y. Hou, L. Yang, X. Zhao, Q. M. Zhang, *Journal of Alloys and Compounds* **2017**, *724*, 8-13.

[228] X.-S. Qian, H.-J. Ye, Y.-T. Zhang, H. Gu, X. Li, C. A. Randall, Q. M. Zhang, *Advanced Functional Materials* **2014**, *24*, 1300-1305.

[229] H. Maiwa, *Japanese Journal of Applied Physics* **2015**, *54*, 10NB08.

[230] Y. Bai, X. Han, K. Ding, L. Qiao, *Energy Technology* **2017**, *5*, 703-707.

[231] M. Sanlialp, V. V. Shvartsman, R. Faye, M. O. Karabasov, C. Molin, S. Gebhardt, E. Defay, D. C. Lupascu, *Review of Scientific Instruments* **2018**, *89*, 034903.

[232] M. Marathe, D. Renggli, M. Sanlialp, M. O. Karabasov, V. V. Shvartsman, D. C. Lupascu, A. Grünebohm, C. Ederer, *Physical Review B* **2017**, *96*.

[233] C. B. Sawyer, C. H. Tower, *Physical Review* **1930**, *35*, 269-273.

[234] C. W. Garland, in *Experimental Study of Physical Properties and Phase Transitions* (Ed.: S. Kumar), Cambridge University Press, Cambridge, **2001**, pp. 240-294.

[235] Y. A. Kraftmakher, *Zurnal prikladnoj mechaniki i techniyeceskoj fiziki* **1962**, *5*, 176-180.

[236] P. F. Sullivan, G. Seidel, *Physical Review* **1968**, *173*, 679-685.

[237] W. J. Parker, R. J. Jenkins, C. P. Butler, G. L. Abbott, *Journal of Applied Physics* **1961**, *32*, 1679-1684.

[238] H. Carslaw, J. Jaeger, *Conduction of Heat in Solids,* Oxford Science Publications, Oxford, England, **1959**.

[239] G. Mader, H. Meixner, P. Kleinschmidt, *Journal of Applied Physics* **1984**, *56*, 2832-2836.

[240] D. S. Smith, N. Ghayoub, I. Charissou, O. Bellon, P. Abelard, *Journal of American Ceramic Society* **1998**, *81*, 1789-1796.

[241] J. H. Lienhard IV, J. H. Lienhard V, *A Heat Transfer Textbook,* Phlogiston Press, Cambridge, USA, **2008**.

[242] Y. A. Cengel, *Heat Transfer: A Practical Approach*, McGraw-Hill, New York, **1998**.

[243] T. L. Bergman, F. P. Incropera, D. P. DeWitt, A. S. Lavine, *Fundamentals of Heat and Mass Transfer*, John Wiley & Sons, **2011**.

[244] B. Rožič, B. Malič, H. Uršič, J. Holc, M. Kosec, B. Neese, Q. M. Zhang, Z. Kutnjak, *Ferroelectrics* **2010**, *405*, 26-31.

[245] J. Peräntie, J. Hagberg, A. Uusimäki, H. Jantunen, *Physical Review B* **2010**, *82*, 134119.

[246] F. L. Goupil, A. Berenov, A.-K. Axelsson, M. Valant, N. M. Alford, *Journal of Applied Physics* **2012**, *111*, 124109.

[247] C. Molin, J. Peräntie, F. Le Goupil, F. Weyland, M. Sanlialp, N. Stingelin, N. Novak, D. C. Lupascu, S. Gebhardt, *Journal of the American Ceramic Society* **2017**, *100*, 2885-2892.

[248] F. Weyland, R. Perez-Moyet, G. A. Rossetti Jr., N. Novak, *Energy Technology* **2018**, *6*, 1512-1518.

[249] O. Noblanc, P. Gaucher, G. Calvarin, *Journal of Applied Physics* **1996**, *79*, 4291-4297.

[250] R. Berman, *Thermal Conduction in Solids*, Clarendon Press, **1976**.

[251] E. Steigmeier, *Physical Review* **1968**, *168*, 523.

[252] V. Buscaglia, S. Tripathi, V. Petkov, M. Dapiaggi, M. Deluca, A. Gajovic, Y. Ren, *Journal of Physics: Condensed Matter* **2014**, *26*, 065901.

[253] R. D. Shannon, *Acta Crystallographica Section A: Crystal Physics, Diffraction, Theoretical and General Crystallography* **1976**, *32*, 751-767.

[254] T. Verbitskaia, G. Zhdanov, I. N. Venevtsev, S. Soloviev, *Soviet Physics Crystallography* **1958**, *3*, 182-192.

[255] M. H. Frey, D. A. Payne, *Physical Review B* **1996**, *54*, 3158-3168.

[256] M. Acosta, N. Novak, V. Rojas, S. Patel, R. Vaish, J. Koruza, G. A. Rossetti Jr., J. Rödel, *Applied Physics Reviews* **2017**, *4*, 041305.

[257] G. Arlt, *Ferroelectrics* **1990**, *104*, 217-227.

[258] H. Tsukasaki, Y. Inoue, Y. Koyama, *Ferroelectrics* **2014**, *460*, 18-33.

[259] M. Huntelaar, E. Cordfunke, R. Van der Laan, *Thermochimica Acta* **1996**, *274*, 101-111.

[260] J. L. Haas Jr, J. R. Fisher, *American Journal of Science* **1976**, *276*.

[261] M. V. Gorev, V. S. Bondarev, I. N. Flerov, P. Sciau, J. M. Savariault, *Physics of the Solid State* **2005**, *47*, 2304-2308.

[262] M. Nagasawa, H. Kawaji, T. Tojo, T. Atake, *Physical Review B* **2006**, *74*.

[263] M. Gorev, I. Flerov, V. Bondarev, P. Sciau, *Journal of Experimental and Theoretical Physics* **2003**, *96*, 531-537.

[264] B. Hanna, R. G. Bohn, *Journal of the American Ceramic Society* **1991**, *74*, 3035-3038.

[265] D. Cahill, J. Olson, H. E. Fischer, S. Watson, R. Stephens, R. Tait, T. Ashworth, R. Pohl, *Physical Review B* **1991**, *44*, 12226.

[266] C. Choy, D. Greig, *Journal of Physics C: Solid State Physics* **1975**, *8*, 3121.

[267] J. Tušek, K. Engelbrecht, L. P. Mikkelsen, N. Pryds, *Journal of Applied Physics* **2015**, *117*, 124901.

[268] C. Zanotti, P. Giuliani, A. Chrysanthou, *Intermetallics* **2012**, *24*, 106-114.

[269] S. Y. Dan'Kov, A. Tishin, V. Pecharsky, K. Gschneidner, *Physical Review B* **1998**, *57*, 3478.

[270] P. Jacobsson, B. Sundqvist, *Physical Review B* **1989**, *40*, 9541-9551.

[271] A. Taubel, T. Gottschall, M. Fries, S. Riegg, C. Soon, K. P. Skokov, O. Gutfleisch, *Physica Status Solidi (b)* **2018**, *255*, 1700331.

[272] B. Zhang, X. X. Zhang, S. Y. Yu, J. L. Chen, Z. X. Cao, G. H. Wu, *Applied Physics Letters* **2007**, *91*, 012510.

[273] K. Engelbrecht, C. R. H. Bahl, K. K. Nielsen, *International Journal of Refrigeration* **2011**, *34*, 1132-1140.

[274] S. Fujieda, Y. Hasegawa, A. Fujita, K. Fukamichi, *Journal of Applied Physics* **2004**, *95*, 2429-2431.

[275] X. Moya, B. Nair, in *MRS Fall Meeting & Exhibit*, Materials Research Society, Boston, USA, **2018**.

[276] M. Vrabelj, H. Uršič, Z. Kutnjak, B. Rožič, S. Drnovšek, A. Benčan, V. Bobnar, L. Fulanović, B. Malič, *Journal of the European Ceramic Society* **2016**, *36*, 75-80.

[277] A. Bell, L. Cross, *Ferroelectrics* **1984**, *59*, 197-203.

[278] A. J. Bell, *Journal of Applied Physics* **2001**, *89*, 3907-3914.

[279] Y. Li, L. Cross, L. Chen, *Journal of Applied Physics* **2005**, *98*, 064101.

[280] Y. Wang, A. Tagantsev, D. Damjanovic, N. Setter, V. Yarmarkin, A. Sokolov, I. Lukyanchuk, *Journal of Applied Physics* **2007**, *101*, 104115.

[281] J. Wang, P. Wu, X. Ma, L. Chen, *Journal of Applied Physics* **2010**, *108*, 114105.

[282] R. Perez Moyet, Ph.D. Thesis University of Connecticut (Storrs), **2014**.

[283] V. E. Yurkevich, B. N. Rolov, *Physica Status Solidi (b)* **1972**, *52*, 335-343.

[284] V. E. Yurkevich, B. N. Rolov, *Physica Status Solidi (b)* **1972**, *52*, 683-691.

[285] N. Khakpash, G. A. Rossetti Jr., (personal communication), **2018**.

[286] G. A. Rossetti Jr., A. G. Khachaturyan, *Applied Physics Letters* **2007**, *91*, 072909.

[287] G. A. Rossetti Jr., A. G. Khachaturyan, G. Akcay, Y. Ni, *Journal of Applied Physics* **2008**, *103*, 114113.

[288] A. A. Heitmann, G. A. Rossetti Jr., *Journal of the American Ceramic Society* **2014**, *97*, 1661-1685.

[289] M. Porta, T. Lookman, A. Saxena, *Journal of Physics: Condensed Matter* **2010**, *22*, 345902.

[290] F. Weyland, M. Acosta, J. Koruza, P. Breckner, J. Rödel, N. Novak, *Advanced Functional Materials* **2016**, *26*, 7326-7333.

[291] F. Weyland, H. Zhang, N. Novak, *Physica Status Solidi (RRL)–Rapid Research Letters* **2018**, *12*, 1800165.

[292] L. Fulanović, J. Koruza, N. Novak, F. Weyland, B. Malič, V. Bobnar, *Journal of the European Ceramic Society* **2017**, *37*, 5105-5108.

[293] D. A. Lewis, C. Narayan, International Business Machines Corporation, *United States Patent US 5569950A*, Washington, DC, **1996**.

[294] R. J. McGlen, R. Jachuck, S. Lin, *Applied Thermal Engineering* **2004**, *24*, 1143–1156.

[295] F. Weyland, T. Eisele, S. Steiner, T. Frömling, G. A. Rossetti Jr., J. Rödel, N. Novak, *Journal of the European Ceramic Society* **2017**.

[296] M. I. Mendelson, *Journal of the American Ceramic Society* **1969**, *52*, 443-446.

[297] Y. Avrahami, H. Tuller, *Journal of Electroceramics* **2004**, *13*, 463-469.

[298] C. Ang, Z. Yu, L. E. Cross, *Physical Review B* **2000**, *62*, 228-236.

[299] O. Bidault, P. Goux, M. Kchikech, M. Belkaoumi, M. Maglione, *Physical Review B* **1994**, *49*, 7868-7873.

[300] D. C. Sinclair, A. R. West, *Journal of Applied Physics* **1989**, *66*, 3850-3856.

[301] W. L. Warren, K. Vanheusden, D. Dimos, G. E. Pike, B. A. Tuttle, *Journal of the American Ceramic Society* **1996**, *79*, 536-538.

[302] A. Müller, H. Härdtl, *Applied Physics A* **1989**, *49*, 75-82.

[303] J. Maier, *Festkörper—Fehler und Funktion: Prinzipien der Physikalischen Festkörperchemie*, Springer-Verlag, **2013**.

[304] D. M. Smyth, *The Defect Chemistry of Metal Oxides*, Oxford University Press, **2000**.

[305] D. Cooper, C. Baeumer, N. Bernier, A. Marchewka, C. La Torre, R. E. Dunin-Borkowski, S. Menzel, R. Waser, R. Dittmann, *Advanced Materials* **2017**.

[306] J. Glaum, T. Granzow, L. A. Schmitt, H.-J. Kleebe, J. Rödel, *Acta Materialia* **2011**, *59*, 6083-6092.

[307] N. Balke, D. C. Lupascu, T. Granzow, J. Rödel, *Journal of the American Ceramic Society* **2007**, *90*, 1081-1087.

[308] F.-Z. Yao, J. Glaum, K. Wang, W. Jo, J. Rödel, J.-F. Li, *Applied Physics Letters* **2013**, *103*, 192907.

7. Curriculum Vitae

Education

Technische Universität Darmstadt

Ph.D., Materials Science, Since February 2016

- Thesis Title: "Electrocaloric Cooling Power and Long Term Stability of Barium Zirconate Titanate"

M.Sc., Materials Science, January 2016

- Thesis Title: "Electrocaloric Effect in Bismuth Sodium Titanate Based Ceramics"

B.Sc., Materials Science, August 2013

- Thesis Title: "Self-assembled Monolayers on Al_2O_3 as Dielectric for Field Effect Transistors"

Recognitions

- Granted by JECS Trust to participate at the Winter Workshop of the American Ceramic Society (2017)
- Winner at "Student Poster Competition" at the 2016 Joint IEEE ISAF, ECAPD, PFM conference (2016)
- Winner of Hans-Walter-Hennicke award (student competition) of the German Ceramic Society e.V. (2016)

Publications

1. **Weyland, F.**, Acosta, M., Koruza, J., Breckner, P., Rödel, J., & Novak, N. (2016). Criticality: concept to enhance the piezoelectric and electrocaloric properties of ferroelectrics. *Advanced Functional Materials*, *26*(40), 7326-7333.
2. Molin, C., Peräntie, J., Le Goupil, F., **Weyland, F.**, Sanlialp, M., Stingelin, N., ... & Gebhardt, S. (2017). Comparison of direct electrocaloric characterization methods exemplified by 0.92 Pb $(Mg_{1/3}Nb_{2/3})O_3$-0.08 $PbTiO_3$ multilayer ceramics. *Journal of the American Ceramic Society*, *100*(7), 2885-2892.
3. Ayrikyan, A., **Weyland, F.**, Steiner, S., Duerrschnabel, M., Molina-Luna, L., Koruza, J., & Webber, K. G. (2017). Multilayer lead-free piezoceramic composites: Influence of co-firing on microstructure and electromechanical behavior. *Journal of the American Ceramic Society*, *100*(8), 3673-3683.

4. Fulanović, L., Koruza, J., Novak, N., **Weyland, F.**, Malič, B., & Bobnar, V. (2017). Fatigue-less electrocaloric effect in relaxor $Pb(Mg_{1/3}Nb_{2/3})O_3$ multilayer elements. *Journal of the European Ceramic Society*, *37*(15), 5105-5108.

5. **Weyland, F.**, Eisele, T., Steiner, S., Froemling, T., Rossetti Jr., G. A., Roedel, J., & Novak, N. (2018). Long term stability of electrocaloric response in barium zirconate titanate. *Journal of the European Ceramic Society*, *38*(2), 551-556.

6. Patel, S., **Weyland, F.**, Tan, X., & Novak, N. (2018). Tunable pyroelectricity around the ferroelectric/antiferroelectric transition. *Energy Technology*, *6*(5), 865-871.

7. Patel, S., Chauhan, A., Rojas, V., Novak, N., **Weyland, F.**, Rödel, J., & Vaish, R. (2018). Thermomechanical Energy Conversion Potential of Lead-Free 0.50 $Ba(Zr_{0.2}Ti_{0.8})O_3$–0.50 $(Ba_{0.7}Ca_{0.3})TiO_3$ Bulk Ceramics. *Energy Technology*, *6*(5), 872-882.

8. **Weyland, F.**, Acosta, M., Vögler, M., Ehara, Y., Rödel, J., & Novak, N. (2018). Electric field–temperature phase diagram of sodium bismuth titanate-based relaxor ferroelectrics. *Journal of Materials Science*, 53:9393–9400.

9. Pramanick, A., Dmowski, W., Egami, T., Budisuharto, A. S., **Weyland, F.**, Novak, N., ... & Jørgensen, M. R. V. (2018). Stabilization of Polar Nanoregions in Pb-free Ferroelectrics. *Physical review letters*, *120*(20), 207603.

10. **Weyland, F.**, Zhang, H., & Novak, N. (2018). Enhancement of Energy Storage Performance by Criticality in Lead-Free Relaxor Ferroelectrics. *physica status solidi (RRL)–Rapid Research Letters*, *12*(7), 1800165.

11. Novak, N., **Weyland, F.**, Patel, S., Guo, H., Tan, X., Rödel, J., & Koruza, J. (2018). Interplay of conventional with inverse electrocaloric response in $(Pb,Nb)(Zr,Sn,Ti)O_3$ antiferroelectric materials. *Physical Review B*, *97*(9), 094113.

12. **Weyland, F.**, Bradeško, A., Ma, Y. B., Koruza, J., Xu, B. X., Albe, K., ... & Novak, N. (2018). Impact of Polarization Dynamics and Charged Defects on the Electrocaloric Response of Ferroelectric $Pb(Zr,Ti)O_3$ Ceramics. *Energy Technology*, *6*(8), 1519-1525.

13. **Weyland, F.**, Perez-Moyet, R., Rossetti Jr., G. A., & Novak, N. (2018). Material measures of electrocaloric cooling power in perovskite ferroelectrics. *Energy Technology*, *6*(8), 1512-1518.

14. **Weyland, F.**, Hayati, R., Novak, N. (2019). Tuning of electrocaloric performance in $(Ba_{0.85}Ca_{0.15})(Zr_{0.1}Ti_{0.9})O_3$ by induced relaxor-like behavior. *Ceramics International*, 45(9), 11408-11412.

15. Yu, Y., Gao, F., **Weyland, F.**, Du, H., Jin, L., Hou, L., Yang, Z., Novak, N., Qu, S. (2019). Significantly enhanced room temperature electrocaloric response with superior thermal stability in sodium niobate-based bulk ceramics. *Journal of Materials Chemistry A* (accepted manuscript online available)

16. Du, H., Chang, Y., Li, C., Hu, Q., Pang, J., Sun, Y., **Weyland, F.**, Novak, N., Jin, L. (2019). Ultrahigh room temperature electrocaloric response in lead-free bulk ceramics via tape casting. *Journal of Materials Chemistry C* (accepted manuscript online available)

Conference Contributions (presenter)

- European Conference on Application of Polar Dielectrics (ECAPD), Darmstadt, 2016, oral presentation: "Criticality: Boost of piezoelectric and electrocaloric properties"
- Materials Science and Engineering (MSE), Darmstadt, 2016, oral presentation: "Effect of criticality on the piezoelectric and electrocaloric properties of relaxor ferroelectrics"
- Electronic Materials and Applications (EMA), Orlando, 2017, poster presentation: "Electric field induced phase transition in lead-free relaxor ferroelectrics"
- Danish Days on Calorics, Roskilde, 2017, oral presentation: "Long Term Stability of the Electrocaloric Effect"
- Thermag VIII, Darmstadt, 2018, poster presentation: "Material measures of electrocaloric cooling power in perovskite ferroelectrics"
- Materials Research Society (MRS) fall meeting, Boston, 2018, oral presentation: "Comparison of electrocaloric materials on basis of material related cooling power"

8. Eigenständigkeitserklärung

Hiermit versichere ich, die vorliegende Dissertation ohne Hilfe Dritter nur mit den angegebenen Quellen und Hilfsmitteln angefertigt zu haben. Alle Stellen, die aus Quellen entnommen wurden, sind als solche kenntlich gemacht. Diese Arbeit hat in gleicher oder ähnlicher Form noch keiner Prüfungsbehörde vorgelegen.

Darmstadt, den

_____

(Florian Weyland)